UNIVERSITÀ DEGLI STUDI DI PADOVA

DIPARTIMENTO DI FISICA ED ASTRONOMIA "GALILEO GALILEI"

Master Degree in Physics

Final Dissertation

Nonlinear optical characterization of hyperbolic metamaterials

THESIS SUPERVISOR:
Prof. Tiziana Cesca

CANDIDATE:
Francesca Dodici

ACADEMIC YEAR 2020 - 2021

Contents

Abstract

Metamaterials are artificial nanostructured materials displaying peculiar optical properties not usually found in ordinary matter (e.g. negative refractive index, cloaking, enhanced nonlinear optical properties, ...). These properties are not deriving only from the constituent materials but are also strongly dependent on the geometry of their sub-wavelength features. Thus, by properly engineering the structure of the material, it is possible to manipulate also its response. Such are the reasons behind the great interest sparked by this research topic in the last decades. Of particular interest are the so called "hyperbolic metamaterials" (HMs), namely highly anisotropic media designed to have one diagonal element of the dielectric tensor with opposite sign with respect to the other two leading to a special hyperbolic dispersion law. The strong anisotropy of these materials causes their optical response to be strongly dependent on the polarization state and angle of incidence of the interacting electromagnetic field with possible applications in all-optical switching devices. One of their more interesting feature is the enhancement of the nonlinear optical response of these materials in a spectral region of vanishing permittivity called epsilon near-zero (ENZ) region.

The aim of this thesis is the synthesis and characterization of the linear and nonlinear optical response in the visible of multilayer hyperbolic metamaterials (MHMs). The samples, synthesised by magnetron sputtering depositions, are made up of alternating silver/alumina or silver/silica layers and their geometry was designed to obtain their ENZ wavelength in the visible. The morphological characterization of these samples is carried out by atomic force microscopy (AFM) and scanning electron microscopy (SEM) and the linear optical properties are characterized by spectroscopic ellipsometry. Finally, Kerr-type optical nonlinearities, manifesting themselves in nonlinear absorption and nonlinear refraction, are studied and quantified with the z-scan technique. These measurements highlight a peculiar nonlinear response in the MHMs, not traceble in that of the constituent materials. More specifically, nonlinear absorption and refraction are observed at intensities much lower than those required for the onset of optical nonlinearities in single films of Ag, Al_2O_3 or SiO_2. Furthermore, an enhancement of the nonlinear optical parameters is observed in the ENZ range of the silver-alumina MHM. The experimental results of this nonlinear characterization are then compared with simulations generated from a dedicated model, and an excellent agreement is observed between simulations and experimental data. This proves the reliability of the simulation model in predicting the nonlinear response of these metamaterials, paving the way to the possibility of designing metamaterials with tailored nonlinear optical properties.

Introduction

Over the last twenty years, there has been a strong burst of scientific research towards the design and fabrication of metamaterials, namely artificial composite media consisting of structural units much smaller than the wavelength of the electromagnetic radiation they interact with. Due to their sub-wavelength features, metatamerials interact with the incident light as an effective medium with peculiar optical properties, not traceable solely in the chemistry of their original constituent materials, as they are strongly influenced also by their nanoscale geometrical structure. This represents their most attractive feature, as it implies the possibility of tailoring and manipulating the material's response by properly engineering its structure, obtaining also exotic properties not usually found in nature such as negative refractive index [1], invisibility cloaking [2], lensing beyond diffraction limit [3], enhanced nonlinear optical properties [4] and many others.

Of particular interest are the so called "hyperbolic metamaterials" (HMs) [5, 6, 7], highly anisotropic media designed to have one of the diagonal elements of the dielectric tensor with opposite sign with respect to the other two principal components in a spectral region of interest ($\varepsilon_{xx} = \varepsilon_{yy} = \varepsilon_{\parallel}$, $\varepsilon_{zz} = \varepsilon_{\perp} \implies \varepsilon_{\parallel} \cdot \varepsilon_{\perp} < 0$) leading to a hyperbolic dispersion law for an extraordinary TM polarized wave. The name "hyperbolic" derives from the topological change of the isofrequency surface from an ellipsoid to an hyperboloid in the spectral range where the $\varepsilon_{\parallel} \cdot \varepsilon_{\perp} < 0$ condition is met. The production of HMs is relatively simple as the only essential criterion is the restriction of the motion of free electrons in one or two spatial directions to achieve metallic behavior in one direction and insulating behaviour in the other. These materials can be classified into two categories: type I for $\varepsilon_{\parallel} > 0$, $\varepsilon_{\perp} < 0$ and type II for $\varepsilon_{\parallel} < 0$, $\varepsilon_{\perp} > 0$. The peculiar shape of their isofrequency surface allows for propagating waves with infinitely large wavevectors in the ideal limit [5], with applications in the control of spontaneous emission lifetime of emitters [8].

Furthermore, these structures present a spectral range of vanishing dielectric permittivity called epsilon-near-zero (ENZ) region where the real part of the in-plane permittivity $\varepsilon_{\parallel}$ is zero. Most notably, enhanced nonlinear optical responses were observed near the ENZ condition [9, 10, 4]. Since in HMs the spectral position of this ENZ condition can also be tuned by properly designing the geometry of the system (in particular, the metal-dielectric filling fraction), it is possible to obtain strong and fast optical nonlinearities in a selected spectral range, making these metamaterials a flexible platform for the development of lower intensity nonlinear applications.

Among nonlinear optical phenomena, of particular interest is the study of the optical Kerr

effect, a third-order effect which manifests itself as a dependence of absorption and refraction properties of the material on the intensity of the incident radiation [11]. Nonlinear refraction is a promising mechanism to be used in all-optical switching devices whereas nonlinear absorption can be exploited for example in saturable absorbers or optical limiters.

The aim of this thesis is the synthesis and characterization of the linear and nonlinear optical properties in the visible of two types of multilayer hyperbolic metamaterials obtained by magnetron sputtering depositions: a silver/alumina (Ag/Al_2O_3) multilayer and a silver/silica one (Ag/SiO_2). The morphological characterization of these samples is carried out with atomic force microscopy (AFM) and scanning electron microscopy (SEM). Then, the linear optical properties are characterized with spectroscopic ellipsometry. Finally, the nonlinear optical response is studied and quantified with the z-scan technique. The experimental results of this nonlinear characterization will then be compared with simulations generated from the model described in the last chapter.

In Chapter 1 the main concepts required for understanding the theory behind hyperbolic metamaterials and their properties is summarized. Then, in Chapter 2, the techniques and experimental setups employed for the synthesis and characterization of the samples is reported. Finally, the results of the morphological characterization of the samples and the study of the linear optical properties are described in Chapter 3 and the results of the nonlinear optical characterization in Chapter 4. Furthermore, in Appendix A, a brief explanation of the mechanisms behind the growth of silver on metal oxides is reported.

Chapter 1

Theoretical background

In this chapter, the theoretical definitions and concepts required to understand the peculiar properties of hyperbolic metamaterials and the third-order nonlinear optical phenomena considered in this work will be introduced. Firstly, a general discussion on hyperbolic metamaterial, their unique hyperbolic dispersion law and possible application is reported. Then the concept of epsilon-near zero (ENZ) is introduced, followed by the theoretical description of the optical Kerr effect.

1.1 Hyperbolic metamaterials

Hyperbolic metamaterials (HMs) are highly anisotropic anisotropic uniaxial media designed to have one of the principal components of either their permittivity (ε) or permeability (μ) tensors with opposite sign with respect to the other two [5]:

$$\bar{\bar{\varepsilon}} = \begin{pmatrix} \varepsilon_{xx} & 0 & 0 \\ 0 & \varepsilon_{yy} & 0 \\ 0 & 0 & \varepsilon_{zz} \end{pmatrix} = \begin{pmatrix} \varepsilon_{\parallel} & 0 & 0 \\ 0 & \varepsilon_{\parallel} & 0 \\ 0 & 0 & \varepsilon_{\perp} \end{pmatrix} \qquad \text{with} \qquad \varepsilon_{\parallel}\varepsilon_{\perp} < 0 \tag{1.1}$$

where the subscripts $\parallel$, $\perp$ refer to the metamaterial-air interface (xy plane) and the components $\varepsilon_{\parallel}$, $\varepsilon_{\perp}$ are thus called in-plane and out-of-plane permittivities respectively. Similar expressions can be written for the permeability tensor $\bar{\bar{\mu}}$ but since this thesis will only focus on nonmagnetic hyperbolic structures it will be $\mu_{\parallel} = \mu_{\perp} = 1$. In ordinary dielectric media, the three diagonal components are all positive and the medium is defined *biaxial* when $\varepsilon_{xx} \neq \varepsilon_{yy} \neq \varepsilon_{zz}$, uniaxial when $\varepsilon_{xx} = \varepsilon_{yy} \neq \varepsilon_{zz}$, and isotropic when $\varepsilon_{xx} = \varepsilon_{yy} = \varepsilon_{zz}$ [7].

To understand the reason behind the denomination "hyperbolic" let's consider the dispersion relation of light in the medium. The starting point are the following Maxwell's equations in the absence of sources:

$$\nabla \times \mathbf{E} = -\frac{\partial \mathbf{B}}{\partial t} \tag{1.2}$$

$$\nabla \times \mathbf{H} = \frac{\partial \mathbf{D}}{\partial t} \tag{1.3}$$

where $\mathbf{D}$ and $\mathbf{B}$ are the electric displacement and the magnetic induction, which are connected to the electric and magnetic fields $\mathbf{E}$ and $\mathbf{H}$ by the constitutive equations:

$$\mathbf{D} = \varepsilon_0 \bar{\bar{\boldsymbol{\varepsilon}}} \mathbf{E} \tag{1.4}$$

$$\mathbf{B} = \mu_0 \bar{\boldsymbol{\mu}} \mathbf{H} \tag{1.5}$$

where ε_0 and μ_0 are the vacuum permittivity and permeability. By inserting into Eq. 1.2 and 1.3 the plane wave expressions $\mathbf{E} = \mathbf{E}_0 e^{i(\omega t - \mathbf{k}\cdot\mathbf{r})}$ and $\mathbf{H} = \mathbf{H}_0 e^{i(\omega t - \mathbf{k}\cdot\mathbf{r})}$, where $\mathbf{k}$ is the wave vector, one obtains:

$$\mathbf{k} \times \mathbf{E} = \omega \mu_0 \mathbf{H} \tag{1.6}$$

$$\mathbf{k} \times \mathbf{H} = -\omega \varepsilon_0 \bar{\bar{\varepsilon}} \mathbf{E} \tag{1.7}$$

and by substituting Eq. 1.6 into Eq. 1.7 the result is the following eigenvalue problem for the electric field E:

$$\mathbf{k} \times (\mathbf{k} \times \mathbf{E}) + \omega^2 \mu_0 \varepsilon_0 \bar{\bar{\varepsilon}} \mathbf{E} = 0 \tag{1.8}$$

or, in matrix form:

$$\begin{bmatrix} k_0^2 \varepsilon_{xx} - k_y^2 - k_z^2 & k_x k_y & k_x k_z \\ k_x k_y & k_0^2 \varepsilon_{yy} - k_x^2 - k_z^2 & k_y k_z \\ k_x k_z & k_y k_z & k_0^2 \varepsilon_{zz} - k_x^2 - k_y^2 \end{bmatrix} \begin{bmatrix} E_x \\ E_y \\ E_z \end{bmatrix} = 0 \tag{1.9}$$

where $k_0 = \omega/c$ is the magnitude of the wave vector and $c = 1/\sqrt{\varepsilon_0 \mu_o}$ the speed of light in vacuum. Considering the specific case of a uniaxial medium with optical axis along the $\hat{\mathbf{z}}$ direction, the components of the permittivity tensor can be denoted as in Eq. 1.1: $\varepsilon_{xx} = \varepsilon_{yy} = \varepsilon_{\parallel} \neq \varepsilon_{zz} = \varepsilon_{\perp}$. The imposition of non trivial solutions to Eq. 1.9 finally leads to the equation [7]:

$$\left(k_x^2 + k_y^2 + k_z^2 - \varepsilon_{\parallel} k_0^2\right) \left(\frac{k_x^2 + k_y^2}{\varepsilon_{\perp}} + \frac{k_z^2}{\varepsilon_{\parallel}} - k_0^2 \right) = 0 \tag{1.10}$$

whose solutions are the dispersion relation for ordinary TE polarized waves (polarization in the xy plane):

$$k_x^2 + k_y^2 + k_z^2 = \varepsilon_{\parallel} \left(\frac{\omega}{c} \right)^2 \tag{1.11}$$

and the dispersion relation for extraordinary TM polarized waves (polarization along the optical axis $\hat{\mathbf{z}}$):

$$\frac{k_x^2 + k_y^2}{\varepsilon_{\perp}} + \frac{k_z^2}{\varepsilon_{\parallel}} = \left(\frac{\omega}{c} \right)^2 \tag{1.12}$$

The first one (Eq. 1.11) denotes a spherical isofrequency surface in the k-space whereas the second, for common uniaxial materials with $\varepsilon_{\parallel}\varepsilon_{\perp} > 0$ denotes an ellipsoidal isofrequency surface. However, when the condition $\varepsilon_{\parallel}\varepsilon_{\perp} < 0$ is verified, a topological change of this isofrequency surface from ellipsoid to hyperboloid occurs, thus the name "hyperbolic metamaterials" (HMs). The condition for hyperbolic dispersion is verified in two cases: Type I HMs have $\varepsilon_{\parallel} > 0$, $\varepsilon_{\perp} < 0$ whereas Type II HMs have $\varepsilon_{\parallel} < 0$, $\varepsilon_{\perp} > 0$. In the first case the isofrequency surface is a two-fold

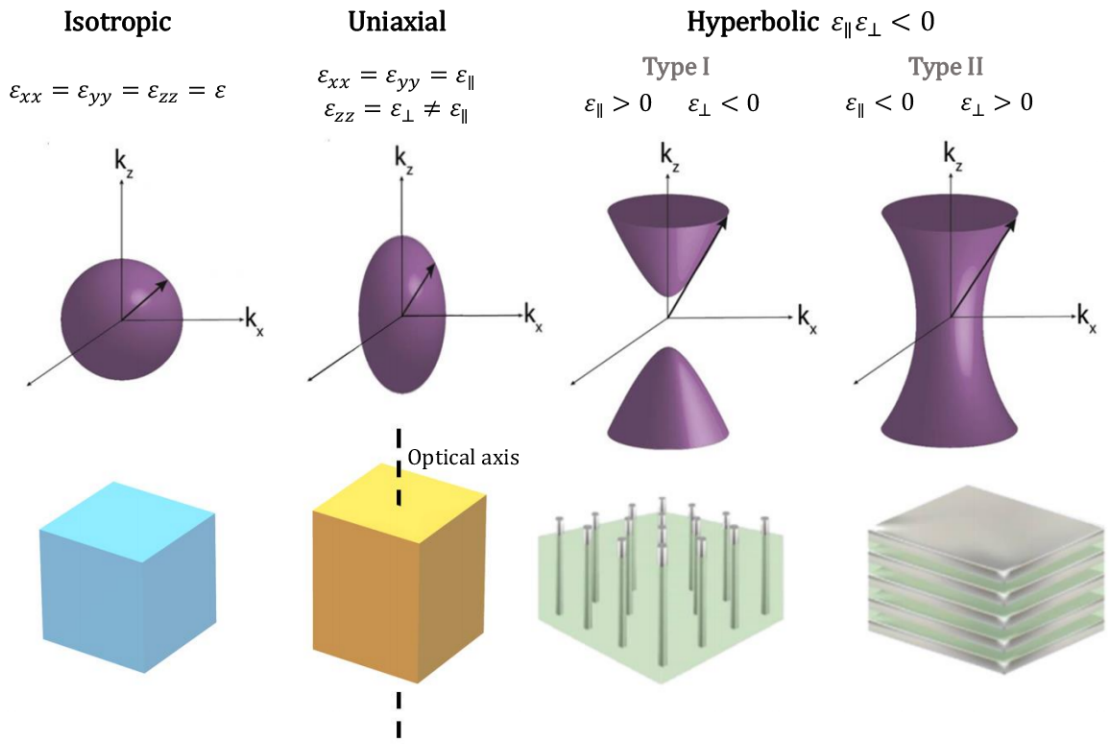

Figure 1.1: Schematic representation of the isofrequency surfaces in the k-space for isotropic, uniaxial and hyperbolic media. Image adapted from [6].

hyperboloid, whereas in the other it is a continuous, one-fold hyperboloid. All these concepts are schematized in Fig. 1.1.

The production of HMs is relatively simple as the only essential criterion is the restriction of the motion of free electrons in one or two spatial directions to achieve metallic behavior in one direction ($\varepsilon < 0$) and insulating behaviour in the other ($\varepsilon > 0$) [5]. As a matter of fact, since in metals the real part of the dielectric function is negative below the plasma frequency because the polarization response of free moving electrons is opposite with respect to the electric field, to have negative components of the dielectric tensor in only one or two spatial directions it is sufficient to restrict the free-electron motion to these directions. Hence, the most common realizations are multilayered metal-dielectric structures for Type II behaviour [12, 13, 14, 15] or arrays of parallel metallic nano-wires embedded in a dielectric matrix for Type I [16, 9, 17]. As in all metamaterials, the size, shape and constituent materials of the structural units are carefully chosen to achieve the desired properties [6]. This thesis will focus on Ag based multilayer hyperbolic metamaterials.

Hyperbolic metamaterials present peculiar optical properties which make them attractive for many possible applications in nanophotonics, biosensing, plasmonics and nonlinear optics [7, 5, 14]. For example, by tuning the shape of the hyperbolic dispersion, the propagation of light in HMs may be flexibly controlled, producing all-angle negative refraction, collimation, splitting, near-perfect absorption and abnormal scattering [18]. Besides, the peculiar shape of the isofrequency surface in materials with hyperbolic dispersion allows for propagating waves with

infinitely large wavevectors in the ideal limit, whereas high k-modes are typically evanescent in ordinary materials. This leads to many possible applications such as enhancement of spontaneous emission in compliance with Fermi's golden rule (Purcell effect) [13, 19, 20].

Furthermore, an enhancement of the nonlinear optical response, not limited by that of the constituent materials, has been observed in both type I and type II hyperbolic metamaterials [8, 9, 15, 21]. This makes them suitable to be employed in emerging light-based metadevices where efficient nonlinear optical interactions are essential. As a matter of fact, the onset of optical nonlinearities typically requires intense laser sources and long interaction lengths. Therefore, the enhanced nonlinear response of this class of metamaterials can be exploited in applications requiring lower powers and smaller footprints.

1.1.1 Effective medium approximation

As stated in the Introduction, one of the most interesting features of metamaterials is the possibility of engineering the response of the material to an external electromagnetic field with a proper design of its structure. Besides, given the size of the nano scale features of these materials, which are smaller than the wavelength of the incident radiation, this response can be described within a simple effective medium theory by defining effective macroscopic parameters. In hyperbolic metamaterials (HMs), the two isotropic components are a metal and a dielectric with bulk permittivities ε_m and ε_d respectively. Since these quantities are frequency-dependent, in an effective medium approximation (EMA) the material will respond as an effective metal, a dielectric or type I or II HM depending on the metallic filling fraction f_m and the wavelength of the incident radiation λ.

In the case of a multilayer like those studied in this work, the metal and the dielectric are periodically arranged in a system of parallel thin layers with thicknesses t_m and t_d respectively (with $t_m + t_d \ll \lambda$). In this case, the metal and dielectric filling fractions are simply:

$$f_m = \frac{t_m}{t_d + t_m} \tag{1.13}$$

$$f_d = \frac{t_d}{t_d + t_m} = 1 - f_m \tag{1.14}$$

Since the effective response is also strongly dependent on the polarization state of the incident radiation let's consider a cartesian system of reference as the one represented in Fig. 1.2, with the $\hat{\mathbf{z}}$ axis along the optical axis of the system, i.e. orthogonal to the metal-dielectric interfaces of the multilayer. In this system of reference, for light with s-polarization (or TE) the electric field oscillates in the **xy** plane, i.e. parallel to the interfaces. Instead, for p-polarized (or TM) light, the electric field oscillates along the $\hat{\mathbf{z}}$ axis, i.e. orthogonally to the interfaces. Moreover, the dielectric tensor assumes the form defined in Eq. 1.1, with in-plane component of the permittivity $\varepsilon_{\parallel}$ and out-of-plane component $\varepsilon_{\perp}$.

To determine the effective in-plane permittivity of the material, let's consider the continuity condition of the tangential component of the electric field across an interface [6]. In this case:

$$E_m^{\parallel} = E_d^{\parallel} = E^{\parallel} \tag{1.15}$$

where $E_m^{\parallel}$ is the electric field in the metallic layers, $E_d^{\parallel}$ in the dielectric layers, and $E^{\parallel}$ is the electric field in the overall effective medium. Moreover, in each layer, the constitutive equation Eq. 1.4 between the electric field displacement D and the electric field E is verified. From the continuity of the dielectric displacement in the parallel direction, the average displacement can be found by averaging the displacement field contributions from the metallic and dielectric components D_m and D_d [6]:

$$D^{\parallel} = f_m D_m^{\parallel} + (1 - f_m) D_d^{\parallel} \tag{1.16}$$

and substituting Eq. 1.4 for each layer into Eq. 1.16:

$$\varepsilon_0 \varepsilon_{\parallel} E^{\parallel} = f_m \varepsilon_0 \varepsilon_m E_m^{\parallel} + (1 - f_m) \varepsilon_0 \varepsilon_d E_d^{\parallel} \tag{1.17}$$

By cancelling out the common terms, the final expression for the in-plane effective permittivity is obtained:

$$\varepsilon_{\parallel} = f_m \varepsilon_m + (1 - f_m) \varepsilon_d \tag{1.18}$$

This is the effective permittivity of the material for an orthogonally incident electric field with s-polarization. To find the out-of-plane component $\varepsilon_{\perp}$ the starting point is still Maxwell's equations and the electromagnetic field boundary conditions. More specifically, for the normal component, the electric displacement vector at an interface must be continuous:

$$D^{\perp} = D_m^{\perp} = D_d^{\perp} \tag{1.19}$$

and the total electric field in the multilayer system will be a superposition of the electric field components from the dielectric and metallic layers.

$$E^{\perp} = f_m E_m^{\perp} + (1 - f_m) E_d^{\perp} \tag{1.20}$$

where $E_m^{\perp}$ is the perpendicular component of the electric field in the metallic region and $E_d^{\perp}$ in the dielectric one. Again, substituting Eq. 1.4 and 1.19 into 1.20 and cancelling out the common terms, the analytic expression for the electric permittivity of the multilayer metamaterial in the perpendicular direction is found [6]:

$$\varepsilon_{\perp} = \frac{\varepsilon_m \varepsilon_d}{f_m \varepsilon_d + f_d \varepsilon_m} \tag{1.21}$$

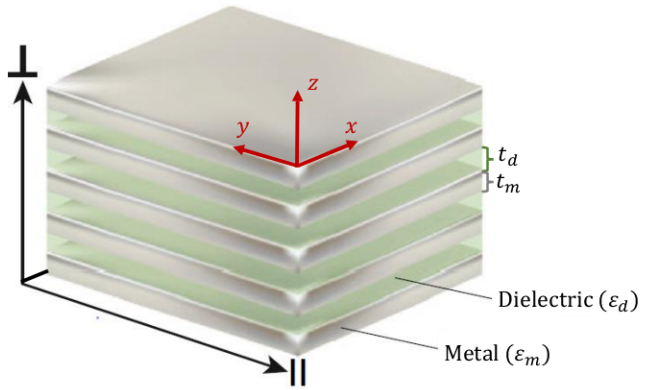

Figure 1.2: Scheme of the metal-dielectric multilayer considered. The metal and dielectric layers have permittivities ε_m, ε_d and thicknesses t_m, t_d respectively. The $\hat{\mathbf{z}}$ direction is denoted as $\perp$ whereas directions in the **xy** plane are denoted with $\parallel$. Image adapted from [6].

This is the effective permittivity for an orthogonally incident electric field with p-polarization. When the input field propagates at an angle θ with respect to the optical axis of the system (i.e. the normal to the interfaces) if the field is linearly polarized with TE polarization (s), the complex effective permittivity of the metamaterial has no angular dependence and it is:

$$\varepsilon_{\mathrm{TE}}(\theta) = \varepsilon_{\parallel} \tag{1.22}$$

On the other hand, for TM polarization (p) it results:

$$\varepsilon_{\mathrm{TM}}(\theta) = \frac{\varepsilon_{\parallel}\varepsilon_{\perp}}{\varepsilon_{\parallel}\sin^2(\theta) + \varepsilon_{\perp}\cos^2(\theta)} \tag{1.23}$$

With analogous reasoning, this homogenization procedure is also possible for systems of metallic nanorods in a dielectric matrix [8, 6].

To sum up, the constitutive parameters defining the effective response of the metamaterial are: the metal filling fraction f_m, the permittivity of the metal ε_m and the permittivity of the dielectric ε_d. By properly setting these parameters, the optical response of the material can be engineered. Besides, the permittivities ε_m, ε_d are usually not constant but are frequency-dependent leading to a dispersive behaviour also in the metamaterial: $\varepsilon_{\parallel} = \varepsilon_{\parallel}(\lambda)$ and $\varepsilon_{\perp} = \varepsilon_{\perp}(\lambda)$. The effective behaviour of the metamaterial is thus also strongly dependent on the wavelength of the incident field. In Fig. 1.3 are reported the phase diagrams showing the evolution of the effective response of mulilayer and nanorod Ag/Al_2O_3 systems as a function of the wavelength and the filling fraction (at normal incidence). It can be seen that, in the visible, type II behaviour is more easily achieved with multilayer systems whereas type I is more typical of nanorods systems. In any case, transitions between different effective behaviours can occur at different wavelengths depending on the choice of the constituent materials. For this reason, depending on the spectral region where hyperbolic dispersion is desired, different combinations of materials should be chosen.

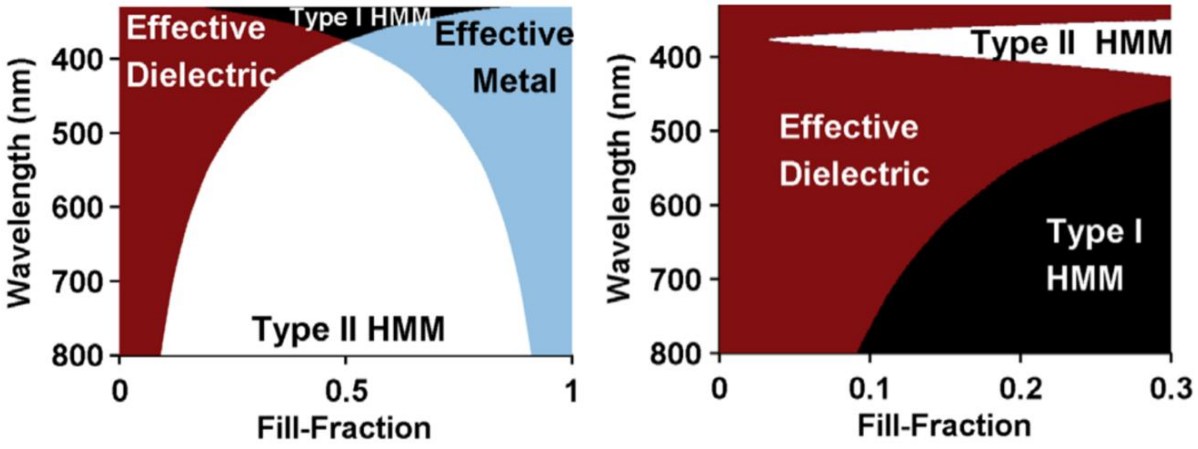

(a) (b)

Figure 1.3: Phase diagrams showing the effective response of hyperbolic metamaterials as a function of the metal filling fraction and the wavelength of the incident radiation for (a) an Ag/Al_2O_3 multilayer syestem and (b) Ag nanowires in an Al_2O_3 matrix [8].

Additionally, as shown by Eq. 1.23, an external control over the response of the material can be achieved also by varying the angle of incidence θ and polarization state of the input field. This external control is one of the most interesting features of this class of materials and could be exploited, for example, to engineer the nonlinear response of HMs to be used in all-optical switching devices.

1.1.2 Epsilon near-zero

Another interesting feature that comes out from the predictions of the effective medium theory is the existence of a condition of vanishing permittivity called *epsilon near-zero* (ENZ) condition in which the real part of the in-plane permittivity is zero $\mathfrak{Re}[\varepsilon_{\parallel}] = 0$. This property is of particular interest as, recently, this class of ENZ materials has been reported to exhibit unprecedented ultrafast nonlinear efficiencies within sub-wavelength propagation lengths [9, 4, 15].

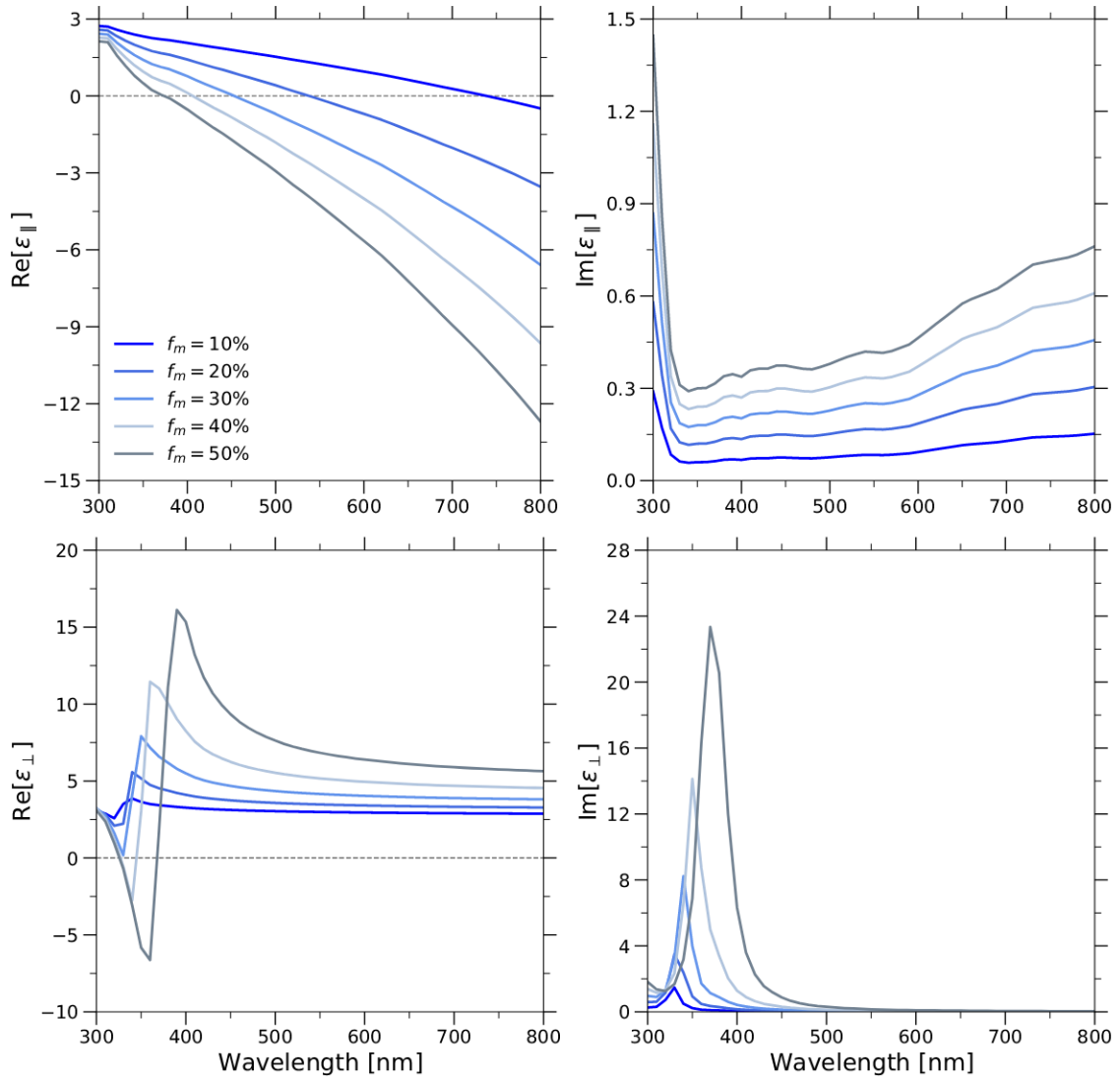

Figure 1.4: Real and imaginary parts of the in-plane ($\varepsilon_{\parallel}$, upper row) and out-of plane ($\varepsilon_{\perp}$, bottom row) permittivities of an Ag/Al_2O_3 multilayer for increasing values of the metal filling fraction f_m.

In addition to hyperbolic metamaterials, there are also some media with naturally occurring vanishing permittivity like some degenerately doped semiconductors such as tin-doped indium oxide (ITO) [10] and aluminium-doped zinc oxide (AZO) [22]. However, these materials are less flexible than ENZ metamaterials as their λ_{ENZ} is fixed and they do not present the same possibilities of metamaterials in the tuning of the response upon changing polarization state and incidence angle of the input radiation.

In Fig. 1.4 it is shown the evolution of the real and imaginary parts of the in-plane ($\varepsilon_{\parallel}$) and out-of plane ($\varepsilon_{\perp}$) permittivities of an Ag/Al_2O_3 multilayer for increasing values of the metal filling fraction f_m. From the upper-left panel in Fig. 1.4, it can be seen that the spectral position of the epsilon near-zero wavelength λ_{ENZ} blueshifts for increasing values of the metal filling fraction f_m. Thus, the position of this zero crossing point can be tuned with a proper choice of the materials and the proportions in which they are present.

1.2 Nonlinear optics

Nonlinear optics refers to optical phenomena that occur as a consequence of the modification of the optical properties of a material system by the presence of light of sufficiently high intensity [11]. The name "nonlinear" comes from the fact in these phenomena the system responds in a nonlinear manner with the strength of the applied optical field. These nonlinear effects are typically weak and require high intensities of light to be observed. Because of this, the nonlinear regime of interaction of light and matter became accessible only with the development of lasers [23]. The response of a material to an external electric field $E(t)$ can be described in terms of the induced polarization $P(t)$. In linear optics, $P(t)$ is assumed to be linearly dependent on the electric field strength $E(t)$ and is described by the relationship:

$$P(t) = \varepsilon_0 \chi^{(1)} E(t) \tag{1.24}$$

where ε_0 is the vacuum permittivity and $\chi^{(1)}$ is the nonlinear optical susceptibility. However, with sufficiently strong electric fields, typically $\gtrsim 10^{11}$V/m [11], higher order terms become comparable with the linear term and phenomena related to these higher order terms arise. In this case Eq. 1.24 becomes:

$$\begin{aligned} P(t) &= \varepsilon_0 \left[\chi^{(1)} E(t) + \chi^{(2)} E^2(t) + \chi^{(3)} E^3(t) + \cdots \right] \\ &= P^{(1)}(t) + P^{(2)}(t) + P^{(3)}(t) + \cdots \end{aligned} \tag{1.25}$$

where the quantities $\chi^{(2)}$, $\chi^{(3)}$, ... are the second- and third-, ... order nonlinear optical susceptibilities. In Eq. 1.25, for the sake of simplicity, the dependency of the $\chi^{(k)}$ on the frequency of the incident radiation ω is omitted and are written as a scalar quantitiy as the fields $P(t)$ and $E(t)$. When considered as vectors however, $\chi^{(k)}$ becomes a tensor of rank $(k+1)$. $P^{(2)}(t) = \varepsilon_0 \chi^{(2)} E^2(t)$, is the second-order nonlinear polarization, $P^{(3)}(t) = \varepsilon_0 \chi^{(3)} E^3(t)$ the third-order nonlinear polarization, and so on for higher-order terms.

The nonlinear processes occurring as a result of the second-order polarization $P^{(2)}$ are distinct from those that occur as a result of the third-order polarization $P^{(3)}$. More in general,

nonlinear optical phenomena of n-th order are proportional to the n-th power of the driving field. Besides, $\chi^{(2)}$ is null in centrosymmetric media, i.e. media with no inversion symmetry such as liquids, gases, amorphous solids. For this reason, such materials cannot produce second-order nonlinear optical interaction like second harmonic generation (SHG), sum-frequency generation and difference-frequency generation [11]. On the other hand, third-order nonlinear optical interactions such as thitd harmonic generation (THG) or optical Kerr effect, can occur for both centrosymmetric and noncentrosymmetric media.

1.2.1 Optical Kerr effect

Among the many nonlinear optical phenomena, this thesis is focused on the optical Kerr effect which is a third order nonlinear optical process which causes the effective susceptibility of the material to depend on the intensity of the incident electromagnetic field. To see this, let's consider the third-order contribution to the nonlinear polarization:

$$P^{(3)}(t) = \varepsilon_0 \chi^{(3)} E^3(t) \tag{1.26}$$

In the most the general case, the field $E(t)$ is made up of several different frequency components and Eq. 1.26 is actually much more complicated [23]. Thus, it is much simpler to consider the case of monochromatic incident field of frequency ω:

$$E(t) = \mathcal{E} \cos(\omega t) \tag{1.27}$$

and by inserting Eq. 1.27 into Eq. 1.26 and using the trigonometric identity $\cos^3 \omega t = \frac{1}{4}\cos 3\omega t + \frac{3}{4}\cos \omega t$ the third-order nonlinear polarization becomes:

$$\begin{aligned} P^{(3)}(t) &= \frac{1}{4}\epsilon_0 \chi^{(3)} \mathcal{E}^3 \cos 3\omega t + \frac{3}{4}\epsilon_0 \chi^{(3)} \mathcal{E}^3 \cos \omega t \\ &= P^{(3)}(3\omega t) + P^{(3)}(\omega t) \end{aligned} \tag{1.28}$$

The first term in Eq. 1.28, $P^{(3)}(3\omega t)$, describes a response at frequency 3ω that is created by an applied field at frequency ω. This phenomenon is called third-harmonic generation [11] and its study goes beyond the purpose of this thesis. On the other hand, the second term describes the optical Kerr effect which is a nonlinear contribution to the polarization at the same frequency as that of the incident field ω:

$$\begin{aligned} P^{(3)}(\omega t) &= \frac{3}{4}\varepsilon_0 \chi^{(3)} \mathcal{E}^2 \cdot \mathcal{E} \cos \omega t \\ &= \frac{3}{4}\varepsilon_0 \chi^{(3)} |E(\omega t)|^2 E(\omega t) \end{aligned} \tag{1.29}$$

In light of these calculations, in a centrosymmetric system (i.e. second-order effects are canceled out), the polarization, keeping the leading third-order nonlinear term, is:

$$P(\omega) = \varepsilon_0 \left(\chi^{(1)} + \frac{3}{4}\chi^{(3)} |E(\omega)|^2 \right) E(\omega) = \varepsilon_0 \chi_{\text{eff}}(I) E(\omega) \tag{1.30}$$

Since the intensity of the incident beam is proportional to the square modulus of the electric field ($I = \frac{1}{2}\varepsilon_0 n_0 c|E|^2$, where n_0 is the linear refractive index of the medium), as shown by Eq. 1.30 the optical Kerr effect causes the effective susceptibility of the material to be dependent on the intensity of incident radiation:

$$\begin{aligned}\chi_{\text{eff}}(I) &= \chi^{(1)} + \frac{3}{4}\chi^{(3)}\,|E_c(\omega)|^2 \\ &= \chi^{(1)} + \frac{3}{2}\frac{1}{c\varepsilon_0 n_0}\chi^{(3)}(I)\end{aligned} \tag{1.31}$$

1.2.2 Nonlinear absorption and nonlinear refraction

Given the relation between the complex refractive index $\tilde{n} = n + i\kappa$ (where n is the real refractive index and κ the extinction coefficient) and the suscettivity χ_{eff} of a material, namely:

$$\tilde{n} = \sqrt{\varepsilon/\varepsilon_0} = \sqrt{1 + \chi_{\text{eff}}} \tag{1.32}$$

the optical Kerr effect causes also an intensity dependence of the refractive index and absorption coefficient of the material according to Eq. 1.33

$$\begin{cases} n(I) = n_0 + n_2 I \\ \alpha(I) = \alpha + \beta I \end{cases} \tag{1.33}$$

where $n_0 = \sqrt{1 + \chi^{(1)}}$ is the linear refractive index of the material, n_2 the nonlinear refractive index, β the nonlinear absorption coefficient and $\alpha_0 = 4\pi\kappa/\lambda$ is the linear absorption coefficient. The nonlinear parameters n_2 and β can also be extracted from the real and imaginary parts of the complex third-order susceptibility $\chi^{(3)} = \chi^{(3)}_{Re} + i\chi^{(3)}_{Im}$. As a matter of fact, by developing in power series Eq. 1.29 and neglecting terms of order I^2 one obtains:

$$\begin{cases} \chi^{(3)}_{Re} = \dfrac{2\varepsilon_0 c n_0}{3}\left(2n_0 n_2 - \dfrac{\alpha_0\beta}{2k^2}\right) \\ \chi^{(3)}_{Im} = \dfrac{2\varepsilon_0 c n_0}{3}\left(\dfrac{n_0\beta}{k} - \dfrac{\alpha_0 n_2}{k}\right) \end{cases} \tag{1.34}$$

with $k = \frac{2\pi}{\lambda}$ the wavevector's modulus. When the material's absorption is negligible, namely $\kappa = \alpha_0/2k \ll n_0$ the previous expressions can be simplified and real and imaginary parts of the susceptibility become proportional to n_2 and β respectively [11]:

$$\begin{cases} n_2 = \dfrac{3\chi^{(3)}_{Re}}{4\varepsilon_0 c n_0 \mathfrak{Re}(n_0)} \\ \beta = \dfrac{3k\chi^{(3)}_{Im}}{2\varepsilon_0 c n_0 \mathfrak{Re}(n_0)} \end{cases} \tag{1.35}$$

Regarding nonlinear refraction, the dependence of the material's refractive index on the intensity of the incident radiation causes an intensity-dependent phase-shift in a wave interacting with the material for a distance L according to:

$$\Delta\phi = \frac{2n_2 I L}{\lambda} \tag{1.36}$$

This intensity-dependent phase shift generated by nonlinear refraction causes a self-focusing or self-defocusing effect on the incident beam depending on the sign of n_2. As a matter of fact, as shown in Fig. 1.5, if $n_2 > 0$ and considering an incident beam with Gaussian radial intensity profile, as the local irradiance increases so does the refractive index of the medium: the material effectively acts as a positive lens, causing the rays to curve toward each other thus focalising the incident beam. On the contrary, if $n_2 < 0$, the refractive index decreases with stronger intensities, leading to divergence of the incident beam in the material.

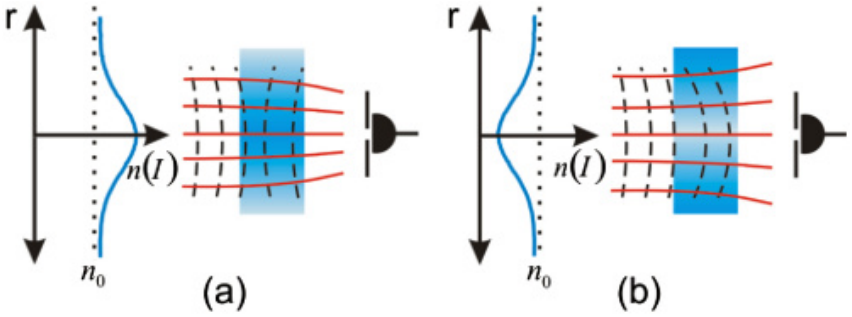

Figure 1.5: Scheme of the self-focusing mechanism when $n_2 > 0$ (a) and of self-defocusing when $n_2 < 0$ (b). Image from [24]

The nonlinear absorption parameter β can also be either negative or positive. If $\beta < 0$ the material's absorption decreases with sufficiently high incident intensities, leading in contrast, to an increase in transmittance. This phenomenon is called saturable absorption (SA) and can be physically understood by considering the system as a simple two-level system with a ground state and an excited state: SA generally occurs when the absorption cross section of the excited state is smaller than that of the ground state [11]. On the other hand, if $\beta > 0$, the material's absorbption increases with the incident intensity. This other situation is called reverse saturable absorption (RSA) Reverse saturable absorption generally arises when the excited state absorption cross section of the system is larger than the ground state one [25].

In addition to SA and RSA, with strong incident intensities higher order effects can arise leading to a dependence on I also of the β parameter. Besides, both SA and RSA contributions can be activated in the system. In this situations, the nonlinear absorption coefficient assumes a more complicated expression [26]:

$$\beta(I) = \beta_{\mathrm{RSA}}(I) + \beta_{\mathrm{SA}}(I) = \frac{\beta_+}{1 + \frac{I_0}{I_s^+}} + \frac{\beta_-}{1 + \frac{I_0}{I_s^-}} \tag{1.37}$$

where β_+ and β_- are the unsaturated absorption coefficients for RSA and SA respectively and the quantities $I_s^{\pm}$ are the saturation intensities of the two processes.

Chapter 2

Experimental methods

In this chapter, a description of the experimental setups and techniques used for the synthesis and characterization of the morphological and optical properties of the studied samples is provided.

Firstly, the magnetron sputtering technique through which the samples were synthesized, is described. Then the techniques used for the study of the structure and composition of the samples are described, namely Atomic Force Microscopy (AFM), Scanning Electron Microscopy (SEM) and Spectroscopic Ellipsometry. The latter, is also used for determining the linear optical properties of the samples. Finally, the z-scan technique used for the study of the nonlinear optical response is discussed.

2.1 Synthesis techniques

2.1.1 Magnetron sputtering

Physical sputtering is a process whereby atoms or molecules of a target material are ejected due to momentum transfer from bombarding highly energetic, atomic-sized particles. These energetic particles are usually ions of a gaseous material accelerated by an electric field. The ejected material can then be transfered directly onto substrates [27]. To efficiently exploit sputtering as a coating process, a number of criteria must be met. To begin with, in order to eject atoms from the target material, one must generate ions of sufficient energy. Besides, ejected atoms must be able to move freely towards the sample to be coated, with little impedance to their movement. For these reasons, sputter coating is a vacuum process: low pressures are required both to maintain high ion energies and to prevent too many atom-gas collisions after ejection from the target. Sputtering is also a plasma-based process: the target is usually kept at a negative potential so that when the gas is introduced into the system, some of its atoms are ionized by this electric field, creating a discharge and igniting a plasma of the bombarding ions. Typically, Ar is used as inert gas as it is a relatively inexpensive inert gas [28].

One crucial aspect to make the deposition process as efficient as possible is to maximize the sputtering yield which is the ratio of atoms sputtered to the number of high energy incident particles. This ratio depends on the mass of the bombarding particle as well as on the chemical

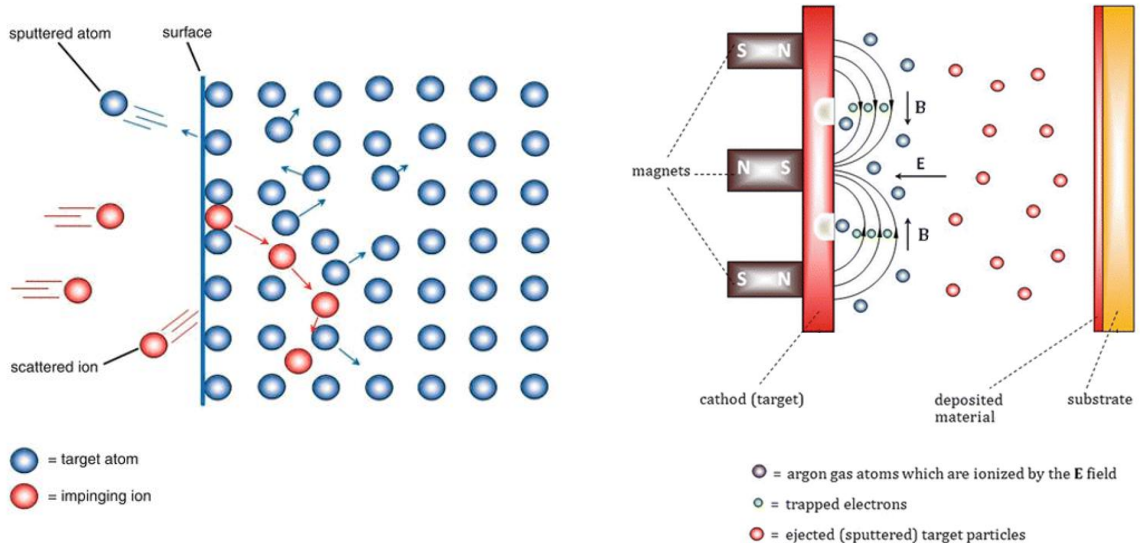

(a) (b)

Figure 2.1: (a) Scheme of the sputtering mechanism: the energetic impinging ions may penetrate into the surface region of the target inducing a collision sequence in which some of the momentum is transferred to surface atoms, leading to their ejection, i.e., sputtering. (b) Simplified scheme of a magnetron sputtering. An arrangement of magnets is placed behind the target which is held at a negative potential. The magnetic field confines the plasma in close proximity of the target [29].

bonding of the target atoms and the energy transferred by collision. The sputtering yield is also sensitive to the angle of incidence of the bombarding particle: for off-normal bombardment, the ratio initially increases to a maximum and then decreases rapidly when the angle is such that most of the bombarding particles are reflected from the surface. Moreover, there is a threshold energy below which sputtering does not occur no matter how high the bombarding flux. However, also when the kinetic energy of ions is too high, they lose much of their energy far below the surface, and the ejection of a target ion becomes more difficult. Consequently, the sputtering yield progressively decreases [28]. When the sputtering process is only induced by bombarding the target with energetic ions, the deposition rates are usually far too low to be used for practical purposes as the times required for deposition would be exceedingly long. This lead to the development of *magnetron sputtering* in which one or more magnets are located close to the target holder to generate a strong magnetic field deflecting the electrons and keeping them near the target in a closed path as shown in Fig. 2.1 (b). This confines the plasma close to the target and increases its denisty, speeding up the sputtering process and, consequenly, improving deposition rates.

The configuration of the electrical field inside the chamber depends on the target material. For the deposition of a conductive one, a simple direct current (DC) configuration, with the sample holder grounded and the target kept at a fixed negative potential, can be used. When working with insulating or semiconductor materials however, this configuration is not efficient: since no current can flow through the target, the ionized bombarding atoms induce an accumulation of charge on its surface. The solution to this problem is to work in radiofrequency (RF) using an

alternating current at high frequency to hit the target with alternatively positive and negative ions, avoiding charge accumulation.

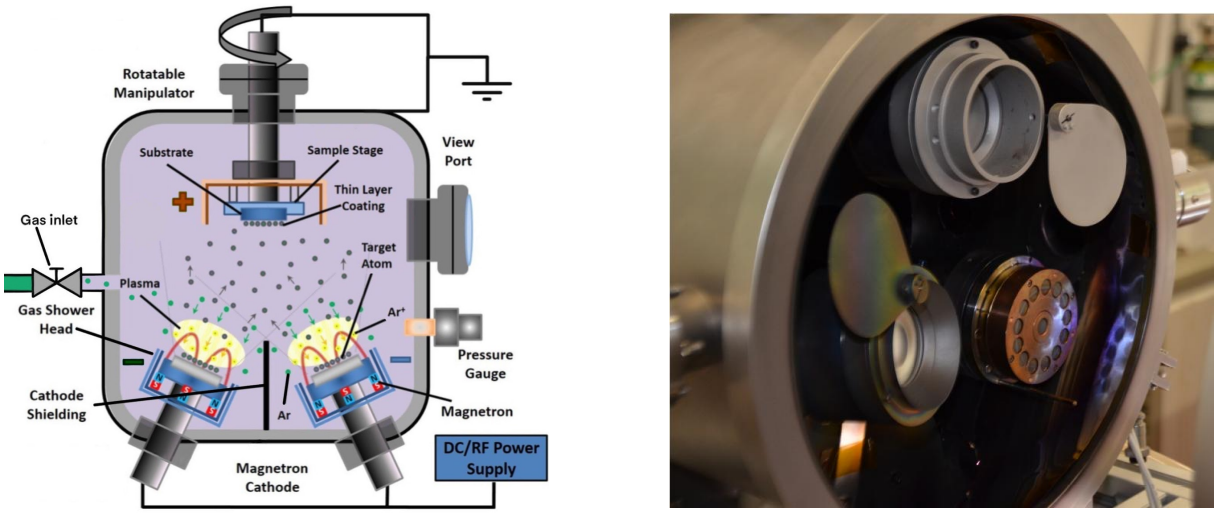

(a) (b)

Figure 2.2: (a) Scheme of the magnetron sputtering setup used in this work. Only two torches are shown for clarity (image adapted from [30]). (b) Photo of the inside of the vacuum chamber of the magnetron sputtering machine on the side where the three torches are placed.

The magnetron sputtering setup used to synthesize the samples studied in this work is schematized in Fig. 2.2(a). It is made up of a cylindrical vacuum chamber where the pre-vaccum condition is achieved with a rotatory pump, whereas a turbomolecular pump allows to reach the high vacuum ($\sim 10^{-6}$ mbar) required to remove from the chamber gasses like oxigen or water vapour which might impact negatively on the quality of the deposition. A feedback system connected to a pressure gauge allows to keep a constant pressure of $10^{-2} \div 10^{-3}$ mbar once Ar is fluxed inside the chamber. On one side of the chamber is located the sample holder which can be kept in continuous rotation throughout the deposition to further ensure the uniformity of the deposited film. More than one substrate can be placed on the sample holder, allowing the synthesis of more than one sample under the same conditions. On the other side of the chamber are located three target holders (also called torches) each one equipped with a shutter. The sample holder, acting as anode, is grounded whereas the torches, acting as cathodes, are connected to their own independent DC or RF power supply. This makes it possible to deposit up to three different materials in the same sputtering session. Moreover, by alternately opening and closing the shutters and consequently alternating the sputtered target, one can create a multilayer of up to three different materials. Another fundamental function of the shutters is that they allow to perform a pre-sputtering of the target, which is useful to remove possible surface layers of oxide or contaminants from the target before the actual deposition takes place. This can be done by simply keeping the shutter closed while the plasma is ignited close to the target. All torches can be tilted towards the sample holder with different inclinations and the sample holder as well can be moved closer or farther from the torches. The setup is also equipped with a water cooling system to contain the overheating of the chamber and its components. In fact, although the

sputtering yield is rather insensitive to the temperature of the sputtering target [28], thermal stress can still be harmful for the target as it might lead to damages and possible contamination from atoms sputtered by the target holder.

2.2 Characterization of the samples

2.2.1 Atomic Force Microscopy

Firstly invented by *G. Binnig* in 1986 [31] Atomic Force Microscopy is a very sensitive technique that allows to see and measure almost any kind of material solid surface with great resolution and accuracy at the atomic scale. It works in a quite different way compared to other microscopy techniques such as optical or electron microscopy as it does not form an image by focusing light or electrons onto a surface, but it physically "feels" the surface of the samples with a sharp probe, building up a map of the height of the surface of the sample [32]. To perform this mapping, the force of interaction of a probe, placed at nanoscale distance from the sample, is used. Then, the data collected from an AFM must be analyzed to form a proper image. Despite this apparent complications, thanks to its working mechanism, the instrument allows to obtain two- or three-dimensional images of the sample's topography and can provide also quantitative information on the height, length, width or volume of any feature in the image.

The main components of an Atomic Force Microscope are the following [33]. First of all, the probe which is usually a sharp tip mounted on a soft cantilever spring. In this way, the interaction between the tip and the sample can be monitored by analyzing the motion of the cantilever. It is thus also required a device to sense and quantify the cantilever's deflection upon interaction with the sample. A feedback system should also be included to monitor and control the deflection. Moreover, AFM also include a mechanical, usually piezoelectric, scanning system capable of moving the sample with respect to the tip in a raster pattern and allowing corrections on the target placement based on the feedback system. Finally, a display system to convert the measured data into actual images iS included. Commonly used materials for AFM probes are silicon nitride (Si_3N_4), silicon (Si) or other materials with low thermal expansion coefficients. In general, the sharpness and reproducibility of manufactured probes are the most limiting factors on the quality of AFM results. Besides, although the resolution of the final image can be improved with sharper probes, the production of probes with a reproducible tip radius below 10 nm at a reasonable cost it still a major challenge [32].

The detection of the cantilever bending can be carried out in several different ways. The first AFM devices, like the one introduced by Binnig, used tunneling tips placed above the conductive surface of the cantilever. Although this method is very sensitive, most of the subsequent systems were based on simpler optical techniques like interferometry or light beam deflection, which do not require the tip to be conductive. Interferometric techinques are more sensitive but also more complicated than the so-called "beam-bounce method". This method exploits the reflection of an optical beam, emitted by a laser source, from the mirrored surface on the back side of the cantilever onto a position-sensitive photodetector. In this configuration, the tilt of the cantilever upon interaction with the sample can be quantified through the changes in position of the beam

on the photodetector [34]. In Fig. 2.3 it is reported the general scheme of an AFM with beam-bounce detection like the one used in this work.

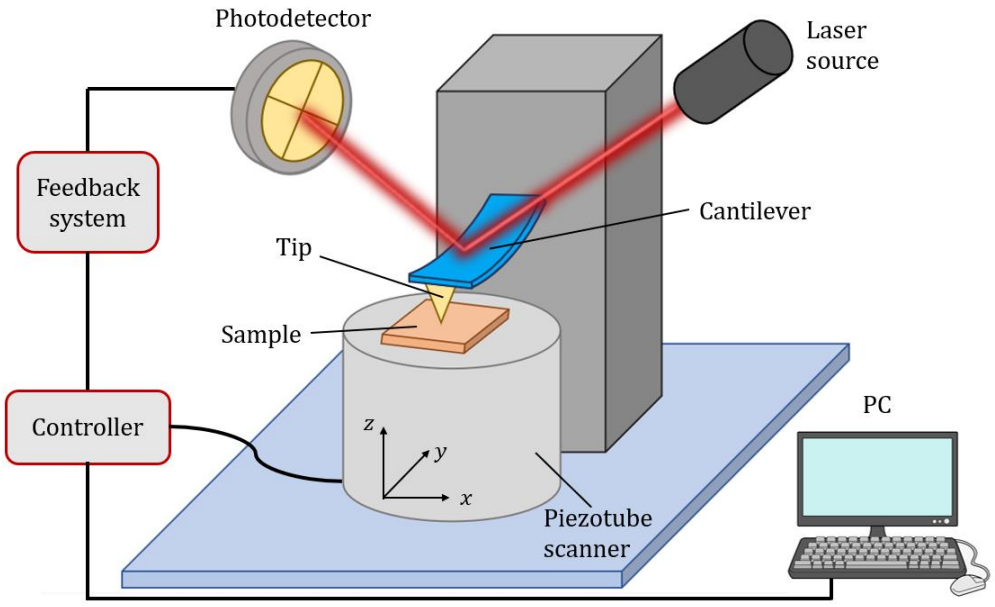

Figure 2.3: General scheme of an Atomic Force Microscope working on beam-bounce detection. The position-sensitive photodetector is made up of 4 photodiodes and the reflected beam is aligned on its center prior to measures. Deviations from this configuration due to cantilever bending can thus be quantified.

To perform AFM measurements, depending on the sample-tip distance and interaction regime, three different operation modes can be exploited: *contact* mode, *non-contact* mode and *tapping* mode. These three regimes are summarised in Fig. 2.4 together with a simple plot showing the evolution of the sample-tip interaction as a function of their distance. It can be seen that when the tip is far from the sample surface, the interaction is basically null and the cantilever is considered to have zero deflection. However, as the tip approaches the surface, it is firstly subject to an attractive force, until as the instrument continues to push the cantilever towards the surface, the two get in contact and the interaction moves into the repulsive regime. Contact mode works in this repulsive regime where the tip of the probe is touching the sample. The feedback signal is the deflection of the cantilever. Although working in this regime allows to obtain high resolutions, there is a high risk of damaging both the tip and the sample during the scanning process. For these reasons in some applications it is preferable to work in non-contact mode. In this mode, the cantilever is oscillating at about 10 nm above the surface without touching it. Hence, the tip only interacts through attractive Van der Walls forces which modify both the amplitude and the frequency of oscillations. Therefore, in this mode, amplitude and frequency of the cantilever oscillations can be used as feedback signals. Non-contact mode offers the advantage of degrading neither the tip nor the sample making it more suited for the study of fragile materials. However, because of the low intensity of Van der Walls forces, this mode is often performed under ultra-high vacuum (UHV) making it less versatile. A better solution

is working in tapping mode. In this case the tip is oscillating and touching the surface of the sample. The amplitude and the frequency of the signal can still be used as feedback signals, but compared to non-contact mode, the interaction is stronger making it possible to operate in ambient environment. Compared to contact mode, it has the advantage of being more stable on highly textured surfaces and of reducing the friction force, hence avoiding the degradation of the tip or the sample.

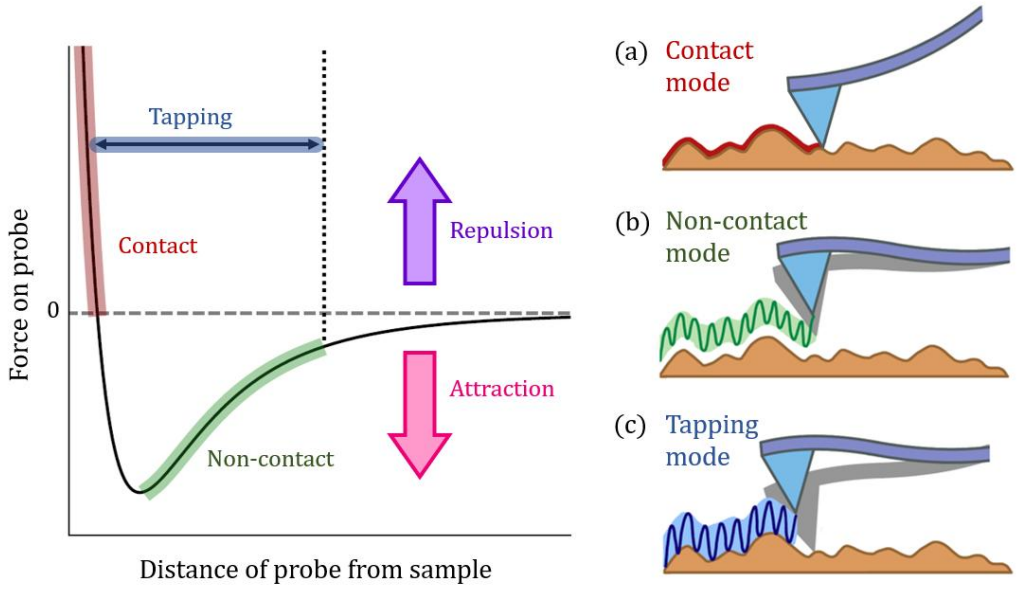

Figure 2.4: The graph on the left shows the evolution of the force applied on the tip by the surface as a function of tip-sample distance. On the right the three main working modes of AFM are schematized. (a) In contact mode the probe operates in the region close to the surface where Coulomb forces are highly repulsive. (b) In non-contact mode the probe is far from the sample and is sensitive to the attractive Van der Waals forces. (c) In tapping mode it oscillates between contact and non-contact region.

AFM imaging is prone to lead to errors in the final image caused by unwanted tip-sample interactions, such as sample movement under the tip or strong tip-sample forces leading to vibration or streaking in the images. These artifacts can also be the result of external forces such as vibration or acoustic noise. Regarding this aspect, the isolation of the setup from external vibrations is fundamental for the good outcome of an AFM measure. To overcome this problem, the microscope is usually equipped with vibration insulation devices. Another source of artifacts in the final image is the tip-sample convolution caused by the finite width of the AFM tip. Some of the artefacts in an AFM image can be corrected via specific routines in AFM processing softwares. These corrections, however, should be carried out carefully especially when trying to obtain quantitative measures from the images as the correction process can alter the data.

For this work a *NT-MDT Solver Pro AFM* operating in non-contact tapping mode is employed to carry out measures while the acquired images are analyzed using the open-source software *Gwyddion* [35]. An example of an AFM surface topography on a Ag/Al_2O_3 multilayer

is in Fig. 2.5(a). A photo of the microscope used in this work is shown in Fig. 2.5(b).

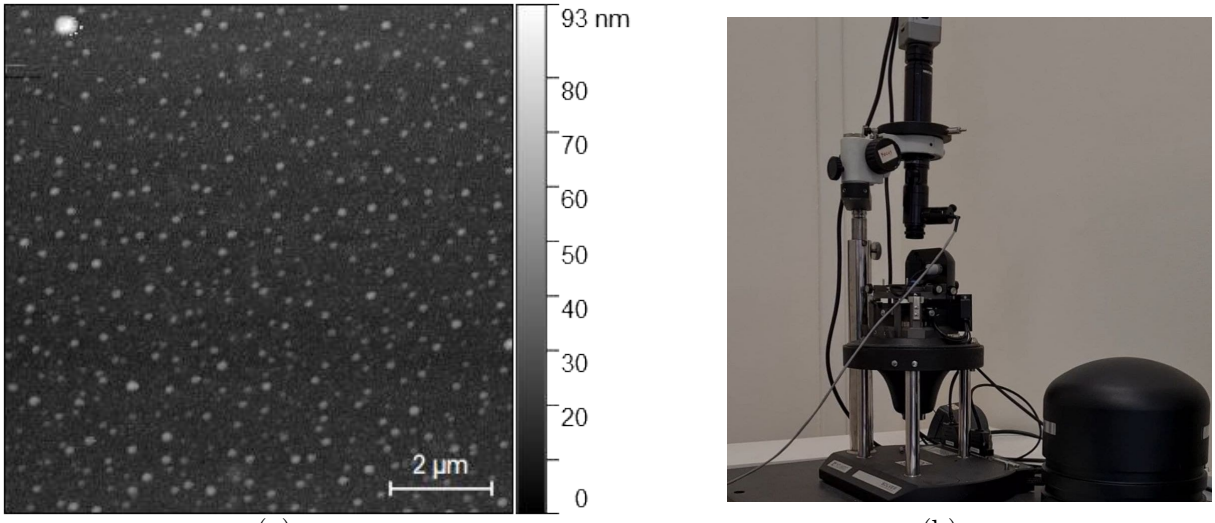

(a) (b)

Figure 2.5: (a) AFM image of the surface of one of the multilayer samples studied in this work. (a) Photo of the Atomic Force Microscope used in this work.

2.2.2 Scanning Electron Microscopy

The Scanning Electron Microscope (SEM) is a tool to create magnified images with nanometric resolution, beyond the diffraction limit of light. These images can provide information on the size and shape but also on the composition, crystallography, and other physical and chemical properties of the specimen. This is all possible thanks to the special working mechanism of SEM which, as opposed to an optical microscope, uses a high energy focused electron beam instead of visible light. The principle of the SEM was originally demonstrated by *M. Knoll* in 1935 and the first working SEM was developed in 1938 by *M. von Ardenne*.

In this microscope, a finely focused beam of energetic electrons is firstly emitted from an electron source. The energy of these electrons is typically between 0.1 keV and 30 keV. The electrons are then accelerated to high energies and the shape of the beam is controlled and modified by a system of apertures, magnetic and/or electrostatic lenses, and electromagnetic coils specifically placed to increasingly reduce the beam diameter. This special system of lenses is also used to scan the focused beam in a raster pattern, placing it sequentially at a series of closely spaced locations on the sample. In this scanning process, the interaction of the electron beam with the specimen produces two main outgoing electron products: backscattered electrons (BSEs) and secondary electrons (SEs). BSEs are beam electrons emerging from the specimen after being scattered and deflected by the atoms in the sample. On the other hand, SEs are electrons escaping the specimen surface after being ejected from atoms in the sample by beam electrons. These outgoing electron signals are measured at each point with specific detectors. Usually a "secondary electron" detector (which is actually sensitive to both SEs and BSEs) and a dedicated "backscattered electron detector" insensitive to SEs are both present. Finally, the signal is digitized to form the final image.

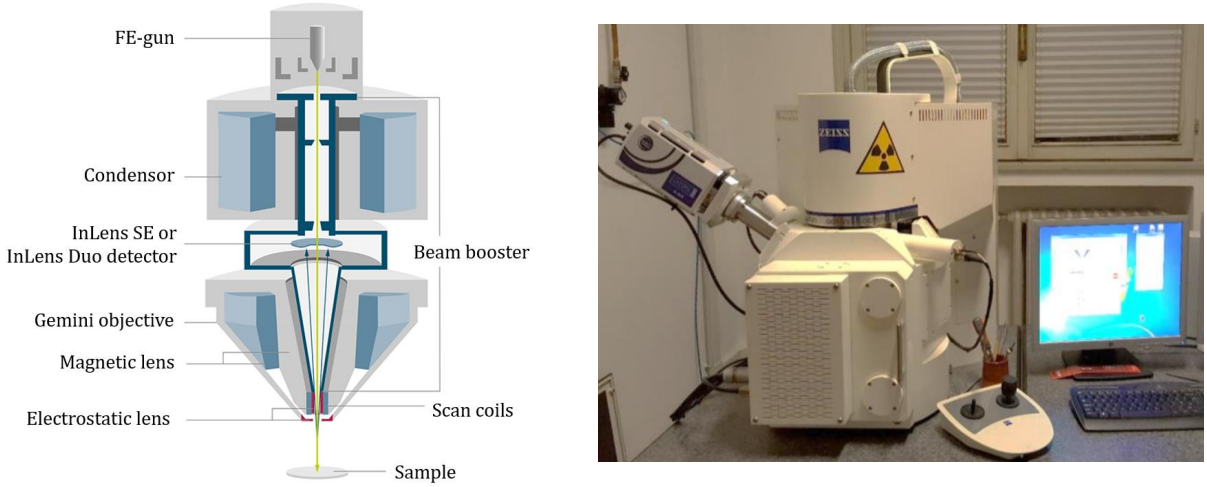

Figure 2.6: (a) Schematic crosssection of the *Gemini optical column* of the *Zeiss Sigma HD FE-SEM* used in this work. Picture from [36]. (b) Photo of the microscope.

In order to minimize the unwanted scattering of beam electrons as well as BSEs and SEs with atoms and molecules of atmospheric gasses, the electro-optical column and the specimen chamber must operate under high vacuum conditions ($< 10^{-4}$ Pa). Furthermore, when working with insulating specimens a properly grounded conductive coating is required to provide an electrical discharge path, otherwise the sample would develop surface electrical charge because of impact of the beam electrons [37]. The SEM images of the samples analyzed in this work are all acquired using a *Zeiss Sigma HD field emission microscope* (FE-SEM) and the annexed software *Smart-SEM*.

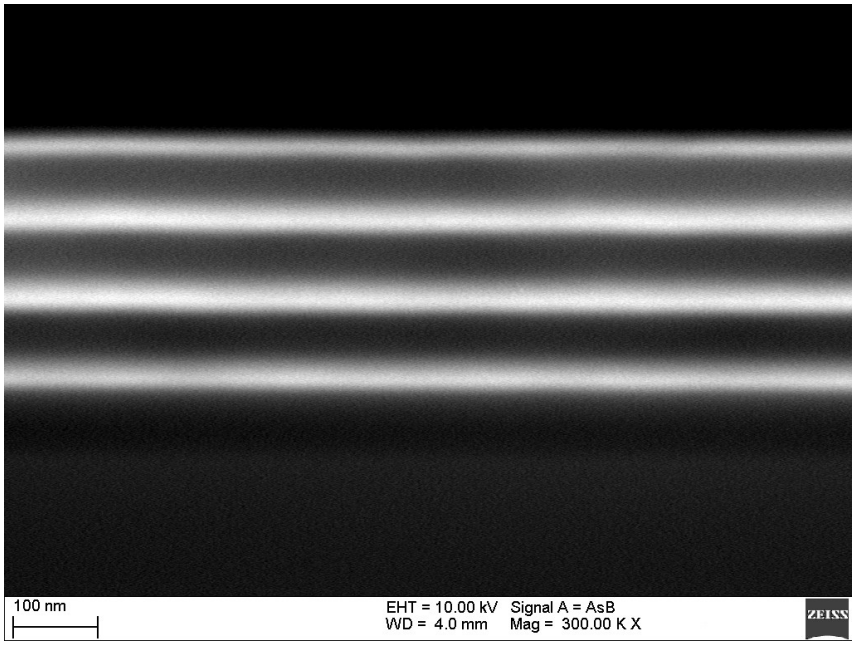

Figure 2.7: SEM image of the cross section of one of the multilayer samples studied in this work.

This instrument, shown in Fig. 2.6, is designed with a *Gemini optical column* which has three main components: the beam booster with an integrated beam deceleration, which guarantees small probe sizes and high signal-to-noise ratios, the Inlens detector which detects both secondary (SE) and backscattered (BSE) electrons in parallel minimizing imaging time and ensuring efficient signal detection and finally, the objective lens whose design combines electrostatic and magnetic fields to maximize optical performance while reducing field influences at the sample to a minimum allowing excellent imaging, even on challenging samples such as magnetic materials.

2.2.3 Spectroscopic Ellipsometry

Ellipsometry is an optical measurement technique that uses light reflected from a thin film as a probe to investigate different properties of the sample. It is commonly used to characterize the thickness and dielectric properties of thin films both in the case of single layers or complex multilayer stacks with thicknesses ranging from a few angstroms up to several micrometers. Many are the reasons for the success of this technique, primarily, its high precision of measurement, and very high thickness sensitivity up to ∼0.1 Å. Moreover, spectroscopic ellipsometry is a fast, non-destructive and contactless technique, allowing an accurate characterization of samples without risks of altering the sample itself. The idea behind this technique is to quantify the change in polarization of light upon reflection on a sample to derive information on the thickness and linear optical properties of the sample itself. The name *ellipsometry* derives from the elliptical polarization usually assumed by light upon reflection on a surface [38].

The typical scheme of an ellipsometer is depicted in Fig. 2.8. The light source, equipped with a monochromator, emits light of a specific wavelength. This light is then linearly polarized by a polarizer and hits the surface of the sample at an angle θ. The reflected signal then passes through another polarizer, which is more properly denoted as analyzer, and finally reaches a photodetector. The user can potentially add also other optional compensators like waveplates or phase-retarders between the sample and the two polarizers.

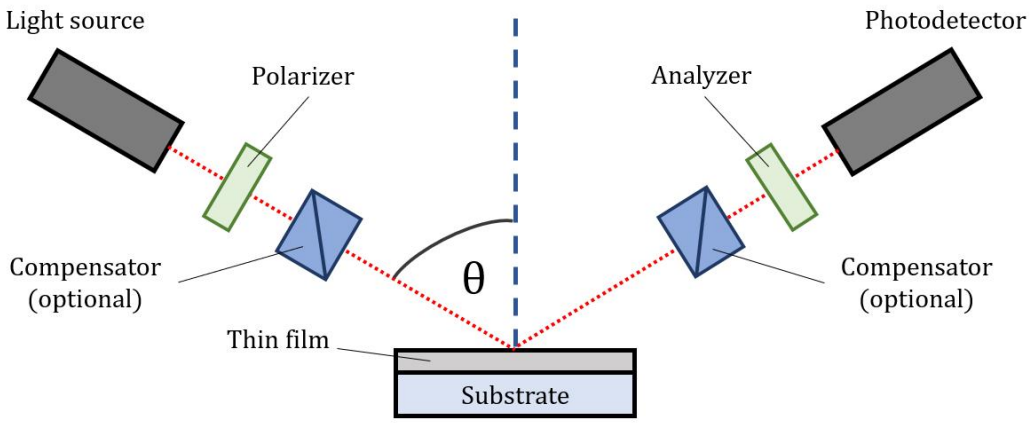

Figure 2.8: Schematic setup of an ellipsometry experiment

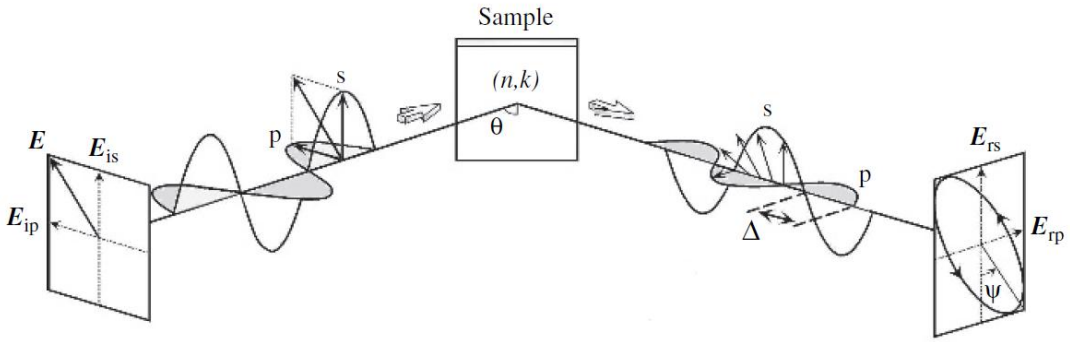

Figure 2.9: Measurement principle of ellipsometry [38]

The state of polarization of the incident and reflected light can then be decomposed into two orthogonal components: the p- and s-polarizations. Denoting as E_{ip} and E_{is} the two p- and s- components of the incident wave and E_{rp} and E_{rs} those of the reflected one, spectroscopic ellipsometry is capable of measuring the changes in these components (and consequently on the polarization state) by measuring the so called *complex reflectance ratio* ρ which is equal to the ratio of the Fresnel coefficients $\tilde{r}_p$ and $\tilde{r}_s$. This ratio can be parametrized by the amplitude component Ψ and the phase difference Δ as in Eq. 2.1 where $\tan\Psi$ quantifies the ratio of the amplitudes upon reflection, and Δ the phase shift.

$$\rho = \tan\Psi \cdot e^{i\Delta} = \frac{\tilde{r}_p}{\tilde{r}_s} = \frac{E_{rp}/E_{ip}}{E_{rs}/E_{is}} \tag{2.1}$$

When a sample structure is simple, the amplitude ratio Ψ is characterized by the refractive index n, while Δ depends on light absorption described by the extinction coefficient k. In this case, the two values (n, k) can be determined directly from the two ellipsometry parameters (Ψ, Δ) obtained from a measurement by applying the Fresnel equations. This basic working principle of ellipsometry measurement is schematized in Fig. 2.9.

In spectroscopic ellipsometry, (Ψ, Δ) spectra are measured at different wavelengths of the incident light. Since this technique measures the ratio (or difference) of two values instead of absolute quantities, it is very robust, accurate, and reproducible. However, there are two general restrictions on ellipsometry measurement. First of all the surface roughness of samples has to be rather small, as light scattering by surface roughness reduces the reflected light intensity severely, making the measuring process more difficult and less precise. Besides, the measurement must be performed at oblique incidence, at angles specifically chosen to maximize the sensitivity for the measurement. The choice of this incidence angle depends on the optical constants of the samples. Furthermore, at normal incidence, the ellipsometry measurement becomes impossible, since p- and s-polarizations are indistinguishable [38]. The main drawback of ellipsometry lies in the indirect nature of this characterization method: to properly analyze ellipsometry data, an *a-priori* optical model of the sample, defined by the optical constants and layer thicknesses, must be known. The data analysis can then provide a better estimate of the thicknesses and dielectric function, allowing to perform a correction of the model but an approximate knowledge

of the materials and their thicknesses is fundamental to interpret the data.

The instrument employed in this work is a Variable Angle Spectroscopic Ellipsometer (V-VASE) by J. A. Wollam Co. It is a traditional rotating analyzer ellipsometer (i.e. the input polarizer is fixed while the analyzer can continuously rotate) allowing measurements over a wide spectral range between 185 nm and 1700 nm. The software *WVASE32* has been used for the data analysis [39]. It allows to build a virtual model of the sample under examination by specifying the substrate, the constituent materials of each film and their thicknesses. Then, once the data collected by the instrument is uploaded, it allows to plot both the experimental and simulated curves (based on the previously specified model). Moreover, one can set the thickness t or the dielectric functions (the refractive index n and the extinction coefficient k) as fitting parameters to let the software determine their best estimate. More complex models depending on other possible parameters besides t, n and k can also be built, considering surface roughness, various non-uniformities in the films, effective media and so on. Since strong correlations may exist between some of these parameters, it is advisable to leave the least possible number of free parameters in the fitting procedure to get more accurate results.

The instrument also allows to measure transmittance and reflectance spectra.

2.2.4 Z-scan technique

The z-scan technique was firstly proposed in 1989 by *M. Sheik-Bahae et al.* [40, 41] as a simple and sensitive single-beam method for measuring both the sign and magnitude of the real and imaginary parts of the complex nonlinear refractive indexes $\tilde{n}_2$ of optical materials. The idea behind this technique is to change the incident intensity on the sample by translating it along the propagation direction of a focused laser beam, which is denoted as z axis, hence the name of the technique. Due to the nonlinear response of the sample, the transmitted intensity in the far-field will change in this translation process as a function of the incident intensity. By recording this transmittance as a function of the z-coordinate it is thus possible to acquire information about the nonlinear optical parameters. To determine both the nonlinear absorption coefficient β and the nonlinear refractive index n_2, which are related to the imaginary and real part of the complex nonlinear refractive index $\tilde{n}_2$ respectively, the measurement has to be performed in two different configurations called *Open Aperture* (OA) and *Closed Aperture* (CA) respectively. In the former, the whole transmitted intensity is collected by a photodetector, allowing to quantify changes in transmittance due to nonlinear absorbtion. On the other hand, to quantify nonlinear refraction, the measurement has to be sensitive to phase distortions. For this reason, a finite aperture must be placed in front of the detector in the CA configuration. Using both configurations during the same z-scan measure, for example using a beam splitter, the technique allows to quantify both β and n_2 simultaneously.

For the case of pure nonlinear absorption, as shown in Fig. 2.10(a), both OA and CA transmittance curves exhibit a completely mirror-symmetric shape about the focus. Specifically, in the case of saturable absorprion (SA), i.e. when $\beta < 0$, since transmittance increases with the incident intensity, the curves present a peak at the focus.

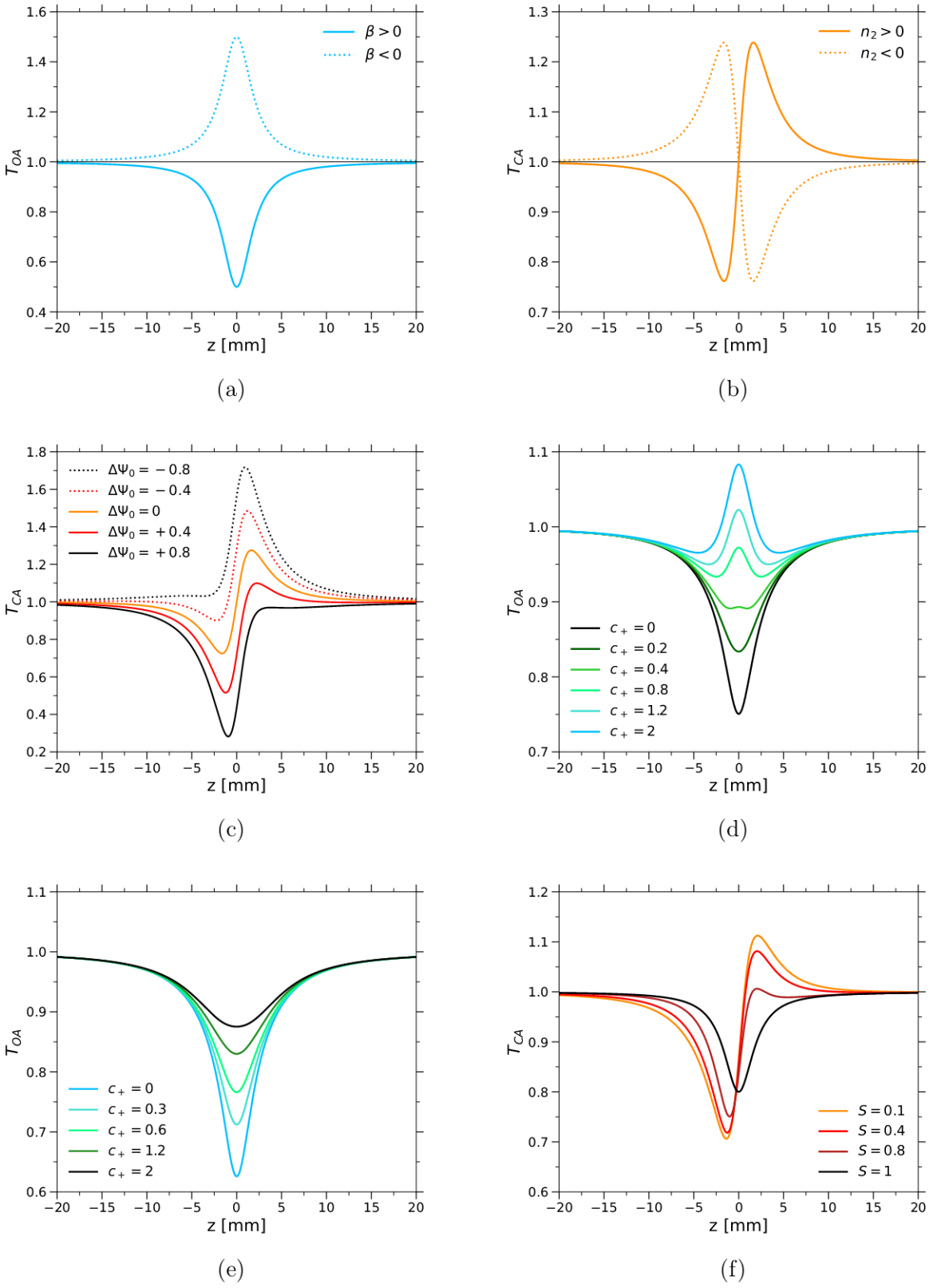

Figure 2.10: Simulations of the various effects influencing a z-scan curve with focus at $z = 0$ mm and Rayleigh range of $z_0 = 2$ mm. (a) Pure nonlinear absorption for $\beta \lessgtr 0$. (b) Pure nonlinear refraction for $n_2 \lessgtr 0$ and $S = 0.3$. (c) Effect of NLA on a CA curve with $n_2 > 0$. (d) Combination of SA and RSA for increasing values of $c_+ = I_S^+/I_0$. (e) Increasing effect of saturation on a OA curve with $\beta > 0$. (f) Effect of the aperture size on a CA curve for increasing values of S.

On the contrary, for reverse saturable absorption (RSA), i.e. $\beta > 0$, transmittance decreases when approaching the focus, leading to a valley-shaped curve. Besides, for the case of pure nonlinear refraction, the OA transmittance curve is flat as transmittance is always constant at any position. The CA curve, on the other hand, is centrally symmetric about the focus as shown in Fig. 2.10 (b). In particular, in the case of self-defocusing when the sample is brought closer to focus, the self-lensing prior to focus will tend to collimate the beam, causing a beam narrowing at the aperture which results in an increase in the measured transmittance. As the scan in z continues and the sample passes the focal plane to the right, the same self-defocusing increases the beam divergence, leading to beam broadening at the aperture, and thus a decrease in transmittance. Thus for $n_2 < 0$ the CA curve has a peak in the pre-focal region and a valley after it. The opposite process occurs for a self-focusing sample with $n_2 > 0$: in this case a valley/peak configuration can be observed. It is thus clear how one can immediately infer also the sign of these nonlinear parameters by simply looking at the shape of the OA and CA curves. In practice, however, in almost all materials nonlinear refraction and nonlinear absorption are both present, leading to an asymmetric CA curve with enhancement or suppression of the peak/valley configuration. For example the simulations in Fig. 2.10(c) show how in a CA curve with $n_2 > 0$ the presence of RSA ($\beta > 0$) leads to valley enhancement and peak suppression whereas the opposite occurs with SA ($\beta < 0$). If the entity of nonlinear absorption in a sample becomes very significant in comparison to its nonlinear refraction, the peak/valley shape will disappear, giving rise to a single asymmetric valley or peak. For the OA curve, deviations from the standard curves in Fig. 2.10(a) can be observed when both components of nonlinear absorption, namely SA and RSA, are present leading to a curve which looks like the convlution of a $\beta > 0$ and a $\beta < 0$ OA curve as in Fig. 2.10(d). This may happen when the two components of the NLA coefficient with opposite sign are activated at different intensities or at different wavelenghts [26, 42]. In this case β cannot be simply described by a purely constant value but one must resort to Eq. 1.37. This equation also accounts for possible saturation effects of the nonlinear components when higher order nonlinearities are activated as the incident intensity overcomes a certain threshold. These saturation effects manifest themselves as a broadening in the OA curve as displayed in Fig. 2.10(e) for increasing values of the parameter $c_+ = I_S^+/I_0$ (see Eq. 1.37).

In spite of its simplicity, the z-scan technique requires careful attention to some important experimental factors which may lead to unreliable data and poor spatial profiles if neglected [43]. Among the most important:

(i) Good knowledge of the input beam spatial profile is highly important as deviations from a Gaussian profile might lead to artifacts, especially in the measurement of nonlinear refraction which relies on measuring distortions of the spatial profile of the beam. To improve beam quality, a spatial filter is usually placed before the z-scan line;

(ii) A good understanding of the temporal characteristics of the laser is also vital in any pulsed laser measurement. Indeed, when the response time of the nonlinearity is larger than the laser pulse width, thermal nonlinearities are likely to dominate over the electronic ones. The same occurs due to cumulative effects when repetition rates are too high. Usually, to

have nonlinear refraction influenced by electronic effects only, z-scan measurements should be performed with a repetition rate of few tens of Hz and pulses of ∼10 ps [44];

(iii) Fluctuations in the laser power are also a major cause of noisy z-scan curves, making the analysis more complicated and less reliable. A common solution to this problem is the introduction of a reference detector before the z-scan line and the normalization of the transmitted signals by the reference one. This usually leads to a cleaner signal. However, having a sufficiently stable input signal is still quite important as different nonlinear effects might be triggered at different intensities. The laser power should not vary by more than a few percent;

(iv) The linear transmittance of the aperture should be of about $0.2 \div 0.4$ to be able to distinguish NLR from NLA with good resolution as shown by Fig. 2.10(f). The distance of the aperture and the sample alignment are also crucial to obtain a good measurement: the aperture must be placed in the far field with the aperture centered on the optical axis of the beam;

(v) Imperfections in the samples might also cause variations in transmittance which are not related to the nonlinear response. Careful attention must be put in verifying that the sample presents no scratches and has limited roughness and irregularities;

(vi) Too high laser power are also problematic as they might set off higher order effects, as previously said, or even damage the sample leading to artifacts in the measures.

Several analytical expressions have been proposed for the fitting of experimental z-scan curves and the determination of the parameters β and n_2. For the present work, the method proposed by *Guo et al.* [45, 26] is followed. This method can be used when dealing with standard on-axis transmission z-scan measurements in which the input laser beam has a Gaussian profile. Moreover, it is only effective in the "thin" sample approximation, which means that the thickness of the sample must be small enough that a change of the beam diameter within the sample due to either diffraction or nonlinear refraction can be neglected. If the sample's thickness is L, for the approximation to be verified one must have $L \ll z_0$ for linear diffraction and $L \ll z_0/\Delta\Phi_0$ for nonlinear refraction where $z_0 = \frac{\pi w_0^2}{\lambda}$ is the Rayleigh length of the focused Gaussian beam and w_0 is the beam waist. Under these hypothesis the normalized transmittance T_{CA} can be written as:

$$T_{CA} = 1 + \frac{(1-S)^{\mu}\sin\xi}{S(1+x^2)}\Delta\Phi_0 - \frac{1-(1-S)^{\mu}\cos\xi}{S(1+x^2)}\Delta\Psi_0 \tag{2.2}$$

where:

$$\mu = \frac{2(x^2+3)}{x^2+9} \tag{2.3}$$

$$\xi = -\frac{4x\ln(1-S)}{x^2+9} \tag{2.4}$$

$$\Delta\Phi_0 = \frac{2\pi}{\lambda} n_2 I_0 L_{\text{eff}} \tag{2.5}$$

$$\Delta\Psi_0 = \frac{1}{2\sqrt{2}} \beta I_0 L_{\text{eff}} \tag{2.6}$$

where S is the linear transmittance of the finite aperture in front of the CA detector, which depends on the radius of the aperture r_a and the beam radius at the aperture w_a as in the expression below:

$$S = 1 - \exp\left(-\frac{2r_a^2}{w_a^2}\right) \tag{2.7}$$

Moreover, $x = \frac{z}{z_0}$ is the dimensionless relative position along the beam propagation direction of the sample with respect to the focus of the converging lens normalized to the Rayleigh range z_0. I_0 is the on-axis intensity of the laser beam at the focus and L_{eff} is the effective length of the sample, which depends on the real sample length L and its linear absorption coefficient α_0 as follows:

$$L_{\text{eff}} = \frac{1}{\alpha_0}\left(1 - \exp\left(-\alpha_0 L\right)\right) \tag{2.8}$$

When no aperture is placed in front of the detector as in an OA measure, the linear transmittance is $S = 1$ and Eq. 2.2 is reduced to the conventional expression given by *Sheik-Bahae et al.* [41]:

$$T_{OA} = 1 - \frac{\Delta\Psi_0}{1 + x^2} = 1 - \frac{\beta I_0 L_{\text{eff}}}{2\sqrt{2}(1 + x^2)} \tag{2.9}$$

Theoretically, one could use Eq. 2.2 to fit both the nonlinear refractive index n_2 and the nonlinear absorption coefficient β from just the CA curve. Nonetheless, to minimize the number of degrees of freedom in the fitting procedure therefore obtaining a much more reliable estimate of the nonlinear parameters, in this work the OA and CA scans are fitted separately with Eqs. 2.9 and 2.2 respectively. Besides, to get consistent results between the two classes of scans, it was decided to carry out firstly the fits of the OA curves. Then, these parameters are fixed when fitting the correspondent CA curves.

The z-scan setup used in this work is schematically represented in Fig. 2.11. The beam source is a high-energy water-cooled and flashlamp-pumped Nd:YAG laser (*Leopard* by *Continuum*). The laser is passively mode-locked and emits 18 ps pulses with a repetition rate of 10 Hz this allows to activate in the sample only electronic nonlinearities without triggering thermal ones. The fundamental wavelength of emission is at 1064 nm but the laser is also equipped with modules for second and third-harmonic generation allowing emission also at $\lambda_{2\omega} = 532$ nm and $\lambda_{3\omega} = 355$ nm respectively. For this work, the third harmonic is used to pump an Optical Parametric Amplifier (OPA) (*TOPAS* by *Light Conversion*), a device that allows to convert the input beam into one with a different wavelength exploiting difference frequency generation in a birifrangent crystal (lithium triborate LiB_3O_5 in this case). The device is connected to a computer and can be controlled through the software *WinTopas4* that allows to set the wavelength of the output beam in the range $420 \div 2400$ nm by rotating the nonlinear crystal.

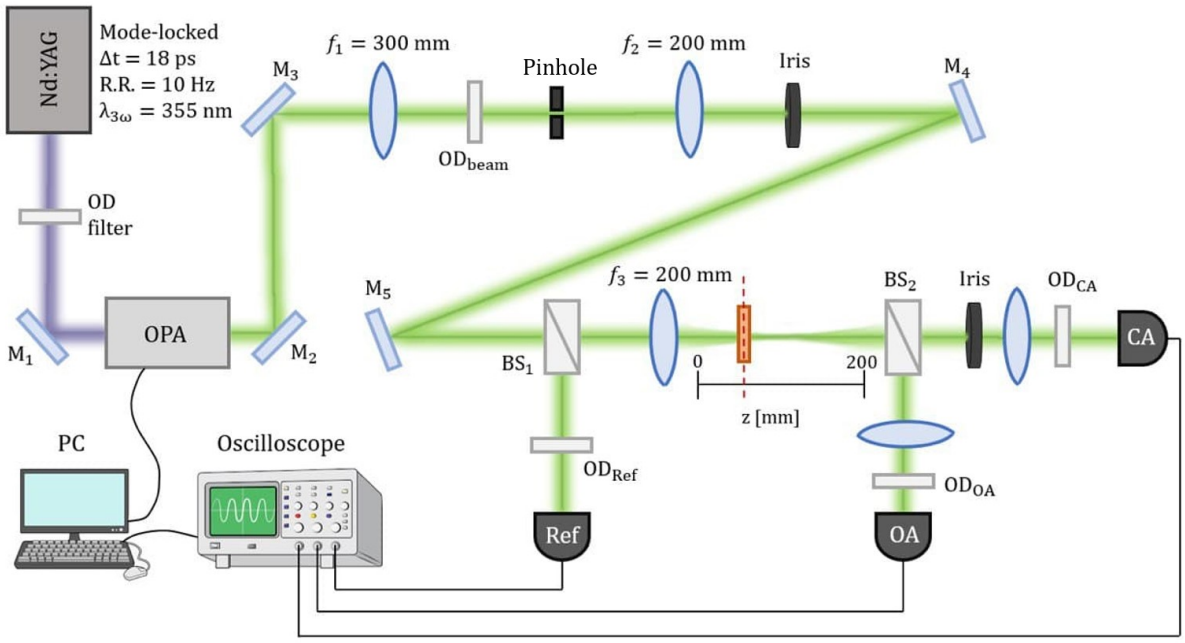

Figure 2.11: Scheme of the z-scan setup employed in this work

The output beam at the desired wavelength is then spatially filtered to select the TEM_{00} mode and have a uniform, circular beam spot. This spatial filter is made up of a pinhole placed between two converging lenses at their common focal point and followed by an iris diaphragm. The two lenses have focal lengths $f_1 = 300\,\text{mm}$ and $f_2 = 200\,\text{mm}$ respectively. OD filters can be placed before it to reduce the intensity of the incident beam (OD_{beam}) and prevent damages to the pinhole. This "spatial filter line" is followed by the actual "z-scan line" where the samples is mounted orthogonally with respect to the z-direction, on a motorized sample holder which can translate along the z-direction by 200 mm. This motorized stage is preceded by another converging lens with focal length f_3 =200 mm placed at a distance such that the focus of the lens is at the center of the line ($z \sim 100\,\text{mm}$). A beam splitter BS_2 is then used to send the transmitted beam to two photodetectors: the open-aperture detector OA and the closed aperture one CA which is preceded by an iris diaphragm with linear transmittance $S \sim 0.282$. Before each detector it is placed a lens and, optionally, some OD filters (OD_{OA} and OD_{CA}) to reduce the incident intensity and avoid detector saturation. To reduce the noise caused by fluctuations in the signal's intensity, another beam splitter BS_1 is placed before the first lens to send a reference signal to a third detector (Ref). The OA and CA signals are then normalized to this Ref signal. All three signals are recorded by a digital oscilloscope (*Tektronix TDS7104 Digital Phosphore Oscilloscope*) which is also connected to a computer where a dedicated software (*Move & Measure*) allows both to translate the sample and to record signals as a function of its position. The trigger is fixed on the Ref channel and the integral of the signal pulse is collected. To reduce noise, many signals are collected at each z coordinate (at least 150-200 pulses) and their average is recorded. The software allows to set the range over the z-axis on which measures are collected, the motion step and the number of signals to record at each position.

Knife-edge method

As previously mentioned, to obtain reliable z-scan measurements it is fundamental to work with a Gaussian beam. To check if this requirement is fulfilled and to obtain an accurate measurement of the beam waist, before carrying out the z-scan measurements, a characterization of the laser beam parameters is performed with the *knife-edge method* [46, 47]. This technique allows to obtain a spatial profile of the beam along its propagation direction and compare it with that predicted by theory for an ideal Gaussian beam. By doing this, it is possible to estimate the beam diameter, its divergence and the M^2 factor which is $= 1$ for an ideal Gaussian beam.

In this method, a sharp blade is moved perpendicular to the direction of propagation of the laser beam, and the total transmitted power is measured as a function of the knife-edge position. This intensity is measured by a photodetector and normalized to a reference signal (quantifying the whole beam intensity).

If the incident beam is a radially symmetric Gaussian laser beam its incident intensity can be described, in a Cartesian system of reference with the $\hat{\mathbf{z}}$ axis along the propagation direction of the laser, by:

$$I(x,y) = I_0 \exp\left[\frac{(x-x_0)^2 + (y-y_0)^2}{w}\right] \tag{2.10}$$

where I_0 is the peak intensity at the center of the beam, located at (x_0, y_0), x and y are the transverse Cartesian coordinates, and w is the beam radius [47]. With the knife-edge blocking the laser beam at a position x, the average transmitted power will be given by the integral of the intensity on the area left free by the knife, which, if normalized to the total power of the reference signal, is:

$$P_N(x) = \frac{\int_{-\infty}^{x}\int_{-\infty}^{\infty} I\,(x',y)\,dydx'}{\int_{-\infty}^{\infty}\int_{-\infty}^{\infty} I\,(x',y)\,dydx'} \tag{2.11}$$

which gives the following expression for the normalized transmitted power as a function of the position x of the blade:

$$P_N(x) = y_0 + A \cdot \mathrm{erf}\left(\frac{\sqrt{2}(x-x_0)}{w}\right) \tag{2.12}$$

where A is a constant. By plotting the normalized power P_N as a function of the position x of the knife-edge and fitting with the error function in Eq. 2.12 one can find the value of the beam radius w at a certain z position along the propagation direction, as shown in Fig. 2.12(a). By repeating this procedure for different z positions it is possible to reconstruct the beam profile by plotting $w(z)$. These data can then be fitted to derive the experimental values of M^2 and the beam waist w_0 with the following expression:

$$w(z) = w_0\sqrt{1 + \left(M^2\frac{\lambda(z-z_0)}{\pi w_0^2}\right)^2} \tag{2.13}$$

where λ is the wavelength and z_0 the position of the beam waist.

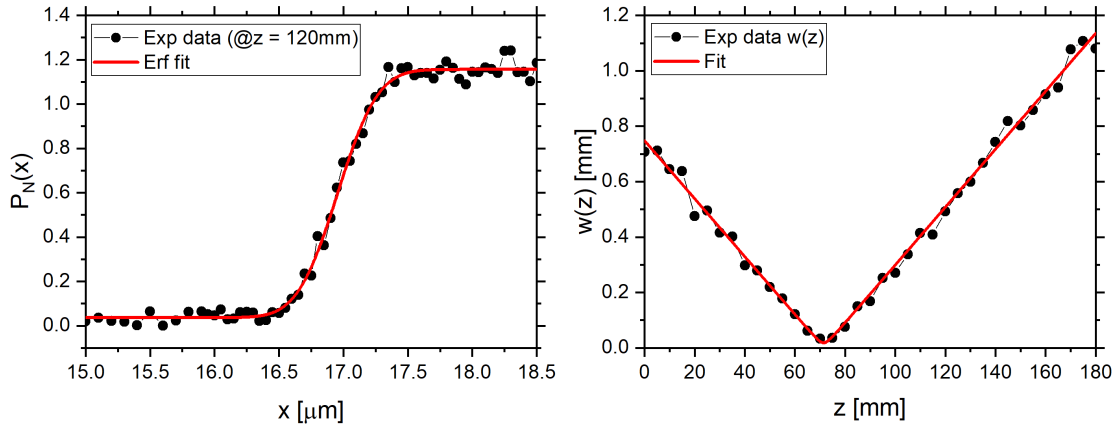

(a) (b)

Figure 2.12: (a) Normalized transmitted power as a function of the x position of the knife edge measured at $z = 120$mm and fitted (red curve) with an *erf* function (Eq. 2.12). (b) Beam radius as a function of the z position fitted with the function in Eq. 2.13 (red curve).

To calibrate the setup used in this work, the procedure is carried out at λ =600 nm and returned an estimation of the beam waist of w_0 =18.82 µm and $M^2 = 1.0$, hinting a good quality of the Gaussian beam. The fit that lead to these results is shown in Fig. 2.12(b).

Chapter 3

Morphological characterization and linear optical response

In this chapter, the preliminary steps of analysis required to correctly evaluate the nonlinear response of the samples are reported and discussed.

Firstly, the morphological characterization obtained from the analysis of AFM and SEM images is reported. Then, the linear optical response, characterized using spectroscopic ellipsometry, is also studied. This same procedure is followed firstly on reference samples and then for the multilayer hyperbolic metamaterials

3.1 Structure and synthesis of the samples

For this work, two types of multilayer hyperbolic metamaterials are synthesised. The two of them only differ in the choice of the dielectric: alumina (Al_2O_3) in one case and silica (SiO_2) in the other. The metal deposited, on the other hand, is silver (Ag) in both samples. Moreover, the multilayers share the same structure as they are made up of four repeated metal-dielectric bilayers with nominal thicknesses of 16 nm for the Ag layer and 85 nm for the dielectric one. The metal filling fraction as defined in Eq. 1.13 would thus be $f_m = 16\%$ for both. A scheme of this structure is shown in Fig. 3.1. Since in both cases the top layer is Ag, which is prone to oxidation if left exposed, an additional 4 nm Al_2O_3 capping layer is deposited on top of the whole structure. The multilayers are built on two types of substrates: monocrystalline silicon (Si) or soda-lime glass (SLG). Both types of substrates are required at different steps of the analysis as a transparent substrate such as SLG is required to carry out measurements in transmittance (e.g. z-scan) whereas a reflective one like Si is more suited for measurements in reflectance (e.g. ellipsometry). This structure was chosen because it has been proven that four is the smallest number of periods required to have a system that adequately approximates the hyperbolic dispersion and the effective medium response [48].

The synthesis procedure begins by preparing the substrates for the deposition by placing them in an acidic Piranha solution (H_2O_2:H_2SO_4, 1:3) for an hour at 80 °C. This hydrogen peroxide-sulfuric acid solution has a double purpose: removing external impurities, which would

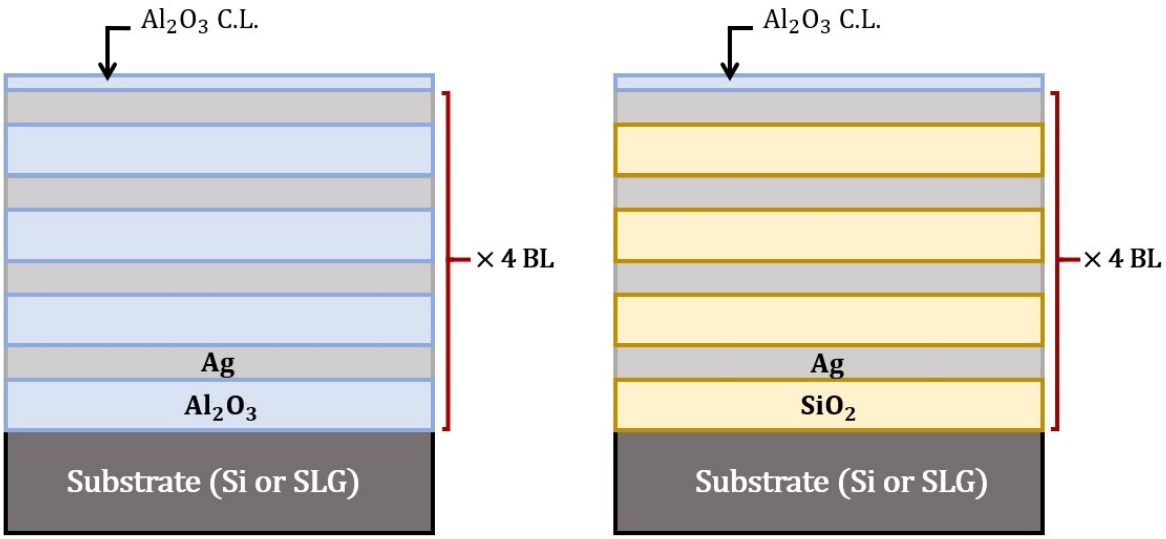

Figure 3.1: Simple scheme of the structure of the two multilayer hyperbolic metamaterials. The thickness of the silver layer is 16 nm while the dielectric layers have 85 nm thicknesses. A 4 nm Al_2O_3 capping layer (C.L.) is also present on top to protect the uppermost Ag layer from oxidation.

impact negatively the quality of the deposition; and hydrophilize the surface of the substrates to promote adhesion of sputtered atoms. The substrates are then rinsed with Milli-Q water until all residues of the acidic solution are removed.

After these preliminary steps, some calibration depositions are performed to determine the best working conditions allowing a uniform deposition with controlled thickness for all sputtered materials. Since there is a linear relationship between deposition time and deposited thickness, the deposition rate for a certain material can be calculated by simply sputtering the chosen material for a specific time interval. Then the exact thickness of the synthesised layer is measured via atomic force microscopy (AFM). The deposition rate for that material, in the experimental conditions set inside the chamber, can finally be calculated as the slope of the deposited thickness vs deposition time. To measure this thickness, if the sputtered layer is Ag, one can simply make a scratch on the surface of the sample to expose the substrate and create a step from the substrate to the top of the sputtered layer. This step can be measured via AFM. This same procedure cannot be followed for Al_2O_3 or SiO_2 which are too hard to be scratched. In this case, to create the step, a marker line is made on the substrate before the deposition and then removed using a solvent. The optimal working parameters set for the synthesis of the three sputtered materials considered are reported in Tab. 3.1. During the synthesis, the Al_2O_3 and SiO_2 torches are kept turned on with the shutter closed when Ag is being deposited. This is done to minimize as much as possible the thermal stress on the dielectric targets, which might suffer from repeated switches of the torch power. A photo of the two types of multilayers, deposited on a soda-lime glass substrate (SLG), is shown in Fig. 3.2.

Having completed the synthesis procedure, other AFM measurements are carried out on the samples to verify their quality. Firstly, their global thicknesses is determined by measuring the step between substrate and top layer as previously done for the calibration samples. Unfortu-

	Ag	Al_2O_3	SiO_2
Ar pressure	$5 \cdot 10^{-3}$ mbar	$5 \cdot 10^{-3}$ mbar	$5 \cdot 10^{-3}$ mbar
Sample holder distance	7.5 cm	7.5 cm	7.5 cm
Sample holder rotation	On	On	On
DC torch power	20 W	—	—
DC torch tilt	16°	—	—
RF torch power	—	150 W	100 W
RF torch tilt	—	16°	16°
Pre-sputtering time	60 s	120 s	180 s
Deposition rate	1.948 Å s^{-1}	0.389 Å s^{-1}	0.408 Å s^{-1}

Table 3.1: Working parameters set during the magnetron sputtering depositions of the three deposited materials.

nately, with this method, only the global thickness of the stack can be measured, not that of each individual layer. Additionally, surface topographies are collected to determine the superficial roughness. This step is very crucial: surface roughness should be at most a few nanometers because bigger values would lead to excessive scattering of light at the surface, with negative impact on the quality of ellipsometric and z-scan measurements. This is especially problematic when depositing silver as its growth mode is characterized by island formation (see Appendix A) and the roughness tends to propagate from a lower layers to those above it. Deviations from the ideal models are thus expected. Besides, as reported in Section 2.2.3, an *a-priori* knowledge of structure and composition of the sample is fundamental for an accurate determination of the film's thicknesses and dielectric functions. For these reason a first thorough characterization of some reference samples is also carried out before stuying the actual multilayer hyperbolic metamaterials. The simplest reference films considered are single layers of Ag, Al_2O_3 and SiO_2 with thicknesses of 16 nm, 120 nm and 90 nm respectively. Then Ag/Al_2O_3 and Ag/SiO_2 bilayers, both with layer thicknesses of 16 nm/85 nm respectively, are made. Finally two Al_2O_3/Ag/Al_2O_3 and SiO_2/Ag/SiO_2 sandwiches are made. In this case the nominal thicknesses are 50 nm/30 nm/50 nm.

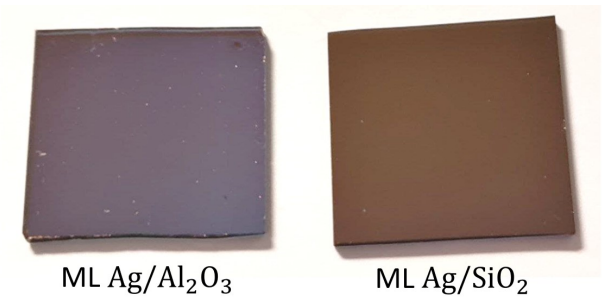

Figure 3.2: Photo of the Ag/Al_2O_3 (on the left) and Ag/SiO_2 (on the right) multilayer hyperbolic metamaterials on a soda-lime glass (SLG) substrate.

The choice of this reference samples is driven by two intents: to indirectly check the evolution of the sample's morphology at different steps of the synthesis process (by making samples with an

increasing number of layers) and to the effects on the growth when the silver layer is thicker (like in the sandwiches). To make the notation less heavy, the samples will be identified as follows:

(a)	**TFAg**	single Ag thin film	16 nm
(b)	**TFAl_2O_3**	single Al_2O_3 thin film	120 nm
(c)	**TFSiO_2**	single SiO_2 thin film	90 nm
(d)	**BLAg/Al_2O_3**	Ag/Al_2O_3 bilayer	(16/85)nm.
(e)	**BLAg/SiO_2**	Ag/SiO_2 bilayer	(16/85)nm.
(f)	**SWAg/Al_2O_3**	Al_2O_3/Ag/Al_2O_3 sandwich	(50/30/50)nm.
(g)	**SWAg/SiO_2**	SiO_2/Ag/SiO_2 sandwich	(50/30/50)nm.
(h)	**MHMAg/Al_2O_3**	Ag/Al_2O_3 multilayer hyperbolic metamaterial with Al_2O_3 capping layer	(16/85) × 4nm. + 4 nm
(i)	**MHMAg/SiO_2**	Ag/SiO_2 multilayer hyperbolic metamaterial with Al_2O_3 capping layer	(16/85) × 4nm. + 4 nm

3.2 Morphology and composition

3.2.1 AFM measurements

The measurements of the step height and of the surface roughness are carried out on different points of the samples and on more than one of the samples synthesised in the same sputtering session. The average values obtained from this analysis are reported in Tab. 3.2. Within the experimental errors, the global measured thicknesses are all comparable with their expected value. Regarding the surface roughness, as expected, it can be seen that generally speaking, the average value increases with the number of layers. An exception to this trend are the two SWAg/Al_2O_3 and SWAg/SiO_2 which, despite of having three layers, are less rough than the corresponding bilayers BLAg/Al_2O_3 and BLAg/SiO_2. This is due to the greater thickness of the silver layer, which is almost two times bigger in the sandwiches with respect to the bilayers.

	Nominal thickness [nm]	**Experimental thickness** [nm]	**Surface roughness** [nm]
TFAg	16	17.4 ± 0.9	1.15 ± 0.05
TFAl_2O_3	120	120 ± 6	0.18 ± 0.01
TFSiO_2	90	93 ± 5	0.39 ± 0.02
BLAg/Al_2O_3	101	103 ± 5	1.79 ± 0.09
BLAg/SiO_2	101	99 ± 5	2.01 ± 0.10
SWAg/Al_2O_3	130	132 ± 7	1.22 ± 0.06
SWAg/SiO_2	130	135 ± 7	0.85 ± 0.04
MHMAg/Al_2O_3	408	—	2.80 ± 0.13
MHMAg/SiO_2	408	402 ± 20	2.02 ± 0.10

Table 3.2: Nominal thicknesses, average experimental thicknesses and surface roughness measured on all samples considered in this work.

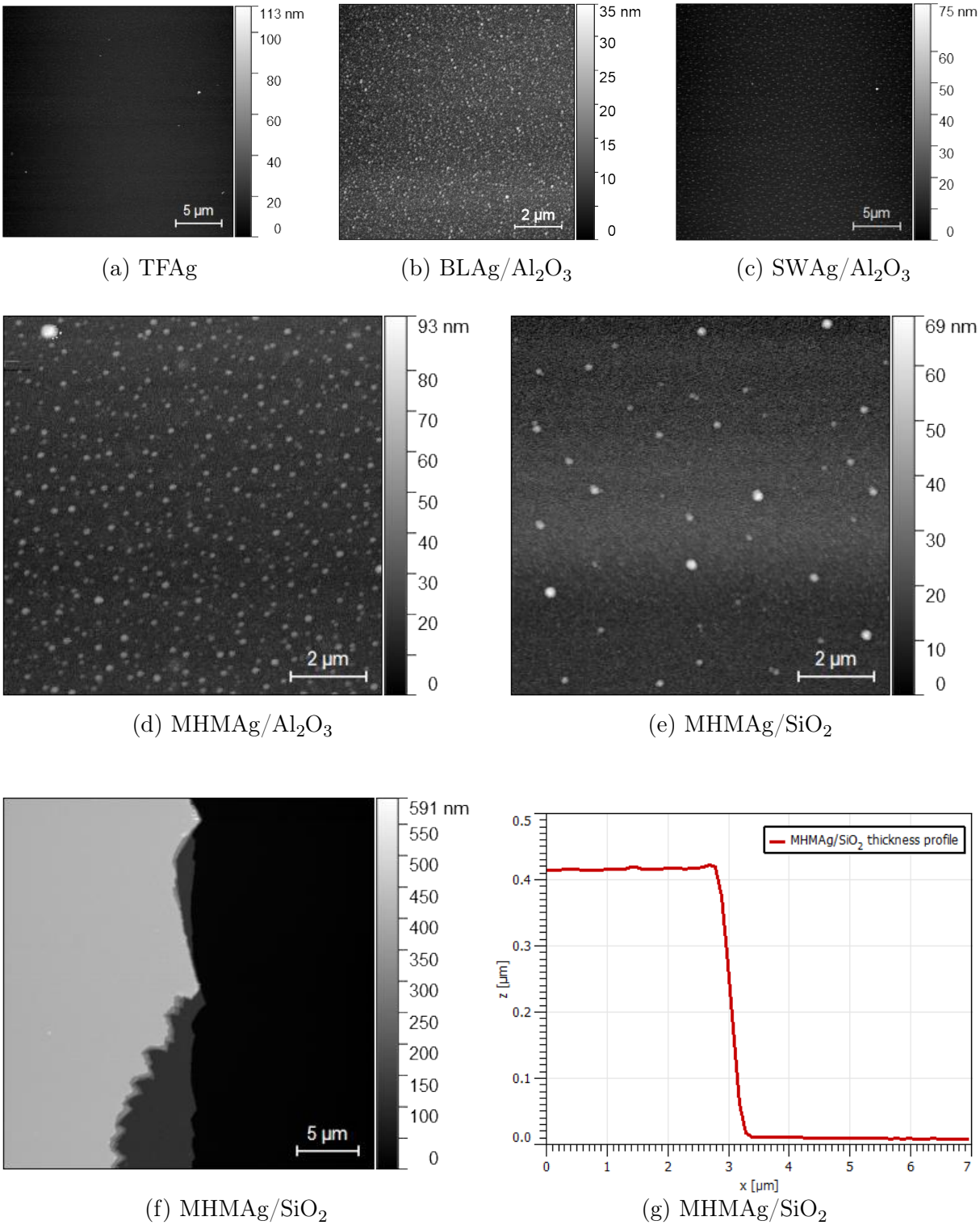

(a) TFAg (b) BLAg/Al_2O_3 (c) SWAg/Al_2O_3

(d) MHMAg/Al_2O_3 (e) MHMAg/SiO_2

(f) MHMAg/SiO_2 (g) MHMAg/SiO_2

Figure 3.3: AFM images acquired on the different samples. (a-e) Surface topographies of the specified samples on Si substrate. (f) Image of the step produced on the MHMAg/SiO_2 to measure the thickness profile shown in (g).

This is consistent with the growth mode of silver: the formation of islands in the deposition process of Ag is progressively "balanced" as the layer becomes thicker (see Appendix A for more

details). It can be noticed that the total thickness of the MHMAg/Al_2O_3 is not reported in Tab. 3.2 because, unfortunately, the solvent used to remove the marker line and create the measurable step also removed some of the upper layers making the measurement impossible. In Fig. 3.3 are reported the acquired AFM topographies of some of the samples and the thickness profile of the MHMAg/SiO_2. All samples, even the single Ag film display, tiny bumps due to the island growth of silver, which negatively impacts the uniformity of all layers. Despite these defects, since the overall roughness of all samples is at most a few nanometers and these bumps are uniformely distributed over all the surface, it is still reasonable to expect a uniform response of the samples over all their surface.

3.2.2 SEM images

The observations drawn from the analysis of AFM images are confirmed also by the Scanning Electron Microscopy (SEM) images acquired, some of which are reported in Fig. 3.4.

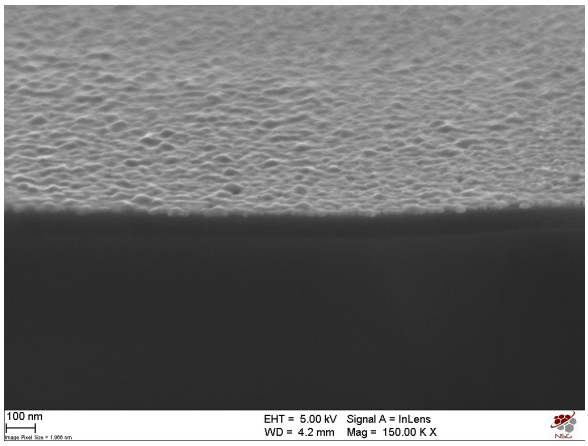

(a) BLAg/Al_2O_3

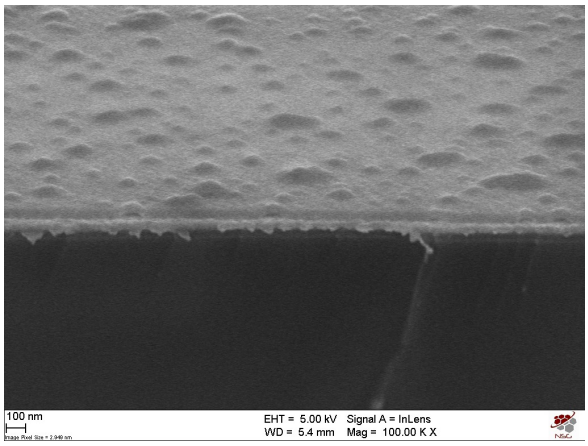

(b) SWAg/Al_2O_3

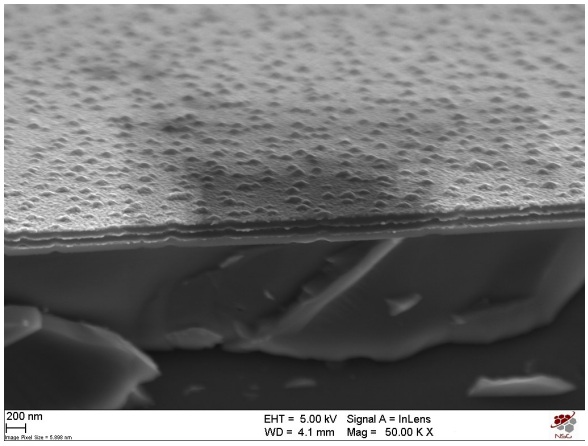

(c) MHMAg/Al_2O_3

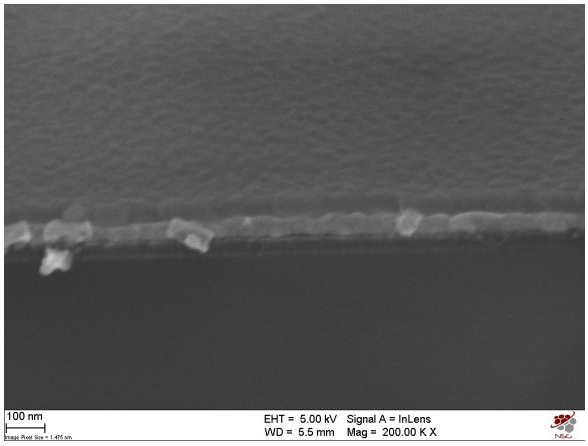

(d) SWAg/SiO_2

Figure 3.4: SEM images of the samples showing their morphology for an increasing number of layers (a,b,c) and for different constituent materials (b,d).

Although the individual layers are a little difficult to spot due to their small thicknesses and the not very precise cutting of the sample in cross-section, all images confirm that the main contribution to the surface roughness of the samples is bumpiness caused by the island growth of silver. Besides, as observed in AFM measurements, the images show a smaller overall roughness of the SWAg/Al_2O_3 compared to the BLAg/Al_2O_3 despite being thicker and with more layers. The images in Fig. 3.4(a) and (b) show how the greater thickness of Ag in the sandwich with respect to the bilayer partially reduces the average surface roughness, as the "empty" spots left during the initial 3D growth of silver are progressively filled, creating a not perfectly flat, but more uniform surface. Moreover, as seen in AFM measurements, the roughness of the SWAg/SiO_2 in Fig. 3.4(d) is smaller than the SWAg/Al_2O_3.

Additionally, in Fig. 3.5 are shown the cross section images of the multilayer hyperbolic metamaterials. Apart from the Ag/Al_2O_3 capping layer on top, which is too thin to be seen, all layers are present and the stratified four-period structure can be observed. The bottom SiO_2 layer of the MHMAg/SiO_2 cannot be seen due to the low contrast with the substrate. The island growth of Ag on Al_2O_3 causes the interfaces between the layers of the MHMAg/Al_2O_3, shown in (a), to be less sharp and defined than those in the MHMAg/SiO_2. Furthermore, by looking at Fig. 3.5(a), a glimpse of the interface between the first Al_2O_3 layer and the substrate can be caught. This first interface is well defined, proving that there are no issues in the growth of Al_2O_3 and that the cleaning and hydrophilisation of the substrates were carried out well. The particular morphology of the samples is only caused by the growth of Ag. In any case, all layers are sill quite defined and the periodicity is good. Consequently, with suitable corrections in the model, the analysis can still be carried out.

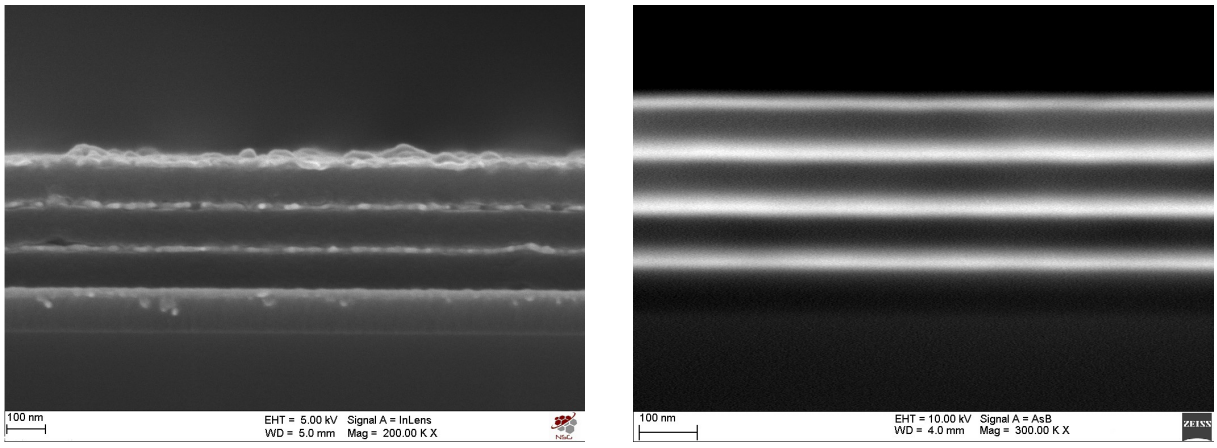

(a) (b)

Figure 3.5: Cross section SEM images of the MHM. The bright thinner layers correspond to Ag whereas the darker layers correspond to the dielectric layers: Al_2O_3 in (a) and SiO_2 in (b)

3.3 Linear optical properties

3.3.1 Dielectric functions

As stated in Section 2.2.3, ellipsometric measurements are also carried out on the samples to determine any possible deviation from the ideal model with the nominal thicknesses and tabulated dielectric functions. Besides, the optical properties of nanostructured materials such as those here considered, can indeed be quite different from the tabulated bulk ones. It is thus fundamental to determine the necessary corrections to carry out the rest of the analysis and simulate the response of the multilayers in the effective medium approximation (EMA).

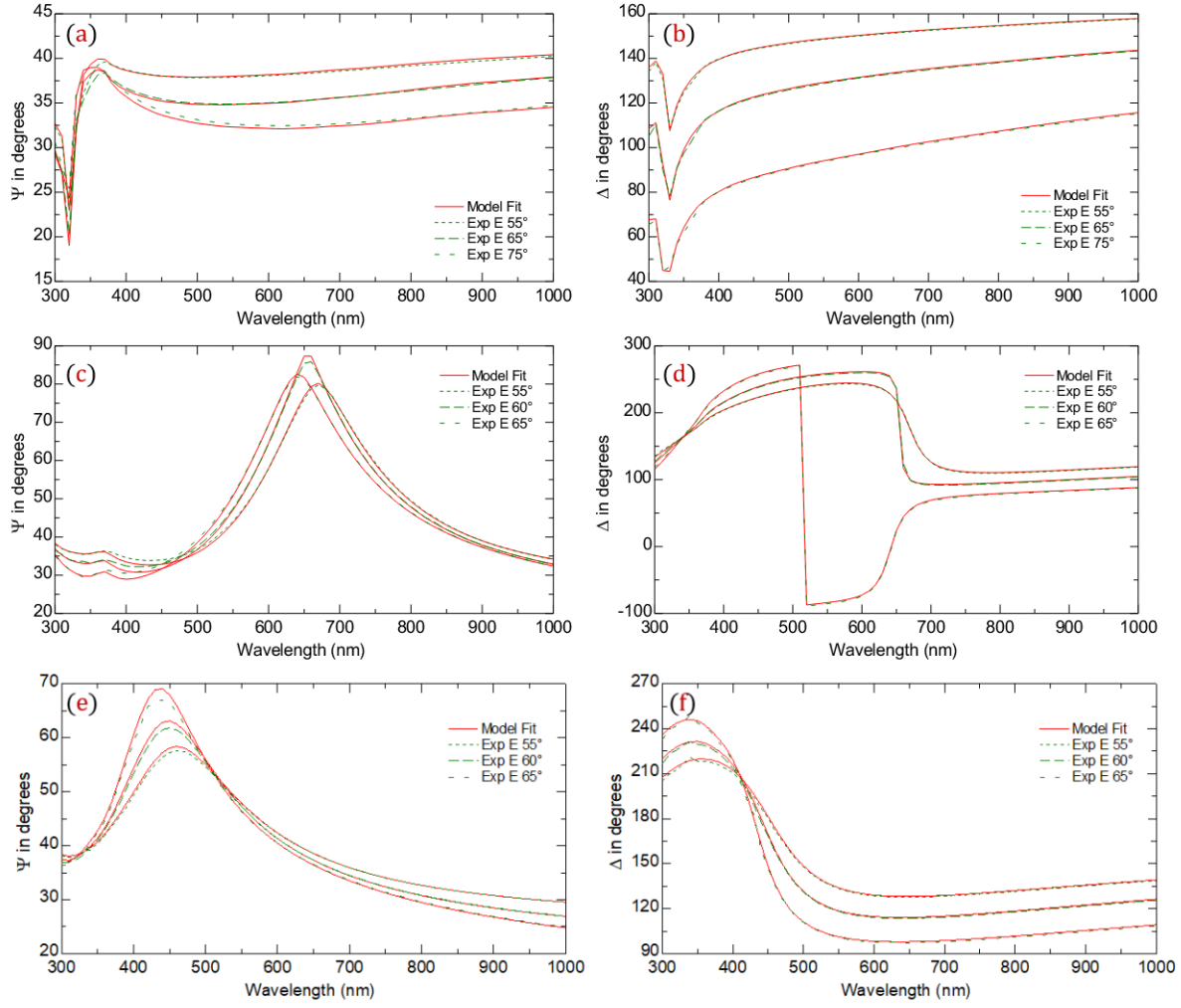

Figure 3.6: Ellipsometry measurements on: TFAg (a,b), $TFAl_2O_3$ (c,d), $TFSiO_2$ (e,f). The experimental and fitted ellipsometric parameters Ψ (amplitude ratios, left column) and Δ (phase shift, right column) in degrees are shown on the left and right respectively. Samples grown on Si were used for this analysis.

To begin with, the single-layer films are considered. The spectroscopic ellipsometry scans have been performed at incidence angles of 55°, 60° and 65°. In their analysis, the first attempt at fitting the experimental ellipsometric measurements is carried out by considering a simple

virtual model which considers the nominal values of the thicknesses and bulk values of the dielectric functions. Then, if discrepancies are found, the thickness or the dielectric functions are adjusted to reduce the mean squared error of the fit. The following results are found:

TFAg As starting values of the dielectric functions of silver, the bulk values found in [49] (*E. D. Palik*) are used. A good agreement is found immediately, and only a small correction on the nominal thickness is required. The fitted thickness is $t_{\mathrm{Ag}} = (17.0 \pm 0.9)$ nm which is also compatible with the AFM value $t_{\mathrm{Ag}}^{\mathrm{AFM}} = (17.4 \pm 0.9)$ nm.

TFAl_2O_3 The bulk dielectric functions of alumina in [50] (*T. Lichtenstein*) are used as starting values. The value found for the thickness $t_{\mathrm{Al_2O_3}} = (121 \pm 6)$ nm is compatible with both the nominal and AFM values but small adjustments are still required in the dielectric functions to improve the quality of the fit. For this reason the refractive index n of the deposited Al_2O_3 is better reproduced by considering a Cauchy function:

$$n(\lambda) = A + \frac{B}{\lambda^2} + \frac{C}{\lambda^4} \tag{3.1}$$

and letting A, B and C as fitting parameters. The experimental refractive index obtained with this procedure, which is smaller than the bulk value, leads to a better agreement between experimental and fitted data. The discrepancies are likely not caused by size effects but are more likely due to a different packing of Al_2O_3 atoms, which leads to a different material density. As a matter of fact, by using the n obtained from this fitting procedure it was also possible to obtain a good fit on ellipsometric measurements also on much smaller samples such as a reference 4 nm Al_2O_3 film.

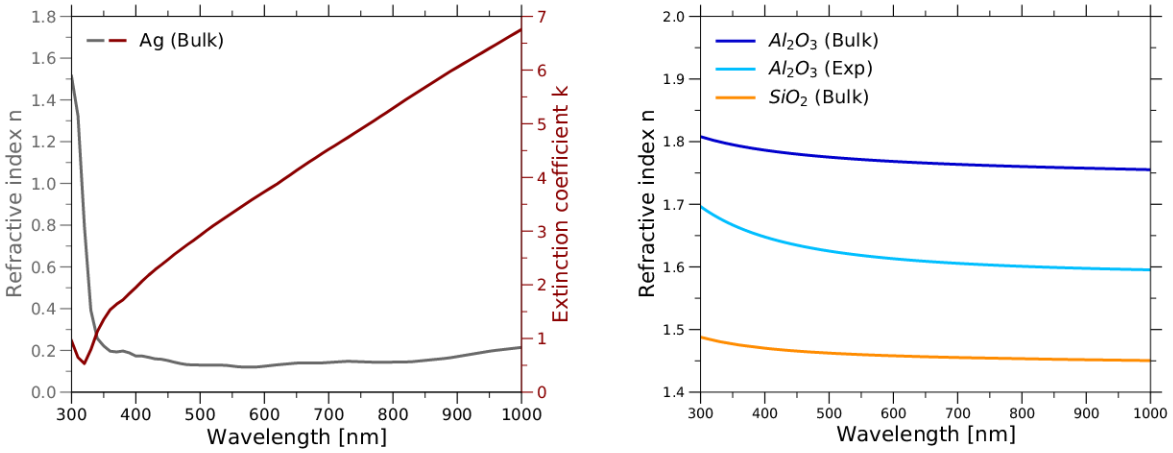

Figure 3.7: On the left the bulk refractive index and extinction coefficient of Ag from [49]. On the right, the bulk refractive indices of Al_2O_3 [50] and SiO_2 [49]. For Al_2O_3, the experimental n modeled as a Cauchy function is also reported (cyan curve). The extinction coefficient k is null for both SiO_2 and Al_2O_3.

TFSiO$_2$ The bulk dielectric functions of silica are also found in [49] and allow to obtain immediately a good fit of the experimental data. The value found for the thickness $t_{SiO_2} = (93 \pm 5)$ nm is compatible with both nominal and AFM values.

The ellipsometric measurements on these three reference single films are in Fig. 3.6. It can be seen that the final fit quality is very good at all considered wavelengths and the deviations from the nominal model are minimal. The dielectric functions used in this fitting procedure are shown in Fig. 3.7.

When repeating the same analysis on the multilayers, greater adjustments on the initial model are required due to the imperfections caused by the island growth of Ag on metal oxides which were already observed during AFM ans SEM characterization in Sections 3.2.1 and 3.2.2.

In this case, the starting model for the analysis is a superlattice made of a 16 nm Ag layer and a 85 nm dielectric one repeated for 4 periods and with a 4 nm Al_2O_3 capping layer on top. The optical functions initially set for these layers are those found during the analysis of the single films: the bulk values from [49] for Ag and SiO_2 and the experimental one for Al_2O_3. The experimental ellipsometry data collected on the two MHM are shown in Fig. 3.8 together with the curves simulated from the original ideal model (in blue) and the final fits obtained after the corrections on the thicknesses and dielectric functions (in red). It can be seen that the initial agreement between experimental and simulated data is quite poor.

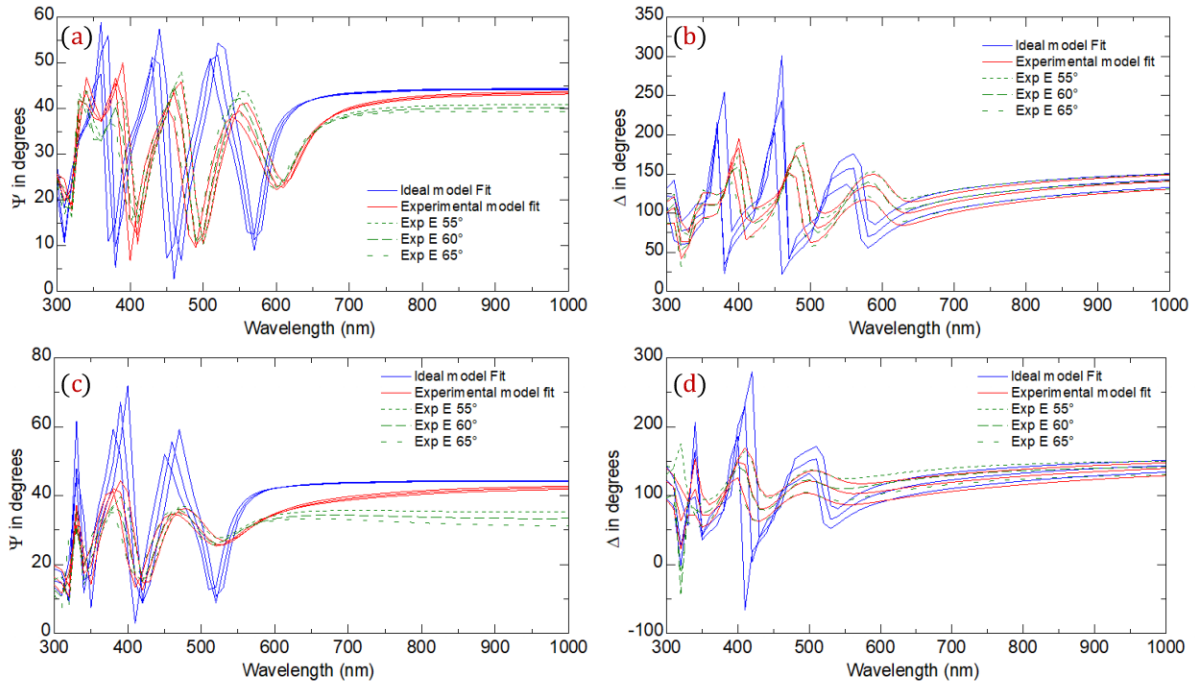

Figure 3.8: Ellipsometry measurements on the MHMAg/Al_2O_3 (a,b) and MHMAg/SiO_2 (c,d). The dotted green lines are the experimental data, the blue curves are simulated from the ideal model with nominal thicknesses, n and k. In red are the final fits obtained by adjusting the thicknesses and dielectric functions.

Usually, when discrepancies with the model are caused by small differences in the layer's thicknesses, a spectral shift between experimental and simulated data can be observed in the ellipsometric parameters Ψ and Δ. On the other hand, differences in the dielectric functions change the shape of the spectra. In light of this, the plots in Fig. 3.8 hint that for these samples, corrections on both the thickness and the dielectric functions are required to improve the agreement with the experimental ellipsomety data.

Firstly, the layer's thicknesses are set as fitting parameters. The capping layer is kept fixed at its nominal thickness since it is too thin to be accurately revealed by the ellipsometer. As a matter of fact, its presence does not influence the response of the system. As hinted by the blue-shift in the peaks of the simulated Ψ and Δ spectra with respect to the experimental ones, for the MHMAg/Al_2O_3 the values obtained are bigger than expected, as the fitted thicknesses of the layers are:

$$t_{Ag} = (17.1 \pm 0.9)\text{nm} \qquad t_{Al_2O_3} = (95 \pm 5)\text{nm}$$

for a total height of the system of $t_{MHMAgAl_2O_3} = (452 \pm 23)$ nm. This is partially due to the surface roughness caused by the 3D growth, which causes the effective thickness of the layers to be greater. On the other hand, for the MHMAg/SiO_2, only small corrections are required on the thicknesses as

$$t_{Ag} = (17.2 \pm 0.9)\text{nm} \qquad t_{SiO_2} = (83 \pm 4)\text{nm}$$

for a total height of the system of $t_{MHMAgSiO_2} = (405 \pm 20)$ nm. In this case, the values are all compatible with both nominal and AFM values. These corrections on the thicknesses, are still not enough as the agreement between experimental and simulated data is still not good. The cause of these differences, as expected, is an oxidation of the silver layers occurred during the synthesis of the multilayers. For reasons explained more in detail in Appendix A, during its growth on metal oxides like Al_2O_3 and SiO_2, Ag is likely to generate a thin layer of silver oxide mostly located at the interfaces between silver and the oxide, especially when working with highly kinetic synthesis techniques such as magnetron sputtering. Unfortunately, there is no way to know the exact stoichiometry and spatial distribution of this silver oxide Ag_xO_x in the Ag layers.

This problem can be solved by considering an *effective medium approximation layer* (EMA) in the the system's model in the analysis software of the ellipsometer. This special layer provides a method to mix together up to three sets of optical constants together by using the Bruggeman or Maxwell-Garnett EMA theories [51]. In practice this virtual layer allows to mix optical constants of different materials together in a reasonable way. It can be used to simulate interfacial intermixing, surface roughness, oxidized surface roughness or refractive index shifts [39]. Consequently, the best way to correct the dielectric function of the samples, is to use instead of Ag, in the virtual model of the multilayers, an EMA layer of silver oxide and pure silver, with the percentage of oxide let as free parameter to fit. In this way, it is possible to reproduce the transition from metallic to dielectric response as oxidation increases by considering a bigger percentage of oxidised silver.

To do this, the results found by *J. Qiu et al.* in this work [52] are used. In this experiment, the authors synthesised a series of Ag_xO_x thin films by the DC-magnetron reactive-sputtering under different oxygen to argon ratio conditions. More specifically, the Ar flux was fixed at 15 sccm (Standard Cubic Centimeters per Minute) whereas O flux ranged from 1 to 15 sccm. The optical properties of the synthesised films were then characterized by spectroscopic ellipsometry. By doing so, they found the dielectric functions n and k of silver films with increasing oxidation. The results of this analysis, together with the bulk values of n and k for pure Ag [49], are all reported in Fig. 3.9. At 15 sccm the saturated oxidation condition is already found and the authors found the dominating component to be Ag_2O. It can be seen that the evolution of the dielectric functions is continuous when going from Ag to Ag_2O.

Going back to the topic of the dielectric functions of the Ag in the multilayers studied in this work, since in them the oxidation is not too strong, in the fitting procedure the silver layers are replaced with an effective medium with bulk Ag [49] as first material, and Ag_xO_x synthesised with an oxygen flux of 1 sccm from [52]. The percentage of this last constituent is let as fitting parameter and results to be 14% for the MHMAg/Al_2O_3 and 35% for the MHMAg/SiO_2. For this reason, in the following sections, the partially oxidised layers in the MHMAg/Al_2O_3 will be indicated ad $Ag_xO_x^{EMA14}$ and those in the MHMAg/Al_2O_3 as $Ag_xO_x^{EMA35}$.

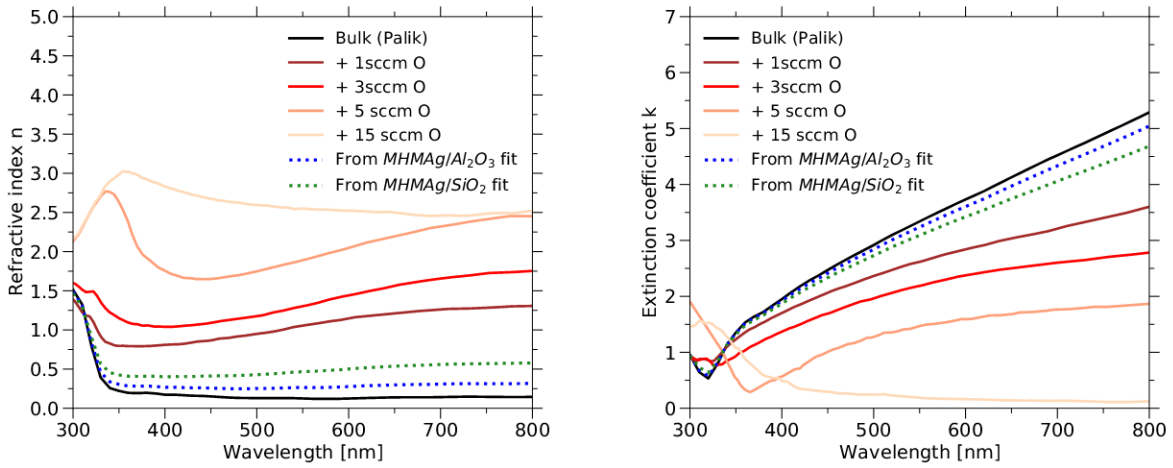

Figure 3.9: Refractive index n (on the left) and extinction coefficient k (on the right) of silver at increasing levels of oxidation. The continuous black lines correspond to the bulk values for pure Ag found in [49]. The other continuous curves correspond to Ag films synthesised by the DC-magnetron reactive-sputtering with flux of argon fixed at 15 sccm, and increasing fluxes of oxygen [52]. Finally, the dotted lines correspond to the experimental functions used to fit ellipsometric data of the MHMAgAl_2O_3 (blue) and MHMAgSiO_2 (green).

3.3.2 Simulations of the MHM in the EMA approximation

Now that the dielectric functions of the constituent materials are finally known, as explained in Section 1.1.1, if the size of the constituent elements of the metamaterial are much smaller than the wavelength of the interacting radiation it is possible to simulate the properties of the multilayer in an effective medium approximation (EMA). In this approximation, the optical

response of the material can be described in terms of the two permittivity components already defined in Eq. 1.18 and 1.21: the in-plane permittivity $\varepsilon_{\parallel}$ and the out-of-plane $\varepsilon_{\perp}$ one:

$$\varepsilon_{\parallel} = f_m \varepsilon_m + (1 - f_m)\varepsilon_d \tag{3.2}$$

$$\varepsilon_{\perp} = \frac{\varepsilon_m \varepsilon_d}{f_m \varepsilon_d + f_d \varepsilon_m} = \frac{\varepsilon_m \varepsilon_d}{f_m \varepsilon_d + (1 - f_m)\varepsilon_m} \tag{3.3}$$

where f_m is the metal filling fraction defined in Eq. 1.13 and ε_m, ε_d are the permittivities of the metal and the dielectric constituents of the multilayer. More specifically, for the MHMAg/Al_2O_3 ε_d is the dielectric function of alumina and ε_m is the one of the $Ag_xO_x^{EMA14}$ defined in the previous section. Conversly, for the MHMAg/AgO_2 ε_d is the dielectric function of silica and ε_m is the one of the $Ag_xO_x^{EMA35}$ also defined in the previous section. The real and imaginary parts of all these permittivities in the visible (VIS) and near-infrared (NIR) spectral range are shown in Fig. 3.10.

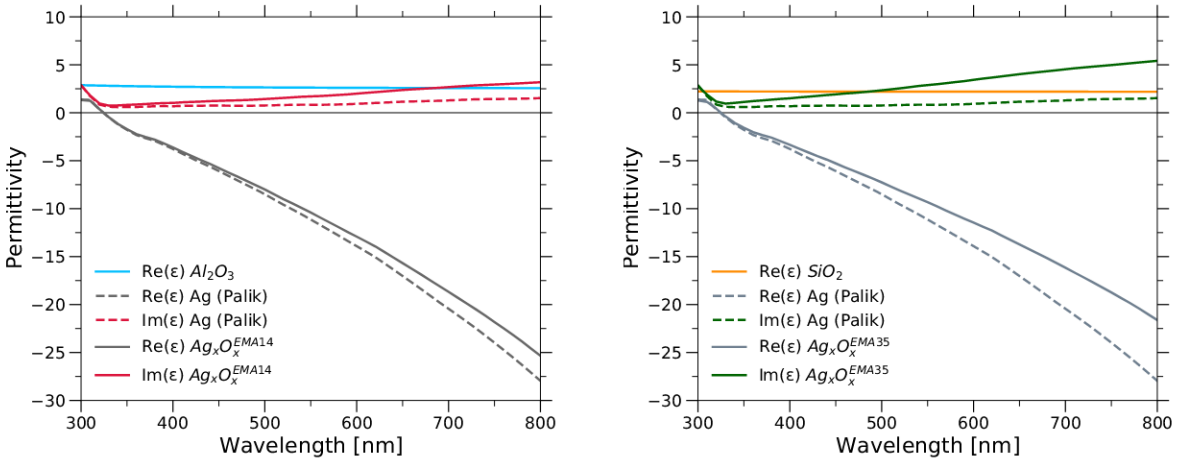

Figure 3.10: Permittivities of the constituent materials of the MHMAg/Al_2O_3 in (a) and the MHMAg/SiO_2 (b). The dashed lines in both plots correspond to the real $\mathfrak{Re}[\varepsilon]$ and imaginary $\mathfrak{Im}[\varepsilon]$ parts of the permittivity of bulk silver [49].

From the plots, it can be seen that both dielectrics have the characteristic Cauchy-type positive real permittivity displaying very little dispersion over the whole investigated spectral range. The imaginary parts are negligible as both Al_2O_3 and SiO_2 are transparent to visible light. The same cannot be said for silver, whose permittivity has a non-negligible and positive imaginary part and a real part which is negative over the whole visible range and shows the Drude-like dispersion typical of metals like Ag and Au (Eq. 3.4).

$$\varepsilon_m(\omega) = \mathfrak{Re}[\varepsilon_m] + i\mathfrak{Im}[\varepsilon_m] = \varepsilon_b - \frac{\omega_p^2}{\omega^2 + \gamma^2} + \frac{i\gamma\omega_p^2}{\omega^3 + \gamma^2\omega} \tag{3.4}$$

where $\varepsilon_m(\omega)$ is the metal permittivity expressed ad a function of the frequency ω, ε_b is a static term due to bound charge and γ is the damping coefficient. For Ag, $\mathfrak{Re}[\varepsilon_m]$ is small and negative in the near-ultraviolet part of the spectrum, becoming progressively more negative towards higher

wavelengths into the visible range. The two oxidised version of Ag present spectral trends very similar to pure silver but with more steeply increasing $\mathfrak{Re}[\varepsilon]$ and less negative $\mathfrak{Im}[\varepsilon]$. In fact, the effect of this oxidation is to make the metallic behaviour of the material less sharp. The differences from pure Ag are obviously greater for the more oxidised silver $Ag_xO_x^{EMA35}$. Using these permittivities as ε_d and ε_m in the effective medium theory, it is possible to determine the two effective in-plane and out-of plane permittivities and to calculare the spectral position at which the zero crossing point of $\mathfrak{Re}[\varepsilon_{\parallel}]$ is located: the epsilon near-zero wavelength λ_{ENZ}. In these calculations, one must consider that the metal filling fraction of the two metamaterials is also slightly different from the 16% value calculated with the original nominal thicknesses $t_m = 16\,\mathrm{nm}$ and $t_d = 85\,\mathrm{nm}$. After the corrections on the thicknesses found in the previous section:

MHMAg/Al_2O_3	$t_m \sim 17\,\mathrm{nm}$	$t_m \sim 95\,\mathrm{nm}$	$\Longrightarrow f_m = 15\%$
MHMAg/SiO_2	$t_m \sim 17\,\mathrm{nm}$	$t_m \sim 83\,\mathrm{nm}$	$\Longrightarrow f_m = 17\%$

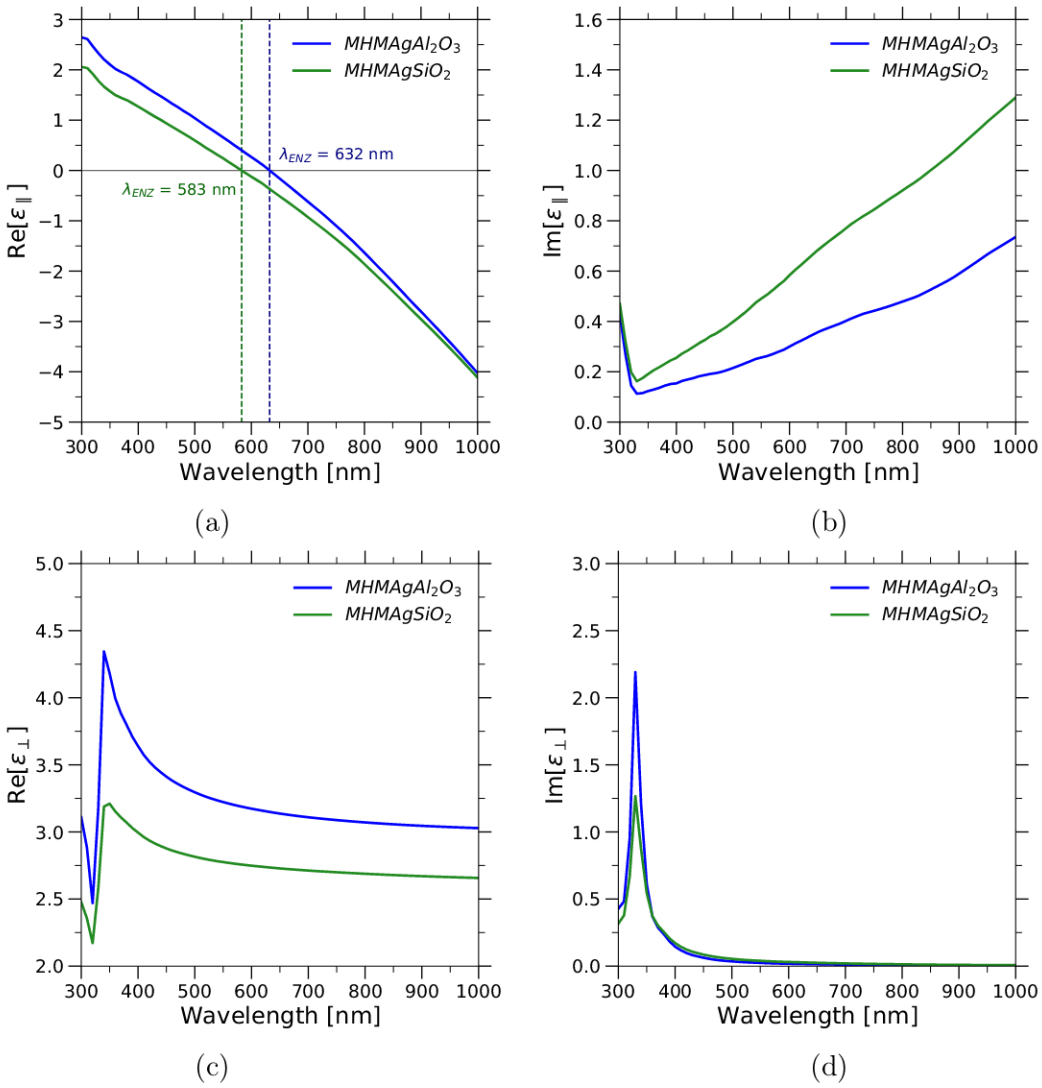

Figure 3.11: Real and imaginary parts of the in-plane (a,b respectively) and out-of plane (c,d) permittivities of the two MHM studied in this work. From graph (a) it is possible to determine the zero crossing point of $\mathfrak{Re}[\varepsilon_{\parallel}]$: the epsilon near-zero wavelength λ_{ENZ}.

Substituting Eq. 3.4 into Eqs. 3.2 and 3.3, it is easy to show that the real in-plane permittivity $\varepsilon_{\parallel}$ becomes null when

$$\mathfrak{Re}[\varepsilon_m] = -\frac{(1-f_m)\varepsilon_d}{f_m}$$

and will display metallic behavior for $\lambda > \lambda_{\mathrm{ENZ}}$. Besides, the out-of-plane permittivity $\varepsilon_{\perp}$ displays a resonance at a wavelength where

$$\mathfrak{Re}[\varepsilon_m] = -\frac{f_m\varepsilon_d}{1-f_m}$$

whose strength is limited by the damping constant γ of Eq. 3.4. For wavelengths above the ENZ point and sufficiently far away from this resonance, the composite material will exhibit type II hyperbolic dispersion [53]. All these features can be observed in the plots in Fig. 3.11 showing the real and imaginary parts of $\varepsilon_{\parallel}$ and $\varepsilon_{\perp}$ for both metamaterials. From graph (a) it can be seen that the epsilon near-zero wavelength of the two materials is at λ_{ENZ} =632 nm for the MHMAg/Al_2O_3 and λ_{ENZ} =583 nm for the MHMAg/SiO_2. Since $\varepsilon_{\perp}$ is always positive for both metamaterials, type I hyperbolic dispersion is never achieved with these samples.

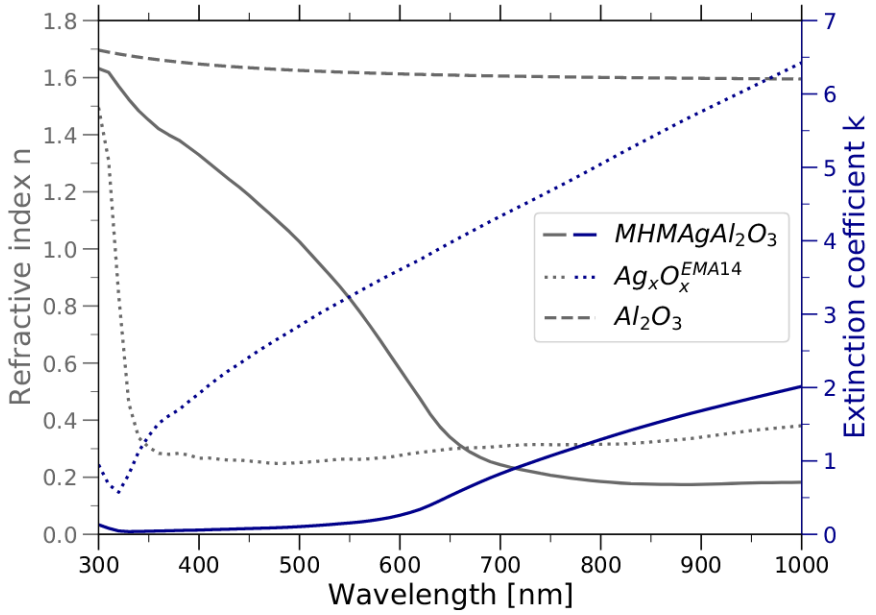

Figure 3.12: Refractive index n and extinction coefficient k of the MHMAg/Al_2O_3 (continuous lines) calculated in the effective medium approximation. The dielectric functions of $Ag_xO_x^{EMA14}$(dotted lines) and the refractive index of Al_2O_3 (dashed line) are also reported for comparison.

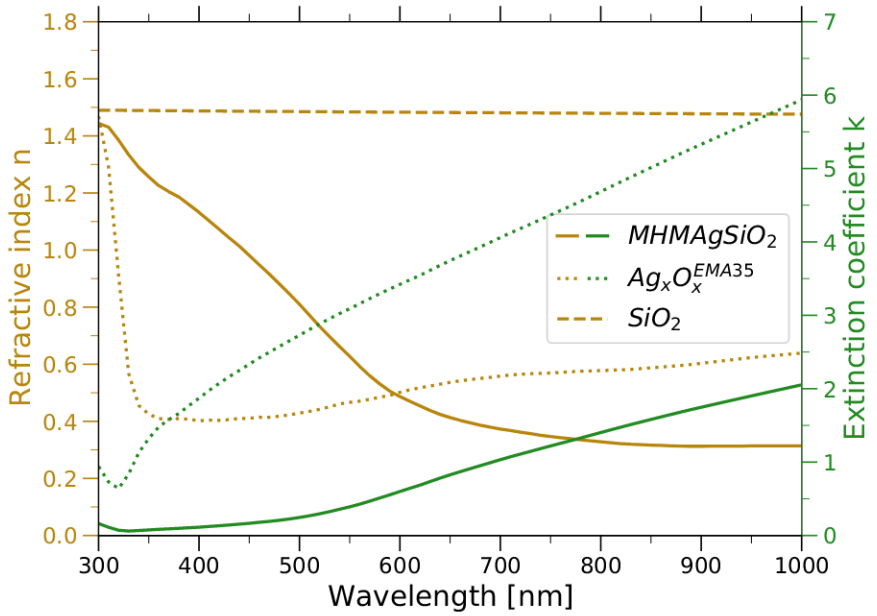

Figure 3.13: Refractive index n and extinction coefficient k of the MHMAg/SiO_3 (continuous lines) calculated in the effective medium approximation. The dielectric functions of $Ag_xO_x^{EMA35}$(dotted lines) and the refractive index of SiO_2 (dashed line) are also reported for comparison.

Now that the effective permittivities are known, it is also possible to calculate the effective linear refractive index n and extinction coefficient k of the two metamaterials. The results for MHMAg/Al_2O_3 are in Fig. 3.12 and those for MHMAg/SiO_3 are in Fig. 3.13. The trends in the two multilayers are very similar as expected given the fact that their structures are very similar. The small differences in f_m, ε_d ($n_{Al_2O_3} > n_{SiO_2}$) and degree of oxidation of the silver layers, manifest themselves in small changes in the absolute values of the effective dielectric functions n and k but are not enough to lead to completely different spectral trends in the linear optical responses.

3.3.3 Reflection, Transmission and Absorption spectra

As already anticipated in Section 2.2.3, the reflectance (R) and transmittance spectra (T) of the samples can also be collected with the ellipsometer for different polarization states and angles of incidence. This can be done by considering Fresnel equations for the multilayer, considered as a uniaxial semi-indefinite medium with optical axis normal to the surface. By doing so, the following expressions are found for reflectance [53]:

$$R_s = \left|\frac{\sin(\theta - \theta_{ts})}{\sin(\theta + \theta_{ts})}\right|^2 \qquad R_p = \left|\frac{\varepsilon_{\parallel}\tan\theta_{tp} - \tan\theta}{\varepsilon_{\parallel}\tan\theta_{tp} + \tan\theta}\right|^2 \tag{3.5}$$

where θ is the angle of incidence and

$$\theta_{ts} = \arcsin\left(\frac{\sin\theta}{\sqrt{\varepsilon_{\parallel}}}\right) \qquad \theta_{tp} = \arctan\left(\sqrt{\frac{\varepsilon_{\perp}\sin\theta^2}{\varepsilon_{\parallel}\varepsilon_{\perp} - \varepsilon_{\parallel}\sin\theta^2}}\right) \tag{3.6}$$

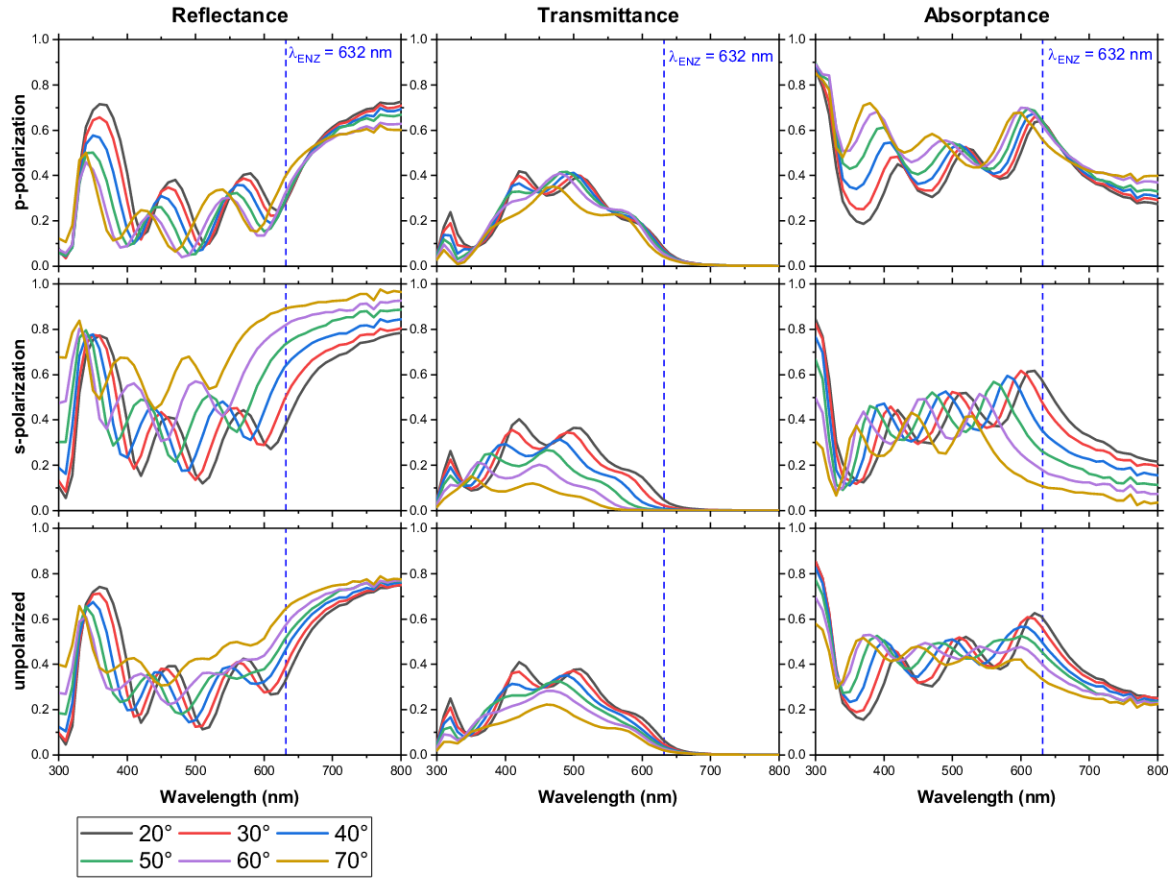

Figure 3.14: Reflectance (left column), transmittance (central column) and absorptance (right column) spectra of MHMAg/Al_2O_3 on SLG substrate for p-polarized (first row), s-polarized (second row) and unpolarized incident light (third row) at different angles of incidence. The blue dashed line marks the position of the λ_{ENZ} =632 nm.

The experimental R and T spectra, shown in Fig. 3.14 for MHMAg/Al_2O_3 and in Fig. 3.15 for MHMAg/SiO_2 are both collected on the same samples on SLG substrate in order to be able to easily calculate also the absorptance spectra (A), using the Lambert-Beer law $A = 1 - R - T$. These calculated spectra are also shown in Fig. 3.14 and 3.15. Measurements are carried out only at angles ranging from 20° to 70° at 10° steps, due to the limitations of the ellipsometer explained in Section 2.2.3, which make it impossible to obtain R spectra at normal incidence and T spectra at 90°. For both samples, it can be seen that the reflectance spectra present an abrupt change around the ENZ wavelength. More specifically, a sharp increase in R, followed by a constant trend for $\lambda > \lambda_{ENZ}$ can be observed. This is due to a growing metallic behaviour of the metamaterial in this spectral region [53]. For the same reason, the transmittance spectra rapidly go to zero for $\lambda > \lambda_{ENZ}$. On the contrary, at smaller wavelengths, reflectance spectra present an oscillating trend caused by interference effects between the waves propagating forward and backward between the metal layers of the sample [21]. These interference features are less sharp in the MHMAg/SiO_2 than in MHMAg/Al_2O_3 due to the greater level of oxidation which dulls the metallic features.

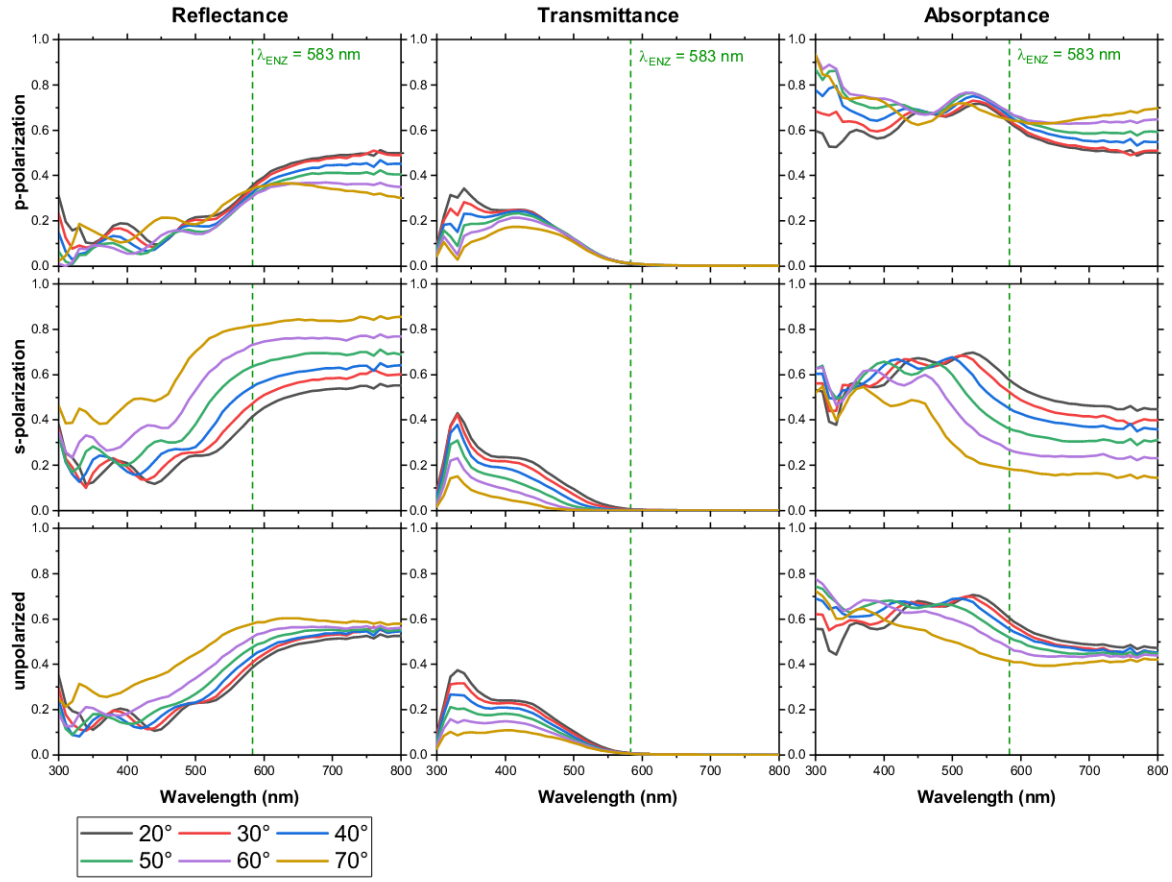

Figure 3.15: Reflectance (left column), transmittance (central column) and absorptance (right column) spectra of MHMAg/SiO_2 on SLG substrate for p-polarized (first row), s-polarized (second row) and unpolarized incident light (third row) at different angles of incidence. The green dashed line marks the position of the $\lambda_{ENZ} = 583\,nm$.

Besides, as explained in Appendix A, since oxidation mostly occurs at the interfaces, the latter are probably less defined, disrupting the interference phenomenon. These features are modified when changing the incidence angle or the polarization of the incoming light. For both samples, an increase and blueshift in reflectance at bigger angles of incidence is observed in all cases except with p-polarized light where R decreases and redshifts at increasing angles of incidence.

Regarding transmittance, for all polarization states the spectra decrease with increasing angles of incidence and their shape progressively loses the resonance peaks. These spectral trends of course influence the absorptance spectra, which also present resonant behaviours with different peaks that redshift and increase at increasing angles of incidence for p-polarization. For s-polarization and unpolarized light the opposite occurs. Of course, since at normal incidence all polarization states are degenerate, as the incidence angle tends to 0° the spectra become more and more similar at different polarizations. Another interesting feature of the absorptance spectra is that the last peak at normal incidence is in proximity of the λ_{ENZ}.

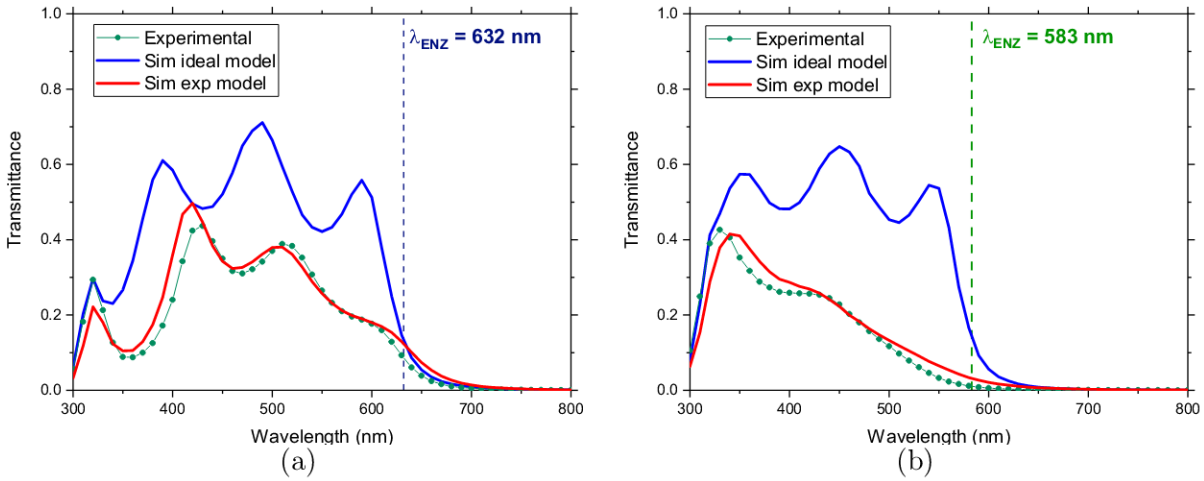

Figure 3.16: Transmittance spectra at normal incidence for (a) MHMAg/Al_2O_3 and (b) MHMAg/Al_2O_3. The blue curves are simulated from the ideal model with nominal thicknesses and pure silver. On the other hand, the red curves are simulated from the model with experimental thicknesses and oxidised silver. Finally, the green dotted curves show the experimental spectra.

Unfortunately, the analysis of transmittance spectra on the MHMAg/SiO_2 exposes a major problem in the possibility of performing z-scan measurements on the sample. Fig. 3.16 shows a comparison between the transmittance spectra at normal incidence of the two MHM simulated from the ideal model with nominal thicknesses and pure Ag (in blue), simulated from the model with experimental thicknesses and oxidised Ag (in red) and the experimental spectra (in green). If can be noticed that for MHMAg/SiO_2, the transmittance in the ENZ region is very low, less than 5% which makes it impossible to perform z-scan measures at reasonable incident intensities. It was thus not possible to carry out the characterization of the nonlinear optical properties of that sample in the spectral region of interest. To solve this problem, Ag/SiO_2 samples with different geometrical features ensuring that their ENZ range falls in a spectral region of sufficiently high transmittance can be engineered and are in progress. Another possibility to marginalize the problem would be to use a less kinetic synthesis technique with respect to magnetron sputtering in order to generate samples with less pronounced oxidation. For the moment, to check the entity of the nonlinear response of the MHMAg/SiO_2, z-scan measurements have been carried out at λ =500 nm, where the transmittance is still high enough.

Chapter 4

Study of the nonlinear optical response of the samples

In this chapter, the nonlinear optical response of the samples, measured through the z-scan technique, is finally quantified. The experimental results will then be compared with simulations generated from the model described in the last section of this chapter.

4.1 Nonlinear optical properties

Having completed the characterization of the linear optical properties of all samples, it is now possible to study optical nonlinearities by using the z-scan technique, as described in Section 2.2.4. The final objective is the determination of the nonlinear parameters n_2 and β in a wide spectral range around the ENZ wavelength, where enhancements of the nonlinear response have been predicted and were experimentally observed [9, 10, 15]. Unfortunately, in the present work, as already stated in the previous section, peroforming z-scan measurements on the synthesised MHMAg/SiO_2 near its ENZ wavelength is impossible due to the low transmittance of the sample in that range. This type of analysis is thus carried out only on the MHMAg/Al_2O_3 in the spectral range $\lambda \in [470, 680]$ nm. For the MHMAg/SiO_2 only a single measure at λ =500 nm is performed to check if nonlinear response is still observable.

Before doing so, an investigation of the nonlinear response of the single TFAg is carried out at λ =500 nm at increasing incident intensities on the sample. As a matter of fact, precise control over the incident intensity on the sample is not easy to achieve. For this reason, it is important to estimate a safe working range below which the nonlinear response is not detectable and above which there is a strong risk of damaging the sample. The same type of study is then repeated also on the MHMAg/Al_2O_3 at both λ =500 nm and at the ENZ wavelength λ =632 nm. Finally, single z-scan measurements are performed on the MHMAg/SiO_2 at λ =500 nm, where transmittance is still high enough to allow measurements.

4.1.1 Reference sample: TFAg

In Fig. 4.1 are reported two examples open aperture (OA) and closed aperture (CA) z-scan measurements performed at λ =500 nm on the single TFAg for different incident intensities: $I \sim 700\text{MW/cm}^2$ (upper graphs) and $I \sim 800\text{MW/cm}^2$ (lower graphs). It can be noticed how both OA scans present an upward peak in the focal position, characteristic of saturable absorption (SA). The increase in transmittance is more pronounced for more negative values of β. The CA signals on the other hand, present a strong asymmetry which is caused by the significant nonlinear absorption in the samples, dominating over nonlinear refraction. In spite of this the valley-peak configuration characteristic of self-focusing ($n_2 > 0$) can still be distinguished. The experimental points are then fitted with Eq. 2.2 as explained in Section 2.2.4 to evaluate the entity of the nonlinear parameters β and n_2 (red curves).

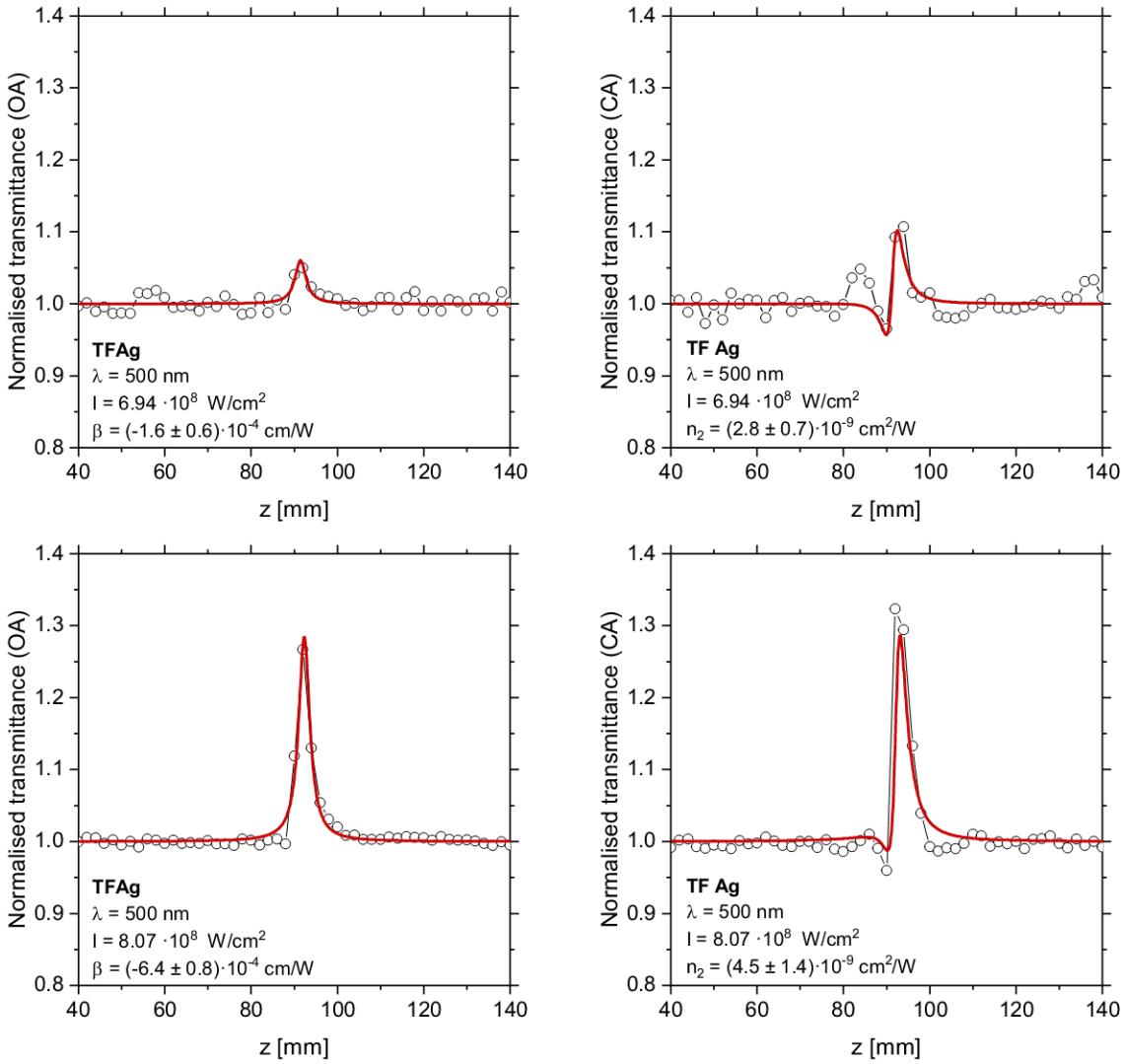

Figure 4.1: z-scans on the TFAg at λ = 500 nm at $I \sim 700\text{MW/cm}^2$ (upper graphs) and at $I \sim 800\text{MW/cm}^2$ (lower graphs). On the left are the open aperture curves (OA) and on the right the closed aperture ones (CA). The red solid curves are the best-fits obtained with the method described in Eq. 2.2.

The n_2 and β parameters obtained by fitting all z-scan curves collected at increasing intensities are shown in Fig. 4.2. The value of intensity on the x axis is the peak intensity incident on the sample, corrected to take into account the sample's reflectance. It can be seen that no nonlinear response is observed until intensities of 500 MW/cm^2. Above this range, increasingly strong saturable absorption ($\beta < 0$) and self-focusing ($n_2 > 0$) are observed. In the range $I \sim 500 \div 800$ MW/cm^2 the value of $n_2 > 0$ is $\sim 3 \cdot 10^{-9}$cm^2/W, compatible with the values reported in literature [15]. The risk of damaging the sample becomes non negligible beyond 1 GW/cm^2. The measurements are collected only at at λ =500 nm as in the spectral range of interest, given the almost constant absorptance of Ag, strong dependencies of the nonlinear response on the wavelength of the incident radiation are not expected. Moreover, this type of analysis is not carried out on the single dielectric thin films as little to none nonlinear response is obtained for both Al_2O_3 [54] and SiO_2 [15].

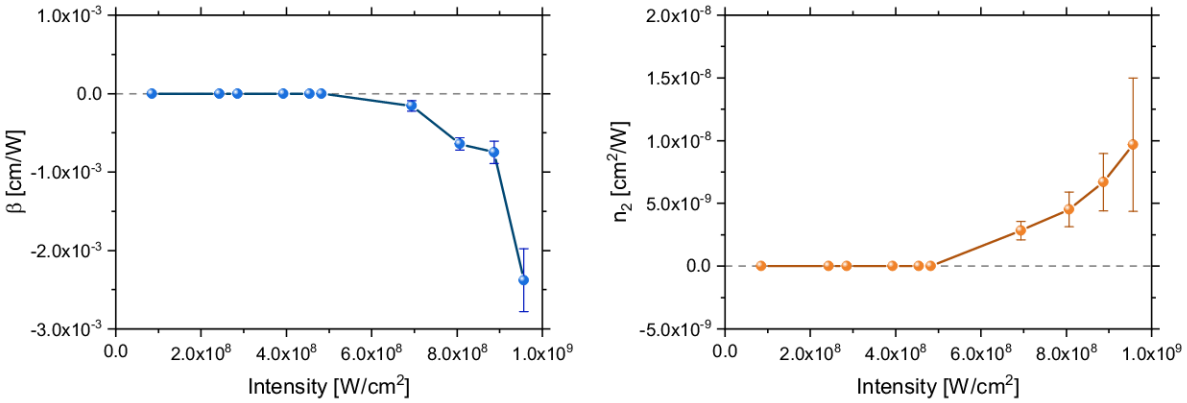

Figure 4.2: Nonlinear optical parameters β (on the left) and n_2 (on the right) of the TFAg at $\lambda = 500$nm as a function of the incident intensity.

4.1.2 Intensity dependent measurements: MHMAg/Al_2O_3

A similar analysis is repeated also on the MHMAg/Al_2O_3. In this case, given the absorptance (A) trends seen in Section 3.3.3, the procedure is repeated at two different wavelengths: $\lambda =$ 500nm, where A is lower, and at the expected ENZ $\lambda = 632$nm where there is a peak in A. The evolution of the parameters β and n_2 as a function of the intensity is shown in Fig. 4.3. It can be noticed that self-focusing is present at both wavelengths but while at $\lambda = 500$nm the sample displays reverse saturable absorption ($\beta > 0$), the opposite is true at $\lambda_{ENZ} = 632$nm where $\beta < 0$. Consequently, the nonlinear absorption behaviour of the MHMAg/Al_2O_3 at $\lambda = 500$nm is opposite to that of the single TFAg. Besides, it can be seen that in the MHM the nonlinear response is triggered at much smaller intensities than the single TFAg even <100 MW/cm^2. Moreover, the nonlinear response results stronger at these lower intensities. Furthermore, as expected, given the greater absorptance at $\lambda_{ENZ} = 632$nm the damage threshold is lower than at $\lambda = 500$nm where intensities of even 3.5 GW/cm^2 can be reached without damaging the multilayer. The same cannot be said at the ENZ, where more than 1.5 GW/cm^2 of incident intensity are enough to significantly increase the risk of damages.

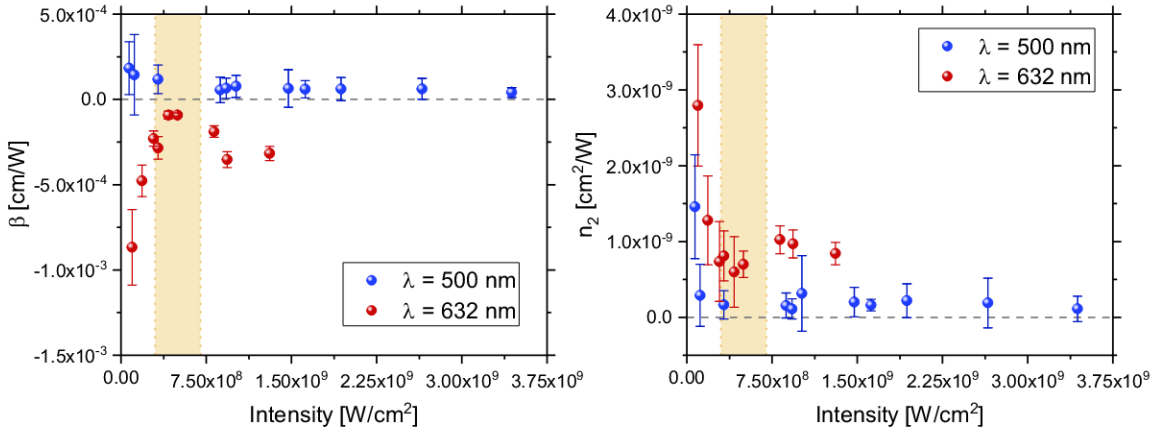

Figure 4.3: Nonlinear optical parameters β (on the left) and n_2 (on the right) of the MHMAg/Al_2O_3 as a function of the incident intensity. The blue points are collected at $\lambda = 500$nm whereas the red ones are taken at the ENZ wavelength of the multilayer: $\lambda = 632$nm. The yellow area highlights the range of intensities at which spectral measurements will be taken on the same sample.

In light of all these observations, the intensity range $I \in [300, 700]$ MW/cm^2, highlighted in yellow in Fig. 4.3, is chosen for performing the spectral nonlinear optical investigation. In Fig. 4.4 are the open aperture (OA) and closed aperture (CA) scans on the MHMAg/Al_2O_3 obtained at comparable intensities $\sim 300 \div 400$MW/cm^2 at a wavelength of $\lambda = 500$ nm and at λ_{ENZ} =632 nm. For comparison, the analogous curves collected at λ =500 nm and at a peak on the MHMAg/SiO_2 . Again, like for the TFAg, all CA signals are asymmetric due to the dominance of nonlinear absorption over nonlinear refraction. Both samples display self-focusing properties ($n_2 > 0$) and for MHMAg/Al_2O_3 this behaviour is observed at both considered wavelengths. Furthermore, the nonlinear response in both multilayers, is triggered at much lower intensities (even <100 MW/cm^2) with respect to the single TFAg, which displays no nonlinearities below ~500 MW/cm^2. Moreover, for the MHMAg/Al_2O_3, an enhancement of the nonlinear response of the MHMAg/Al_2O_3 is observed at the λ_{ENZ} =632 nm where, for an incident peak intensity of ~330 MW/cm^2, an increase in transmittance of about 20% due to saturable absorption is achieved, with a $\beta = (-2.8 \pm 0.7) \cdot 10^{-4}$cm/W. This is two times greater, in absolute value, than the $\beta = (1.2 \pm 0.8) \cdot 10^{-4}$cm/W value observed at λ =500 nm, where reverse saturable absorption causes a $\sim$ 10% decrease in transmittance. Likewise, at the ENZ $n_2 = (8.1 \pm 3.0) \cdot 10^{-10}$cm^2/W which more than 4-times greater than the one obtained at λ =500 nm, where $n_2 = (1.7 \pm 1.1) \cdot 10^{-10}$cm^2/W.

Regarding the MHMAg/SiO_2 it is interesting to see how a quite strong nonlinear response is still present in spite of the more pronounced oxidation of the Ag layer: an increase in transmittance of about 20% can be observed in the OA scan due to saturable absorption with $\beta = (-2.6 \pm 1.4) \cdot 10^{-4}$cm/W and $n_2 = (1.8 \pm 1.2) \cdot 10^{-9}$cm^2/W and were achieved at a peak intensity twice as high (~800 MW/cm^2 instead of ~370 MW/cm^2). The reason behind this lower threshold for the onset of optical nonlinearities in the MHMs compared to the single TFAg film has yet to be determined but it might be related to the resonant behaviour of the electric field in multilayer systems.

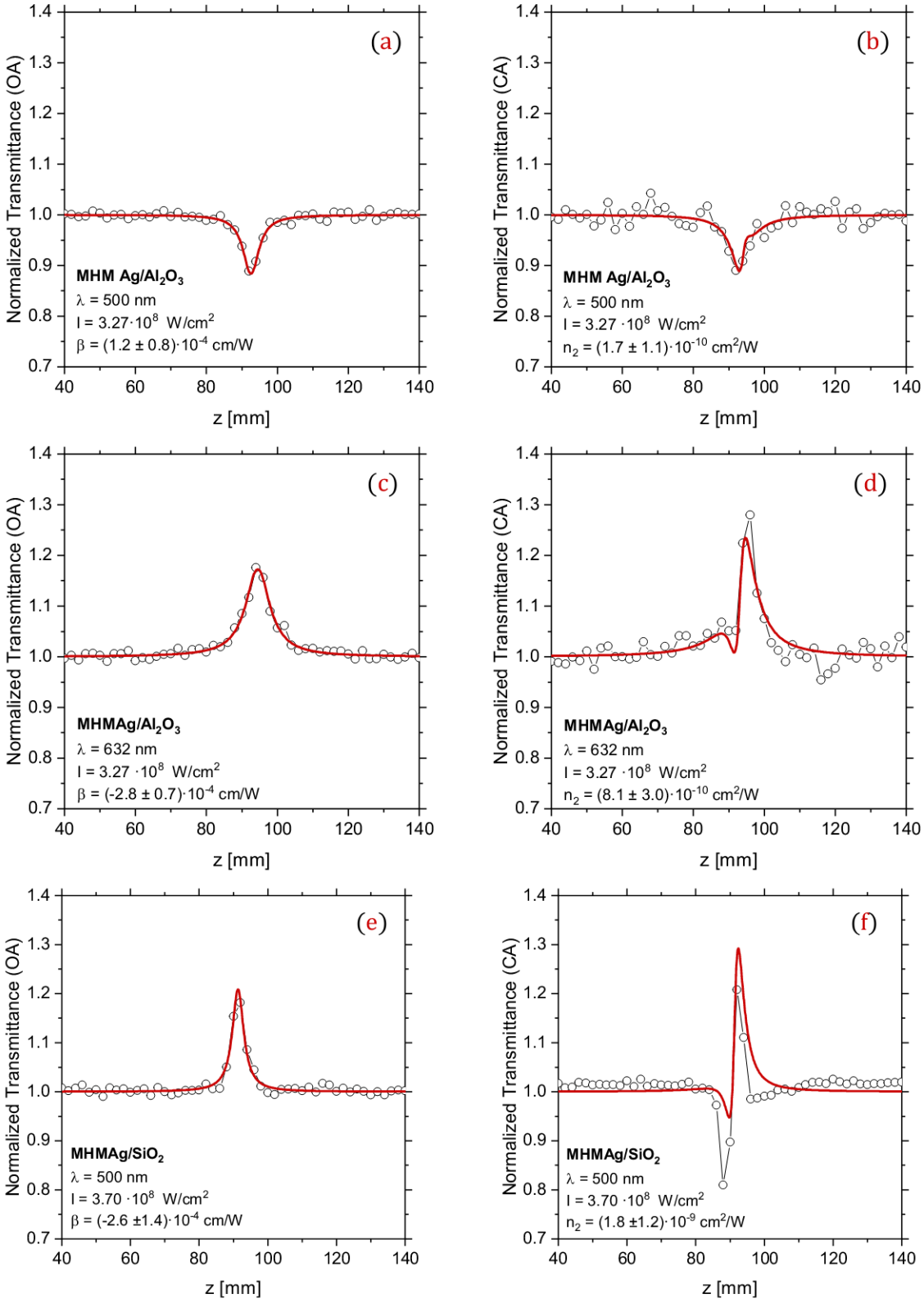

Figure 4.4: z-scans at $\lambda = 500$ nm (a, b) and at the ENZ wavelength $\lambda = 632$ nm (c,d) on the MHMAg/Al_2O_3. On the left are the open aperture curves (OA) and on the right the closed aperture ones (CA). In (e,f) are also the OA and CA scans obtained on the MHMAg/SiO_2 at $\lambda = 500$ nm. All scans are performed at peak intensities $I \sim 300 \div 400$ MW/cm^2. The red solid curves are the best-fits obtained with the method described in Eq. 2.2.

4.1.3 Spectral measurements: MHMAg/Al_2O_3

Now that a safe intensity range has been established, it is possible to investigate the spectral evolution of the nonlinear optical parameters β and n_2 of the MHMAg/Al_2O_3. The results of this characterization are shown in Fig. 4.5. The graphs show that both the type and entity of the nonlinear response are strongly dependent on the wavelength of the incident radiation. The nonlinear absorption parameter β presents an oscillating trend with two changes of sign: one at around 530 nm and another in proximity of the ENZ wavelength at about 600 nm. Beyond this second change of sign, the sample shows strong saturable absorption up to $\beta = (-7.4 \pm 1.3) \cdot 10^{-4}$cm/W at $\lambda \sim$660 nm. The nonlinear refractive index n_2 also presents an oscillating trend but remains always positive in the range considered. A first small peak can be noticed at $\lambda \sim$560 nm where $n_2 = (7.6 \pm 2.0) \cdot 10^{-10}$cm^2/W. The strongest response however, is measured at $\lambda \sim$650 nm, where $n_2 = (2.2 \pm 0.6) \cdot 10^{-9}$cm^2/W.

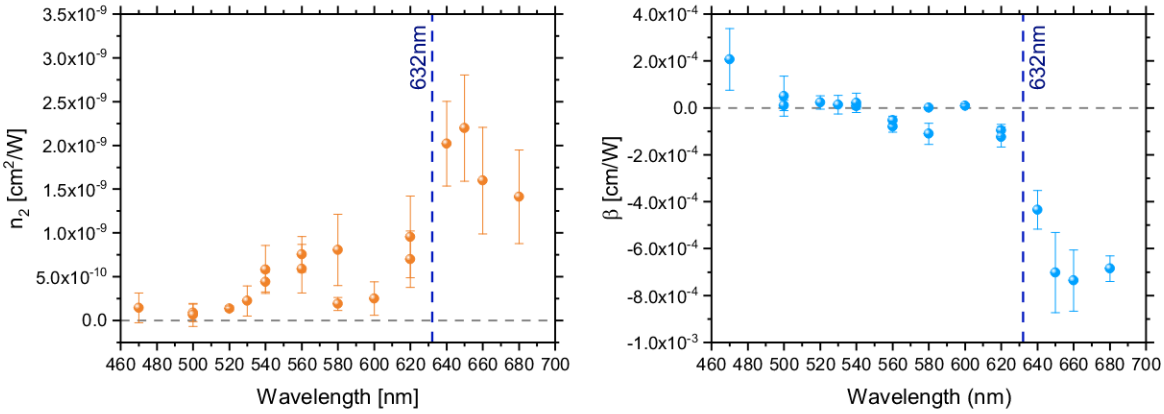

Figure 4.5: Spectral evolution of the nonlinear optical parameters n_2 (on the left) and β (on the right) of the MHMAg/Al_2O_3. The dashed blue line marks the ENZ wavelength λ =632 nm. The measurements were taken at intensities in the range chosen after the intensity measurements: $I \in [300, 700]$ MW/cm^2.

4.2 Simulation of the nonlinear optical response

As final step, the nonlinear optical response of the MHMAg/Al_2O_3 is simulated with the model proposed in [21]. This model allows to simulate the material's response not only at normal incidence but also for different incidence angles and polarization states.

To begin with, let's consider the complex nonlinear refractive index of the material, which can be written as [11, 15]:

$$\tilde{n}_2 = n_2 + i\frac{\lambda}{4\pi}\beta = \frac{3}{4c\varepsilon_0\tilde{n}_0 n_0}\chi^{(3)}_{\text{eff}} \tag{4.1}$$

where c is the speed of light in vacuum, ε_0 the vacuum permittivity, $\tilde{n}_0$ the complex linear refractive index of the material (whose real part is n_0) and $\chi^{(3)}_{\text{eff}}$ its effective third-order effective susceptibility (see eq. 1.34). The nonlinear refractive index n_2 and the nonlinear absorption

coefficient β are related to real and imaginary parts of the complex linear refractive index in Eq. 4.1 as in the following expressions:

$$n_2 = \mathfrak{Re}(\tilde{n}_2) \qquad \beta = \frac{4\pi}{\lambda}\mathfrak{Im}(\tilde{n}_2) \tag{4.2}$$

For multilayer metamaterials as the MHMAg/Al_2O_3, within an effective medium theory, the effective susceptibility $\chi^{(3)}_{\text{eff}}$ can be written as a weighted average on the filling fractions of those of the constituent materials. When doing so, since the third-order susceptibility of the dielectric component is ususally much smaller than that of the metal ($\chi^{(3)}_d \ll \chi^{(3)}_m$) it can be neglected, leading to the following expressions for the in-plane and out-of plane effective third-order susceptibility of the metamaterials:

$$\chi^{(3)}_{\parallel} = f_m\chi^{(3)}_m \qquad \chi^{(3)}_{\perp} = f_m\chi^{(3)}_m \left|\frac{\varepsilon_\perp}{\varepsilon_m}\right|^2 \left(\frac{\varepsilon_\perp}{\varepsilon_m}\right)^2 \tag{4.3}$$

where $\varepsilon_\perp$ is the out-of-plane complex effective dielectric permittivity of the metamaterials, given by Eq. 1.21, and ε_m is that of the metal. The first expression corresponds to the effective third-order susceptibility when the input electric field is parallel to the surface of the layers, the latter when it is perpendicular. Thus, for TE polarization, at all the angles of incidence it results:

$$\chi^{(3)}_{\text{TE}}(\theta) = \chi^{(3)}_{\parallel} \tag{4.4}$$

The expression for TM polarization is more complicated, as it depends on the angle of incidence and polarization state of the incident radiation. To determine this angular dependence $\chi^{(3)}_{\text{TM}}(\theta)$, one can start by considering the complex nonlinear effective permittivity for TM-polarized light given by the following expression (obtained in analogy to Eq. 1.23):

$$\varepsilon^{\text{NL}}_{\text{TM}}(\theta) = \frac{\varepsilon^{\text{NL}}_{parallel}\varepsilon^{\text{NL}}_{\perp}}{\varepsilon^{\text{NL}}_{\parallel} sin^2(\theta) + \varepsilon^{\text{NL}}_{\perp} cos^2(\theta)} \tag{4.5}$$

where the in-plane ($\varepsilon^{\text{NL}}_{\parallel}$) and out-of-plane ($\varepsilon^{\text{NL}}_{\perp}$) nonlinear complex effective permittivities are [11]:

$$\varepsilon^{\text{NL}}_{\parallel} = \varepsilon_{\parallel} + \frac{3}{4}\chi^{(3)}_{\parallel}|E|^2 \qquad \varepsilon^{\text{NL}}_{\perp} = \varepsilon_{\perp} + \frac{3}{4}\chi^{(3)}_{\perp}|E|^2 \tag{4.6}$$

Replacing Eqs. 4.6 in Eq. 4.5, and assuming that the nonlinear terms in the denominator of Eq. 4.5 are negligible with respect to the linear terms, one finally gets:

$$\varepsilon^{\text{NL}}_{\text{TM}}(\theta) \approx \varepsilon_{\text{TM}}(\theta) + \frac{3}{4}\varepsilon_{\text{TM}}(\theta)\left(\frac{\chi^{(3)}_{\parallel}}{\varepsilon_{\parallel}} + \frac{\chi^{(3)}_{\perp}}{\varepsilon_{\perp}}\right)|E|^2 \tag{4.7}$$

where the terms of order of $|E|^4$ have been neglected. From Eq. 4.7 one can finally obtain:

$$\chi^{(3)}_{\text{TM}}(\theta) = \varepsilon_{\text{TM}}(\theta)\left(\frac{\chi^{(3)}_{\parallel}}{\varepsilon_{\parallel}} + \frac{\chi^{(3)}_{\perp}}{\varepsilon_{\perp}}\right) \tag{4.8}$$

Going back to Eq. 4.3, it can be noticed that both $\chi^{(3)}_{\parallel}$ and $\chi^{(3)}_{\perp}$ depend on the product $f_m\chi^{(3)}_m$. Since in the measuring process a broad wavelength range has been explored, for more

accurate results the third-order susceptibility of the metal (in this case, silver) should be characterized over the whole spectral range considered. However, since the nonlinear response of silver is almost constant in the explored range [15], for the sake of simplicity a single z-scan measurement is performed at a reference wavelength of λ =500 nm. The complex nonlinear refractive index of silver is then determined from Eq. 4.2, from which, by inverting Eq. 4.1, the Ag third-order susceptibility $\chi^{(3)}_{\mathrm{Ag}}$ at λ =500 nm can be calculated. Moreover, the hypothesis that the contribution due to the nonlinearity of the dielectric component can be neglected in the calculations is validated by the fact that no nonlinear response is measured on single Al_2O_3 films [54]. As the reference sample for silver, the BLAg/Al_2O_3 is used instead of the single Ag film to have a reference silver layer with properties as close as possible to those in the actual multilayer (namely with oxidation and increased surface roughness caused by the island growth). In the case of the bilayer, the dielectric function of the material, which allows to achieve the best fits of ellipsometric measurements, is an EMA silver layer similar to those of the MHMAg/Al_2O_3 but with percentage of Ag_xO_x of 7%. This smaller percentage, compared to that of the silver in the MHMAg/Al_2O_3, is consistent with the fact that, as explained in Appendix A, the oxidation occurs mostly at the metal-alumina interface and in the case of the BL only one interface is present. The results of the z-scan measurement, performed at a peak intensity of $I = 1.2 \cdot 10^9 \mathrm{W/cm^2}$ are shown in Fig. 4.6.

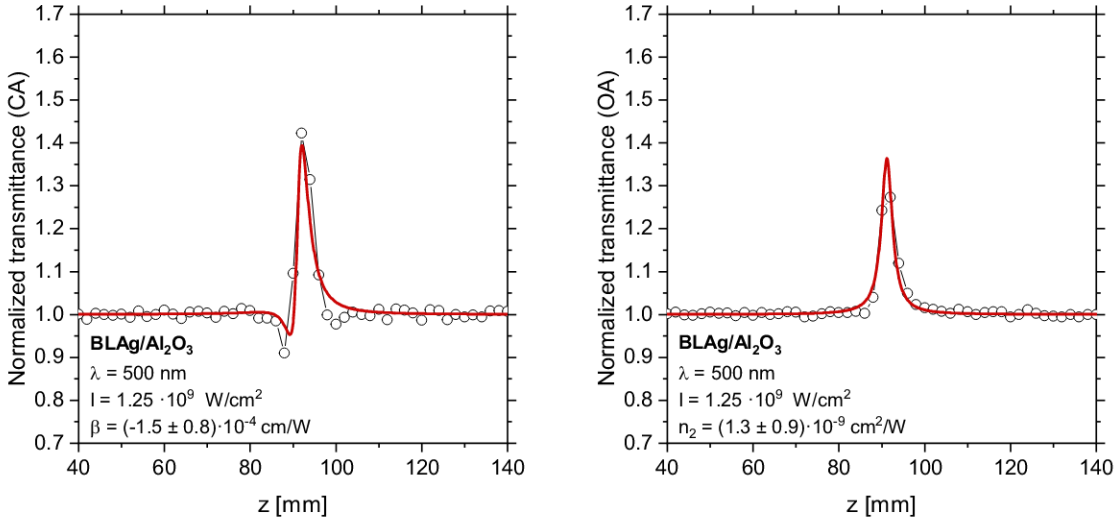

Figure 4.6: z-scans at λ = 500 nm on the BLAg/Al_2O_3. On the left is the open aperture curve (OA) and on the right the closed aperture one (CA). The red curves are obtained with the fitting procedure described in Sec. 2.2.4.

To provide a complete description of the nonlinear response of the MHM, the resonant behavior of the electric field distribution in the multilayers caused by interference effects in the waves propagating forward and backward between the metal layers has to be considered. This effect accounts for a local intensity enhancement in the metallic layers. Owing to this, a wavelength-dependent effective metal filling fraction can be defined as:

$$\rho(\lambda, \theta) = f_m \frac{\zeta_{\mathrm{MM}}(\lambda, \theta)}{\zeta_{\mathrm{film}}(\lambda, \theta)} \tag{4.9}$$

where ζ_{MM} represents the spatial average of the square of the electric field over the metallic layers of the metamaterials while ζ_{film} is calculated for a silver thin film of 17 nm. The profile of the electric field in the MHMs at $\lambda = 500$nm is reported in Fig. 4.7. These calculations are done starting from the electric fields simulated by EMUstack [55].

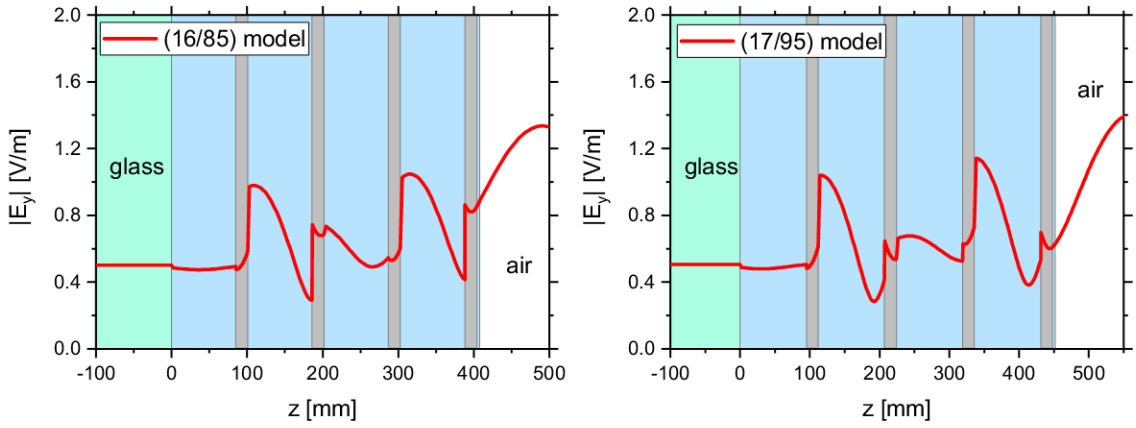

Figure 4.7: Electric field profile (E_y component) inside the MHMAg/Al_2O_3(16/85) (left) and MHMAg/Al_2O_3(17/95) (right), simulated by EMUstack at $\lambda = 500$ nm. A sketch of the multilayer structure used for the simulations is also superimposed to the curves. The beam is impinging normally to the samples from the air side, with an amplitude of 1 V/m. In the incidence half-space (air), E_y contains both the input beam and the reflected one.

Two simulations are carried out: one using the nominal values of the thicknesses (t_{Ag} =16 nm and $t_{Al_2O_3}$ =85 nm) and the other considering the experimental model ($t_{Ag_xO_x}{}^{EMA14}$ =17 nm and $t_{Al_2O_3}$ =95 nm). The results are shown in Fig. 4.8 together with the experimental data previously collected.

An excellent agreement is found between the experimental values of the nonlinear refractive index n_2 and the simulated ones. Both simulation predicts an enhancement of n_2 near the ENZ wavelength, in agreement with experimental data. The position of these features however, is slightly redshifted in the simulation performed using experimental thicknesses with respect to that obtained with nominal ones. Because of this, the simulation obtained with the experimental values is more compatible, within the margin of error, with the values of n_2 estimated from the z-scan measurements, especially near the ENZ region. This validates even further the fact that the experimental model derived from ellipsometric characterization provides a better representation of the system.

Regarding the nonlinear absorption coefficient β, a very nice agreement is found in the blue side of the spectrum and the general spectral trend of the data, together with the change of sign in proximity of the ENZ wavelength, is correctly predicted. The compatibility of the experimental data with the simulated models in absolute value is however slightly worse for $\lambda > \lambda_{ENZ}$. These discrepancies are probably caused by the fact that in the simulations a uniform response of the reference sample BLAg/Al_2O_3 was assumed over the whole investigated wavelength range as it is

the case for a single Ag thin film. The spectral response of the bilayer, however, might be more complicated. Besides, more accurate predictions are expected to be achieved by considering a reference sample with two metal-dielectric interfaces (namely a $Al_2O_3/Ag/Al_2O_3$ sandwich with thicknesses of 85/16/85nm respectively) as this is the case of the silver films in the multilayer. Another thing worth mentioning is that the peak of n_2 is slightly to the right of the estimated λ_{ENZ} =632 nm in both the experimental and simulated data. This is probably due to the effect of the oxidation which slightly reduces the metal filling fraction f_m and slightly redshifts the position of the ENZ compared to the value estimated with the effective medium theory.

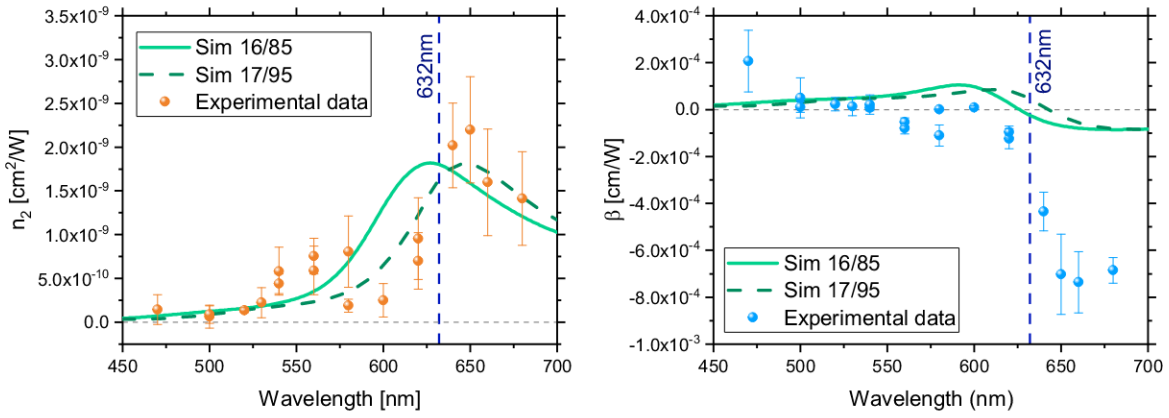

Figure 4.8: Comparison of the experimental values of the nonlinear optical parameters n_2 (on the left) and β (on the right) of the MHMAg/Al_2O_3 with the simulations. The simulation marked by the continuous line is performed by considering the model with nominal thicknesses (t_{Ag} =16 nm and $t_{Al_2O_3}$ =85 nm). The green dashed curve is instead simulated considering the experimental model ($t_{Ag_xO_x}^{EMA14}$ =17 nm and $t_{Al_2O_3}$ =95 nm). The measurements were taken at intensities in the range chosen after the intensity measurements $I \in [300, 700]$ MW/cm^2. The dashed blue line marks the ENZ wavelength λ =632 nm

In conclusion, the fabricated sample MHMAg/Al_2O_3 presents enhanced nonlinearities near the ENZ wavelength λ_{ENZ} =632 nm as expected. Moreover, the nonlinear parameters, present a peculiar spectral dependence which is not found in pure silver, with opposite nonlinear absorption behaviour at certain wavelengths. Furthermore, the nonlinear response of the multilayer is triggered at smaller incident peak intensities. Also, the other constituent material of the multilayer, namely Al_2O_3, does not display any nonlinearities [54]. All these facts show how different the properties of the artificially engineered metamaterial can be with respect to those of the original constituent materials.

Regarding the simulations, it can be said that the model proposed in [21], provides a very good description of the nonlinear optical response of the sample. As a matter of fact, the trend, the sign and, to a certain extent, even the magnitude of the nonlinear parameters n_2 and β can be predicted with good accuracy, in spite of the simple assumptions in the model, especially regarding the reference sample. More accurate predictions are expected to be achieved by considering, as a reference sample, a $Al_2O_3/Ag/Al_2O_3$ sandwich and by determining its nonlinear

parameters over the whole investigated spectral range. The model described in this section can thus represent a useful tool to design multilayer metamaterials with tailored nonlinear optical properties even predicting the response at different incidence angles and polarization states.

Conclusions

In this work, two different type II multilayer hyperbolic metamaterials (MHMs) have been studied to characterize and quantify their nonlinear optical response. More specifically, third order Kerr-type optical nonlinearities, namely nonlinear refraction and nonlinear absorption of the samples, have been studied.

The MHMs were modelled in the effective medium approximation (EMA) which allows to define an effective permittivity of the system as a function of the angle of incidence and polarization state of the incident radiation.

The study of the nonlinear optical response was focused in a special spectral region of vanishing permittivity called epsilon near-zero (ENZ) region, where the real part of the effective in-plane permittivity is zero ($\mathfrak{Re}(\varepsilon_{\parallel}) = 0$) and where enhancements of the nonlinear response have been predicted and observed [9, 10, 15, 21].

Two types of samples were synthesised, both of which had metal filling fraction $f_m = 16\%$ as they were made up of four repeated silver-dielectric bilayers with nominal thicknesses of 16 nm for the Ag layer and 85 nm for the dielectric one. As dielectric, alumina (Al_2O_3) was used in the first set of samples called MHMAg/Al_2O_3 and silica (SiO_2) in the other one called MHMAg/SiO_2.

The samples were synthesised through magnetron sputtering depositions and their morphology was then characterized by both Atomic Force Microscopy (AFM) and Scanning Electron Microscopy (SEM). Through AFM measurements, the deposited thicknesses and the surface roughnesses could be estimated and by SEM the uniformity of the layers could be visually evaluated. At this step, a surface roughness of $\sim 2 \div 3$ nm was observed on both MHMs due to the characteristic 3D island growth of Ag on metal oxides such as Al_2O_3 and SiO_2. Despite these defects, the uniformity and smoothness of the samples was still enough to justify the application of the EMA, albeit with some corrections on the thicknesses and dielectric functions of the constituent layers. As a matter of fact, the growth process is also characterized by partial oxidation of Ag especially at the metal-dielectric interfaces [56].

To determine the linear optical response of the samples and find the required adjustments in the dielectric functions and thicknesses of the layers, the MHMs were studied with spectroscopic ellipsometry. Thanks to these measurements, the dielectric function of the partially oxidised Ag layers could be reconstructed and it was found that oxidation was more pronounced in the MHMAg/SiO_2.

By using these experimental dielectric functions and thicknesses, a more accurate model in the EMA of the two MHMs could be constructed, leading to an estimated λ_{ENZ} =632 nm for the

MHMAg/Al_2O_3 and λ_{ENZ} =583 nm for the MHMAg/SiO_2.

Reflectivity and transmittance measurements were also carried out with the ellipsometer for different angles of incidence and polarization states. The absorptance spectra were then reconstructed by applying Lambert-Beer's law. All spectra displayed an abrupt change of trend for $\lambda > \lambda_{ENZ}$ caused by the transition to an effective metallic behaviour in that spectral range. Due to the oxidation of silver, experimental transmittance spectra were found to be different from those simulated with the ideal model. Particularly, in the MHMAg/SiO_2, experimental transmittance was found to be too low in the ENZ region making it impossible to evaluate the nonlinear response of this sample in this spectral range with the z-scan technique as it requires the mesurement of the transmitted signal. New Ag/SiO_2 samples with different geometrical features ensuring that their ENZ range falls in a spectral region of sufficiently high transmittance can be engineered and are in progress. For this work, only z-scan measurements at a reference wavelength of λ =500 nm were carried out on this sample.

After this preliminary characterization process, the nonlinear optical response of the samples could finally be quantified with the z-scan technique [41]. By fitting the experimental z-scan curves with the procedure described in Sec. 2.2.4 [45, 26] it is possible to determine the nonlinear absorption parameter β and the nonlinear refraction coefficient n_2.

A first set of measurements was performed on a single 16 nm thin film of silver (TFAg) at λ =500 nm and for increasing values of the peak incident intensity. No nonlinear response was observed for intensities $\lesssim 500\,\mathrm{MW/cm^2}$. On the contrary, when this characterization of the nonlinear properties as a function of the incident peak intensity was repeated on the MHMAg/Al_2O_3, a strong nonlinear response was observed also at peak intensities $\lesssim 100\,\mathrm{MW/cm^2}$ for both wavelengths at which these measuments were carried out, namely $\lambda = 500$ nm and $\lambda_{ENZ} = 632$ nm. The reason for this lower threshold for the onset of optical nonlinearities in the multilayers has yet to be determined but it might be related to the resonant behaviour of the electric field in multilayer systems. These intensity-dependent measurements on the MHMAg/Al_2O_3 allowed also to determine a safe intensity-working-range for the spectral characterization of the parameters β and n_2, $I \in [300, 700]\mathrm{MW/cm^2}$, where the risk of damaging the samples is very low and scans with a good signal-to-noise ratio can be obtained.

In the spectral characterization of n_2 and β, an enhancement of the nonlinear response in the MHMAg/Al_2O_3 was observed near its ENZ wavelength $\lambda_{ENZ} = 632$ nm. Moreover, the spectral evolution of the nonlinear parameters β and n_2 was found to be quite different to that of pure silver. For example, saturable absorption (SA) was observed in the MHMAg/Al_2O_3 at λ = 500 nm, where the single TFAg displayed reverse saturable absorption (RSA). Furthermore, the nonlinear response of the multilayer was triggered at smaller incident peak intensities. All these facts testify how artificially engineered metamaterials allow to obtain nonlinear optical properties that can be very different from those of the original constituent materials. To predict the sign and entity of these nonlinearities, the model proposed in Sec. 4.2 [21] has proven to be a useful and reliable tool to make predictions on the expected values of the nonlinear parameters β and n_2. As a matter of fact, in spite of the introduction of some simplifications in the model, especially regarding the reference sample, the trend, the sign and, to a certain extent, even the magnitude

of n_2 and β were predicted with good accuracy. More accurate predictions will be obtained by considering a $Al_2O_3/Ag/Al_2O_3$ sandwich as reference sample and by fully characterizing its nonlinear response over the whole considered spectral range.

Finally, it is worth mentioning that, although in this work the nonlinear response of the samples was studied only at normal incidence for the sake of simplicity, the nonlinear optical properties of these type of MHMs is known to be strongly dependent also on the polarization state and angle of incidence of the input electromagnetic field. The simulation model can be a useful tool in this process, as it makes it possible to design multilayer metamaterials with tailored nonlinear optical properties also for different incidence angles and polarization states, with possible applications in the design of metamaterials with tailored nonlinear optical properties which can be externally controlled, for example, by simply changing the angle of incidence.

Appendix A

Thin film epitaxy: Ag growth on metal oxides

"Epitaxy" is the growth of a thin crystalline film on a crystalline substrate where the orientation is determined by the underlying crystal. The process results in the formation of crystalline thin films that may be of the same chemical composition and structure as the substrate (*homoepitaxy*) or may be composed of one or more layers of different materials (*heteroepitaxy*). This deposited film is denoted as epitaxial film or epitaxial layer. In this process, three different growth modes can be observed depending on the values assumed by the three macroscopic surface tensions: γ_o, γ_i and γ_s which are the free energy per unit area at the overlayer/vacuum interface, at the overlayer/substrate interface, and the substrate/vacuum interface, respectively. The three modes, schematically depicted in Fig. A.1, are: [57]

(i) The *Frank-Van der Merwe* mode occurs when

$$\gamma_s \geq \gamma_o + \gamma_i \tag{A.1}$$

In this case, the growth of the overlayer reduces the free energy of the system, leading to complete wetting of the surface and to smooth, 2D, layer-by-layer growth. The epitaxial orientation is typically established within the first monolayer.

(ii) The *Volmer-Weber* mode, on the other hand, occurs when $\gamma_s < \gamma_o + \gamma_i$. In this case the substrate surface tends to maximize its exposed area, leading to layer clustering on the substrate in a 3D island growth. Further deposition causes these islands to grow and maybe coarsen but they may sometimes rearrange extensively before forming a continuous film. Epitaxial orientation is typically established quite late in the growth process.

(iii) The *Stranski-Krasantov* mode is initiated as a 2D growth until, after a critical thickness, further deposition is in the form of islands. In his case the interfacial energy γ_i increases throughout the growth process due to strain in the growing layer, caused by mismatch in lattice constants between the substrate and the deposited layer. In such a case, the thermodynamic conditions for 2D growth terminate after a certain thickness and further 2D growth of is in competition with that of more stable islands.

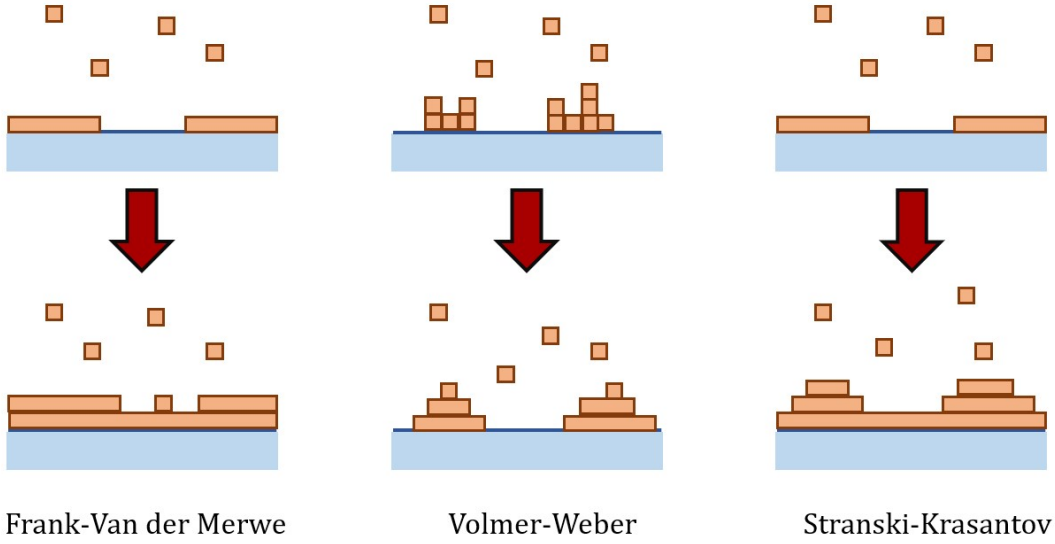

Figure A.1: Schematic diagram of the three possible growth modes for an epitaxial film. Image adapded from [58].

The condition for Frank-Van der Merwe growth obviously holds for the trivial case of homoepitaxy when the layer is grown under conditions close to thermodynamic equilibrium. In the heteroepitaxial case however, to have layer-by-layer growth, usually one must have $\gamma_o \ll \gamma_s$ to satisfy Eq. A.1 since γ_i is usually positive and non-negligible [59].

This condition is not usually verified for the growth of Ag on Al_2O_3. As a matter of fact, Ag has a surface free energy of $1.3\,J/m^2$ [60, 61] whereas the surface free energy of Al_2O_3 is approximately $0.69\,J/m^2$, thus smaller than that of Ag [62]. Due to the weak interaction between Ag and alumina [63], γ_i is estimated to be very small. Consequently, to minimize the surface free energy, the exposed Al_2O_3 surface area will be maximized and, Ag should grow three-dimensionally on alumina. Moreover, given the probability of adsorption of silver on alumina is very small [64]. This leads to high mobility of Ag adatoms on Al_2O_3 and high desorption probability. Consequently, the main growth mechanism of silver film is through the adsorption of adatoms on already existing Ag clusters. For these reasons, the uniformity and superficial smoothness of films are low until few tens of nm have been deposited. Many experimental results proved that this is indeed the case.

For example *K. Luo et al.* [63] observed three-dimensional (3D) growth of Ag clusters when studying the growth of Ag on an ordered Al_2O_3 surface. The cluster size increased with Ag coverage as shown by the 3D scanning tunneling microscopy (STM) images in Fig. A.2. In these studies since, as already observed, Ag is not necessarily grown on alumina as a layer-by-layer mode, instead of identifying the various steps of growth in terms of layer thickness, it is preferred to use monolayer equivalent (MLE) as a unit of the amount of deposited Ag. For Ag(111) $1\text{MLE} = 1.4 \cdot 10^{15}\text{atoms/cm}^2$ whereas Ag(100) and $1\text{MLE} = 1.2 \cdot 10^{15}\text{atoms/cm}^2$ [56].

The images in Fig. A.2, show the growth of 0.05, 0.5, 1.0, and 2.0 MLE Ag on Al_2O_3 at 300 K. It can be seen that, at relatively small coverages (0.05 MLE), very small clusters of Ag already start forming.

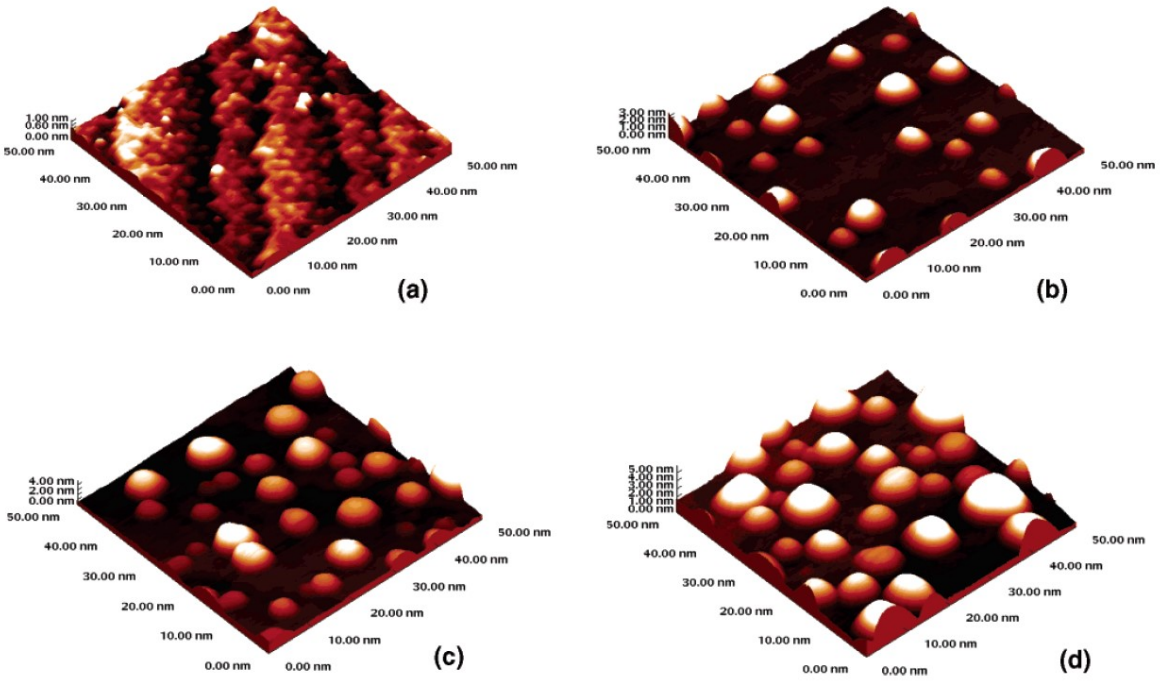

Figure A.2: STM images Ag on Al_2O_3 at different steps of growth at 300 K: (a) 0.05 ML; (b) 0.5 ML; (c) 1.0 ML; and (d) 2.0 ML. Image from [63].

These clusters range from 1 to 3.5 nm in diameter, 0.4−1.2 nm in height and hemispherical in shape. Thereafter, their size increases with increasing Ag coverage. At 0.5 ML, the clusters are 4-8 nm in diameter, with heights of 1.0-3.0 nm. At 2.0 MLE, the Ag clusters reach 4.5−10 nm in diameter, with heights of 1.7−5.0 nm.

Another important aspect in the growth of Ag on Al_2O_3 is that at the first adsorption steps, the minimum binding energy condition is favored at O sites. In light of this, it is very likely for Ag atoms to bind to the exposed O atoms of alumina forming Ag-O bonds, and therefore losing their metallic behavior in the very first atomic layers. Besides, the surface free energies of Ag oxide are 0.28 J/m^2 for AgO, [65] and 0.65 J/m^2 for Ag_2O [62] which are all lower than that of both Ag and Al_2O_3. Therefore, 2D Ag oxide growth mode is expected and thermodynamically favorable as the interaction between Ag clusters and alumina is weak, differing from that of Ag oxides on alumina [56].

Similar mechanisms are observed in the growth of Ag on SiO_2. As a matter of fact, the surface free energy of SiO_2 is also smaller than that of Ag as it is approximately 0.61 J/m^2 [62], leading to 3D island growth of silver also on silica. Besides, since oxygen desorption is more likely to occur in SiO_2 rather than Al_2O_3 the oxidation of silver during deposition on SiO_2 is expected to be even greater than in Al_2O_3. This is especially true when working with synthesis techniques such as magnetron sputtering. Indeed, given the highly kinetic nature of in-coming sputtered particles, the thermal stability of silicon oxide might be significantly altered and when deposited with proper substrate heating, an oxide layer may easily desorb from the surface and diffuse through the Ag layer being deposited [66].

Regarding the samples synthesised and studied in this work however, the surface roughness

of Ag/SiO_2 samples was significantly smaller than that of Ag/Al_2O_3. The reason behind this difference lies probably in the greater degree of oxidation of the silver layers in the SiO_2-based multilayer (35%) compared to the Al_2O_3-based one (14%). As a matter of fact, as previously observed, the surface free energies of silver oxides are much smaller than those of pure silver, making 2D growth more likely when oxidation is more pronounced.

Bibliography

[1] V. G. Veselago. Electrodynamics of substances with simultaneously negative electrical and magnetic permeabilities. *Soviet Physics Uspekhi*, 10(4):504–509, 1968.

[2] W. Cai, U. K. Chettiar, A. V. Kildishev, and V. M. Shalaev. Optical cloaking with metamaterials. *Nature Photonics*, 1(4):224–227, 2007.

[3] J. B. Pendry. Negative refraction makes a perfect lens. *Physical Review Letters*, 85(18):3966, 2000.

[4] O. Reshef, I. De Leon, M. Z. Alam, and R. W. Boyd. Nonlinear optical effects in epsilon-near-zero media. *Nature Reviews Materials*, 4(8):535–551, 2019.

[5] A. Poddubny, I. Iorsh, P. Belov, and Y. Kivshar. Hyperbolic metamaterials. *Nature Photonics*, 7(12):948–957, 2013.

[6] P. Shekhar, J. Atkinson, and Z. Jacob. Hyperbolic metamaterials: fundamentals and applications. *Nano Convergence*, 1(1):1–17, 2014.

[7] L. Ferrari, C. Wu, D. Lepage, X. Zhang, and Z. Liu. Hyperbolic metamaterials and their applications. *Progress in Quantum Electronics*, 40:1–40, 2015.

[8] C.L. Cortes, W. Newman, S. Molesky, and Z. Jacob. Quantum nanophotonics using hyperbolic metamaterials. *Journal of Optics*, 14(6):063001, 2012.

[9] A.D. Neira, N. Olivier, M. E. Nasir, W. Dickson, G. A Wurtz, and A. V. Zayats. Eliminating material constraints for nonlinearity with plasmonic metamaterials. *Nature Communications*, 6(1):1–8, 2015.

[10] M. Z. Alam, I. De Leon, and R. W. Boyd. Large optical nonlinearity of indium tin oxide in its epsilon-near-zero region. *Science*, 352(6287):795–797, 2016.

[11] R. W. Boyd. *Nonlinear optics, Fourth edition.* Academic press, 2020.

[12] R. Maas, J. Parsons, N. Engheta, and A. Polman. Experimental realization of an epsilon-near-zero metamaterial at visible wavelengths. *Nature Photonics*, 7(11):907–912, 2013.

[13] D. Lu, J. J. Kan, E. E. Fullerton, and Z. Liu. Enhancing spontaneous emission rates of molecules using nanopatterned multilayer hyperbolic metamaterials. *Nature Nanotechnology*, 9(1):48–53, 2014.

[14] K. V. Sreekanth, Y. Alapan, M. ElKabbash, E. Ilker, M. Hinczewski, U. A. Gurkan, A. De Luca, and G. Strangi. Extreme sensitivity biosensing platform based on hyperbolic metamaterials. *Nature Materials*, 15(6):621–627, 2016.

[15] S. Suresh, O. Reshef, M. Z. Alam, J. Upham, M. Karimi, and R. W. Boyd. Enhanced nonlinear optical responses of layered epsilon-near-zero metamaterials at visible frequencies. *ACS Photonics*, 8(1):125–129, 2020.

[16] G. A. Wurtz, R. Pollard, W. Hendren, GP W., D.J. Gosztola, V.A. Podolskiy, and A. V. Zayats. Designed ultrafast optical nonlinearity in a plasmonic nanorod metamaterial enhanced by nonlocality. *Nature Nanotechnology*, 6(2):107–111, 2011.

[17] R. Chandrasekar, Z. Wang, X. Meng, S. I Azzam, M. Y. Shalaginov, A. Lagutchev, Y. L. Kim, A. Wei, A. V. Kildishev, A. Boltasseva, et al. Lasing action with gold nanorod hyperbolic metamaterials. *ACS Photonics*, 4(3):674–680, 2017.

[18] Z. Guo, H. Jiang, and H. Chen. Hyperbolic metamaterials: From dispersion manipulation to applications. *Journal of Applied Physics*, 127(7):071101, 2020.

[19] Z. Jacob, I. I Smolyaninov, and E. E. Narimanov. Broadband purcell effect: Radiative decay engineering with metamaterials. *Applied Physics Letters*, 100(18):181105, 2012.

[20] M.A. Noginov, H. Li, Y. A. Barnakov, D. Dryden, G. Nataraj, G. Zhu, C.E. Bonner, M. Mayy, Z. Jacob, and E.E. Narimanov. Controlling spontaneous emission with metamaterials. *Optics Letters*, 35(11):1863–1865, 2010.

[21] D. Genchi, I. G. Balasa, T. Cesca, and G. Mattei. Tunable third-order nonlinear optical response in epsilon-near-zero multilayer metamaterials. 2021. Phys. Rev. Appl. Submitted.

[22] N. Kinsey, C. DeVault, J. Kim, M. Ferrera, V.M. Shalaev, and A. Boltasseva. Epsilon-near-zero al-doped zno for ultrafast switching at telecom wavelengths. *Optica*, 2(7):616–622, 2015.

[23] A.V. Krasavin, P. Ginzburg, and A. V. Zayats. Free-electron optical nonlinearities in plasmonic nanostructures: a review of the hydrodynamic description. *Laser & Photonics Reviews*, 12(1):1700082, 2018.

[24] W. S. Martins, H. L.D. de S. Cavalcante, T. P. de Silans, M. Oriá, and M. Chevrollier. Two-beam nonlinear Kerr effect to stabilize laser frequency with sub-doppler resolution. *Applied Optics*, 51(21):5080–5084, 2012.

[25] L. W. Tutt and T. F. Boggess. A review of optical limiting mechanisms and devices using organics, fullerenes, semiconductors and other materials. *Progress in Quantum Electronics*, 17(4):299–338, 1993.

[26] T. Cesca, P. Calvelli, G. Battaglin, P. Mazzoldi, and G. Mattei. Local-field enhancement effect on the nonlinear optical response of gold-silver nanoplanets. *Optics Express*, 20(4):4537, 2012.

[27] S Swann. Magnetron sputtering. *Physics in Technology*, 19(2):67–75, 1988.

[28] D. M. Mattox. *Handbook of Physical Vapor Deposition (PVD) Processing*. Elsevier, 2010.

[29] M. Braun. Magnetron sputtering technique. *Handbook of Manufacturing Engineering Technology; Springer: Berlin, Germany*, pages 2929–2957, 2015.

[30] https://www.adnano-tek.com/magnetron-sputtering- deposition-msd.html.

[31] G. Binnig, C. F. Quate, and C. Gerber. Atomic force microscope. *Phys. Rev. Lett.*, 56:930–933, Mar 1986.

[32] P. Eaton and P. West. *Atomic force microscopy*. Oxford university press, 2010.

[33] D. Rugar and P. Hansma. Atomic force microscopy. *Physics Today*, 43(10):23–30, 1990.

[34] C.F. Quate. The afm as a tool for surface imaging. *Surface Science*, 299:980–995, 1994.

[35] D. Nečas and P. Klapetek. Gwyddion: an open-source software for spm data analysis. *Open Physics*, 10(1):181–188, 2012.

[36] https://www.zeiss.com/microscopy/int/products/scanning-electron-microscopes/sigma.html.

[37] Joseph I. Goldstein et al. *Scanning Electron Microscopy and X-Ray Microanalysis*. Springer, 4th edition, 2017.

[38] H. Fujiwara. *Spectroscopic ellipsometry: principles and applications*. John Wiley & Sons, 2007.

[39] *Guide to using WVASE, Spectroscopic Ellipsometry Data Acquisition and Analysis Software*. J.A. Woollam Co., Inc., 2008.

[40] M. Sheik-bahae, A. A. Said, and E. W. Van Stryland. High-sensitivity, single-beam n_2 measurements. *Optics Letters*, 14(17):955, 1989.

[41] M. Sheik-Bahae, A.A. Said, T.-H. Wei, D.J. Hagan, and E.W. Van Stryland. Sensitive measurement of optical nonlinearities using a single beam. *IEEE Journal of Quantum Electronics*, 26(4):760–769, 1990.

[42] D. Genchi, R. Rangel-Rojo, J. Bornacelli, A. Crespo-Sosa, A. Oliver, and T. Cesca. Spectral nonlinear optical response of ion-implanted au and ag nanoparticles in sapphire: A three-level model description. *Physical Review Applied*, 14(4):044020, 2020.

[43] P. B. Chapple, J. Staromlynska, J. A. Hermann, T. J. Mckay, and R. G. Mcduff. Single-beam z-scan: Measurement techniques and analysis. *Journal of Nonlinear Optical Physics & Materials*, 06(03):251–293, 1997.

[44] A. Gnoli, L. Razzari, and M. Righini. Z-scan measurements using high repetition rate lasers: how to manage thermal effects. *Optics Express*, 13(20):7976–7981, 2005.

[45] S-L Guo, J. Yan, L. Xu, B. Gu, X-Z Fan, and N. B. Ming. Second z-scan in materials with nonlinear refraction and nonlinear absorption. *Journal of Optics A: Pure and Applied Optics*, 4(5):504–508, 2002.

[46] J. M. Khosrofian and B. A. Garetz. Measurement of a gaussian laser beam diameter through the direct inversion of knife-edge data. *Applied Optics*, 22(21):3406–3410, 1983.

[47] M. A. de Araújo, R. Silva, E. de Lima, D. P. Pereira, and P. C. de Oliveira. Measurement of gaussian laser beam radius using the knife-edge technique: improvement on data analysis. *Applied Optics*, 48(2):393–396, 2009.

[48] A. Cotrufo. *Unidimensional hyperbolic metamaterials: synthesis and characterization.* Master's thesis in Physics. 2018.

[49] E. D. Palik. *Handbook of optical constants of solids*, volume 3. Academic press, 1998.

[50] T. Lichtenstein. *Handbook of thin film materials.* College of Engineering and Applied Science, University of Rochester, 1979.

[51] D. E Aspnes. Optical properties of thin films. *Thin Solid Films*, 89(3):249–262, 1982.

[52] J-H Qiu, P. Zhou, X-Y Gao, J-N Yu, S-Y Wang, J. Li, Y-X Zheng, Y-M Yang, Q-H Song, and L-Y Chen. Ellipsometric study of the optical properties of silver oxide prepared by reactive magnetron sputtering. *J. Korean Phys. Soc*, 46(9):269, 2005.

[53] T. Tumkur, Y. Barnakov, S.T. Kee, M.A. Noginov, and V. Liberman. Permittivity evaluation of multilayered hyperbolic metamaterials: Ellipsometry vs. reflectometry. *Journal of Applied Physics*, 117(10):103104, 2015.

[54] D. Genchi. *Multilayer Hyperbolic Metamaterials: synthesis, characterization and control of coupled Eu^{3+} emitters luminescence properties.* Master's thesis in Material Science. 2019.

[55] B.C.P. Sturmberg, K. B. Dossou, F. J. Lawrence, Christopher G. P., Ross C. M., C.M. de Sterke, and L. C. Botten. Emustack: An open source route to insightful electromagnetic computation via the bloch mode scattering matrix method. *Computer Physics Communications*, 202:276–286, 2016.

[56] D. Guo, Q. Guo, K. Zheng, E.G. Wang, and X. Bao. Initial growth and oxygen adsorption of silver on Al_2O_3 film. *The Journal of Physical Chemistry C*, 111(10):3981–3985, 2007.

[57] D.A. King and D.P. Woodruff (Eds.). *Growth and Properties of Ultrathin Epitaxial Layers.* The Chemical Physics of Solid Surfaces 8. Elsevier Science, 1 edition, 1997.

[58] F. Wu. *Planar Defects in Metallic Thin Film Heterostructures.* PhD thesis, 2014.

[59] H Brune. Growth modes. Technical report, Pergamon, 2001.

[60] L.Z. Mezey and J. Giber. The surface free energies of solid chemical elements: calculation from internal free enthalpies of atomization. *Japanese Journal of Applied Physics*, 21(11R):1569, 1982.

[61] L. Vitos, A.V. Ruban, H. L. Skriver, and J. Kollar. The energetics of steps on transition metal surfaces. *Philosophical Magazine B*, 78(5-6):487–495, 1998.

[62] S.H. Overbury, P.A. Bertrand, and G.A. Somorjai. Surface composition of binary systems. prediction of surface phase diagrams of solid solutions. *Chemical Reviews*, 75(5):547–560, 1975.

[63] K. Luo, X. Lai, C-W Yi, K.A. Davis, K.K. Gath, and D.W. Goodman. The growth of silver on an ordered alumina surface. *The Journal of Physical Chemistry B*, 109(9):4064–4068, 2005.

[64] D. G Van Campen and J. Hrbek. Silver on alumina: adsorption and desorption study of model catalysts. *The Journal of Physical Chemistry*, 99(44):16389–16394, 1995.

[65] A. Michaelides, K. Reuter, and M. Scheffler. When seeing is not believing: Oxygen on Ag (111), a simple adsorption system? *Journal of Vacuum Science & Technology A: Vacuum, Surfaces, and Films*, 23(6):1487–1497, 2005.

[66] T-B Hur, H.K. Kim, and J. Blachere. Epitaxial growth of Ag films on native-oxide-covered Si substrates. *Physical Review B*, 75(20):205306, 2007.